Computational Investigations of Supramolecular Polymerization

A Thesis

Submitted For the Degree of

DOCTOR OF PHILOSOPHY

in the Faculty of Science

by

Karteek Kumar Bejagam

CHEMISTRY AND PHYSICS OF MATERIALS UNIT
JAWAHARLAL NEHRU CENTRE FOR ADVANCED SCIENTIFIC RESEARCH
Bangalore – 560 064, India

OCTOBER 2016

To My Family

DECLARATION

I hereby declare that the matter embodied in the thesis entitled "**Computational Investigations of Supramolecular Polymerization**" is the result of investigations carried out by me at the Chemistry and Physics of Materials Unit, Jawaharlal Nehru Centre for Advanced Scientific Research, Bangalore, India under the supervision of Prof. S. Balasubramanian and that it has not been submitted elsewhere for the award of any degree or diploma.

In keeping with the general practice in reporting scientific observations, due acknowledgement has been made whenever the work described is based on the findings of other investigators. Any omission that might have occurred by oversight or error of judgement is regretted.

Karteek Kumar Bejagam

CERTIFICATE

I hereby certify that the matter embodied in this thesis entitled "**Computational Investigations of Supramolecular Polymerization**" has been carried out by Mr. Karteek Kumar Bejagam at the Chemistry and Physics of Materials Unit, Jawaharlal Nehru Centre for Advanced Scientific Research, Bangalore, India under my supervision and that it has not been submitted elsewhere for the award of any degree or diploma.

Prof. S. Balasubramanian
(Research Supervisor)

Acknowledgements

I am very thankful to my research supervisor **Prof. S. Balasubramanian**. I felt very happy to be a part of his lab. I am extremely thankful to him for teaching me simulation techniques and introducing me to the field of supramolecular chemistry. I am pleased with the support he gave me during the hard times.

I thank the Jawaharlal Nehru Centre for providing excellent research facilities. I thank TUE-CMS, JNCASR for providing the computational facilities. I also thank CSIR for the fellowship and DST for the funding. I thank all the academic and non-academic staff of JNCASR.

I express my sincere thanks to all my course instructors Prof. Ranjani Viswanatha, Prof. Swapan Pati, Prof. Umesh Waghmare and Prof. S. Balasubramanian. I also thank my collaborators Prof. Michael L. Klein, Prof. Subi J. George, Prof. K. S. Narayan, Dr. Kulkarni, Dr. Fiorin, Dr. Remsing and Dr. Senanayak.

I am very grateful to Dr. Fiorin and Dr. Remsing, Temple University, Philadelphia for introducing me to various free energy techniques.

I thank the developers of LAMMPS software which has been used to a large extent in this thesis. I also thank the developers of CP2K which too has been used to some extent, herein.

I would like to thank all the present (Tarak, Anirban, Sudip and Divya) and past (Dr. Sandeep, Dr. Rajdeep, Dr. Kanchan, Dr. Chidambar, Dr. Anurag, Dr. Satya, Pallabi and Promit) lab members for the various moments of joy I shared with them.

I thank my all other friends from JNCASR and elsewhere.

I thank my family members, especially my wife and son for keeping me busy throughout the years.

Preface

The thesis is focussed on modelling supramolecular polymers using classical molecular dynamics simulations employing all-atom (AA) and coarse-grain (CG) potentials. Various free energy techniques are used to estimate the free energy profiles for processes related to self-assembly of molecules in solution.

Chapter 1 presents a general introduction to supramolecular polymerization and illustrates the different mechanisms of supramolecular self-assembly. A brief discussion on the previous computational work of modelling supramolecular polymers is also presented. The chapter concludes with a discussion on simulation methods adopted in the thesis.

In chapter 2, atomistic MD simulations of benzene-1,3,5-tricarboxamide (BTA) have been carried out in gas phase and explicit *n*-nonane solution. A non-polarizable force field is sufficient to predict the cooperativity of BTA molecules. Self-assembled structures of BTA molecules have been obtained within MD time-scales, starting from a dispersed configuration. Asymmetric hydrogen bonding pattern in oligomers has been demonstrated to be stable over a symmetric one *via* both quantum chemical calculations and force field approach. Adaptive Biasing Force (ABF) has been employed to determine the free energies to remove a molecule from oligomers of different size and thus to demonstrate cooperativity at ambient conditions.

In chapter 3, coarse-grain potentials for BTA moleules have been developed. Dimerization and solvation free energy profiles obtained from atomistic simulations have been used as benchmark for CG non-bonded potentials. Simulations have been

carried out to understand the monomer exchange event either from a core or from an edge of an oligomer. Free energy simulations have been performed to comment on the type of cooperativity and determine the size of nucleus.

Chapter 4 reports results of simulations of BTA molecules in liquid-crystalline (LC) phase. It is shown that a supramolecular columnar stack reverses its handedness while aligning its macrodipole direction with an external electric field. An experiment to predict the reversal has been proposed.

In chapter 5, molecular dynamics simulations of ester BTAs have been carried out at ambient conditions in cyclohexane solvent. Two dimer variants that are differentiated based on the intermolecular hydrogen bonding pattern are feasible. Three derivatives (BTA-Met, BTA-Nle, and BTA-Phe) have been studied. At ambient conditions, BTA-Met and BTA-Phe can exist as long assemblies while the self-assembly of BTA-Nle does not proceed beyond a dimer.

Chapter 6 discusses the simulations of perylene-bisimide derivatives. Dipole-driven cooperativity has been demonstrated for a perylene derivative appended with carbonate and cholesterol tail. Other two derivatives display no dipolar interactions and thus exhibit isodesmicity.

The thesis concludes with a brief outlook for the future directions in this area.

Contents

List of Figures

List of Tables

Chapter 1

Introduction

Supramolecular chemistry is coined as 'chemistry beyond the molecule' and 'the chemistry of the non-covalent bond' [1–3]. Association of two or more chemical species *via* weak intermolecular forces leads to structures of higher complexity and richness [4, 5]. Hydrogen bonding [6–9], $\pi - \pi$ [10, 11], electrostatic [12, 13], dipole-dipole [14], hydrophobic [15, 16], donor-acceptor [17, 18] are some of these key interactions. Naturally, the strengths of these non-covalent interactions are lower than that of covalent interactions. As a result, supramolecular polymers are less stable, more labile, and more flexible than conventional polymers. "Thus, supramolecular chemistry is concerned with soft bonds and represents a soft chemistry" [4].

Supramolecular assemblies result from a spontaneous association of smaller units, possess well-defined microscopic organization and can have various macroscopic characteristics such as films, layers, membranes, micelles, vesicles, etc. [4]. Supramolecular polymers exhibit a wide variety of applications ranging from biomedical [19] to optoelectronics [20].

Inspiration to supramolecular chemistry often comes from naturally occurring self-assembly phenomena [21]. In biology, four basic building blocks (amino acids, nucleobases, carbohydrates, and lipids) can create highly diverse organisms *via* bottom-up approaches [22]. Design principles for these assembled structures are

unique. “Strategies like that won’t be easy for chemists to emulate. But if they want to make complex, ordered structures from the ground up, they’ll have to get used to thinking a bit more like nature" [23]. Additionally, nature brings about the hierarchical self-assembly of DNA into compact chromosomes [24], and also nascent proteins adopt native states. Such a process leads to well-defined, complex ordered structures and a marginally off-pathway results in protein misfolding that causes diseases such as Alzheimer’s disease [25].

1.1 Supramolecular polymerization

Self-assembly, in the present context, is limited to the spontaneous organization of small, pre-existing components into long, complex ordered structures. Reversible, non-covalent interactions hold the smaller units together in the assembly. Invariably, one-dimensional supramolecular polymers are helical in nature. The architecture of a molecule is such that a twist between the molecules is required to achieve π stacking. In general, molecules involved in supramolecular polymerization consist of three main blocks: core, linker and self-assembling moiety, as illustrated in Figure 1.1. The core is aromatic in nature and requires an intermolecular distance of 3.6 Å for π stacking. The linker can be any functional group which helps in either formation of hydrogen bonds or enhance electrostatic interactions. Self-assembling moieties are typically aliphatic chains. Aliphatic tails are floppy in nature and require large volume. Additionally, the distance between the tails should be around 4.7 Å [26]. Thus, in order to satisfy the twin requirements of optimal $\pi - \pi$ distance and that of tail-tail distance, molecules rotate to form helical assemblies (see Figure 1.1).

Conventional polymers are formed *via* covalent linkage between molecules. Entanglement of these macromolecules results in highly viscous melts. However, for processability, less viscous fluids are better suited. While high temperatures are needed to decrease the viscosity of conventional polymers [27], supramolecular polymers, constituted by weak, non-covalent interactions, possess low viscosity at ambient

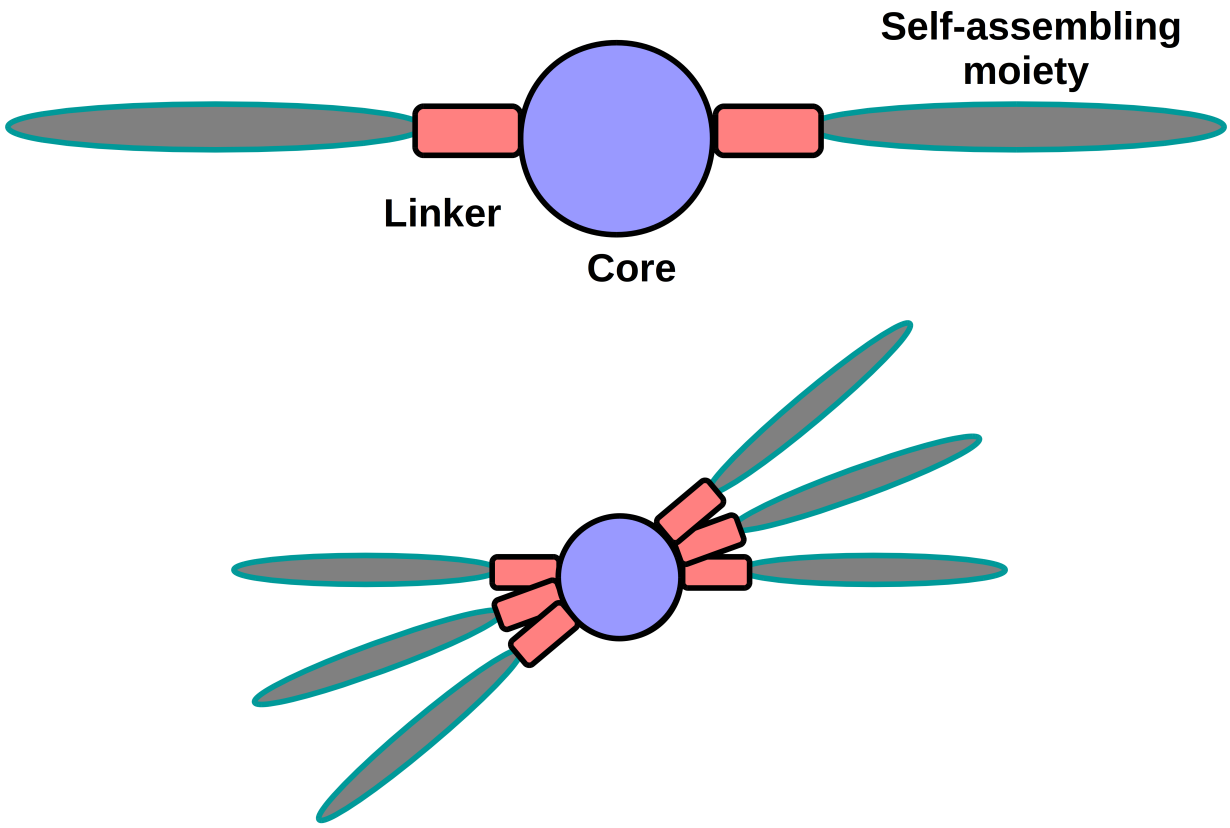

Figure 1.1: (a) Architecture of a molecule undergoing supramolecular polymerization and (b) Its helical assembly. Blue circle, red rectangle and grey ellipse represent the aromatic core, linker and the self-assembling moiety respectively.

conditions [27]. The viscosity of polyethylene glycol is 3500 cP at 150° C [28], whereas that for polyamides at 160° C is about 500 cP [29]. Often, the synthesis of covalent polymers occurs under kinetic control because of a larger barrier for the backward reaction compared to the forward reaction [30]. In contrast, supramolecular polymerization occurs in a thermodynamic control regime, due to fast association/dissociation of molecules [30]. Also, the extent of aggregation of the latter in the solution phase can be varied, by changing either the temperature or the concentration [31].

1.2 Applications

Since the advent of supramolecular chemistry, much research has focused on designing functional materials [32, 33]. Non-covalent weak interactions, principles of self-assembly, dynamic exchange of molecules, repairability, modification of aggregate

structures by changes in temperature/pH are key aspects of most of the applications.

1.2.1 Gels

Supramolecular gels are a class of organic gels made of low molecular weight organogelators. These are formed by the self-assembly of monomer units which are linked together by non-covalent interactions. Conventional polymers are typically used in water to form hydrogels. However, supramolecular gelators can be formed in organic fluids as well [34]. In such gelators, they can be switched from polymers to monomers *via* external stimuli such as temperature or pH. Supramolecular gels are used in the controlled release of drugs, in oil recovery, and serve as a media for crystal growth [35].

1.2.2 Ferroelectrics

Supramolecular chemistry offers a strategy to design lead-free, all-organic ferroelectric materials. For a material to be ferroelectric, it should possess either an intrinsic molecular dipole or an induced dipole resulting from the interactions between the molecules [36]. Alternate packing of aromatic donor (D) and acceptor (A) molecules have emerged as promising candidates in this direction [37]. The assembly is driven by strong charge transfer (CT) interactions. Stupp and co-workers have demonstrated the ferroelectricity of CT complexes at room temperature [17].

Unlike the alternate arrangement, an orthogonal or segregated organization of acceptor and donor molecules leads to significant charge separation. Such a strategy is employed to obtain active materials for solar cells [38].

1.2.3 Healable polymers

Polymers are widely used in various domains, from electronics to medicine. Continuous exposure of polymers to impact, mechanical and thermal stress can lead to their degradation and can result in mechanical failure [39]. In contrast, supramolecular polymers arise due to reversible interactions and thus any such mechanical failures can be repaired either in an autonomous fashion (self-healing) or by the exposure to

heat, light, or mechanical stress (healable) [40]. Repairability of the material helps in increasing its durability and lifetime. Reformation of hydrogen bonds [41], host-guest complexes [42] are the few strategies employed to self-repair.

1.2.4 Security labels

Ajayaghosh and co-workers have designed an approach in which water acts as a self-erasable security marker [43]. The molecules used consist of triple bonded linear aromatic π-backbone (phenylene ethynylene, PE) which acts as a fluorescent core. PE is attached to the bulky group through an amide bond. Intermolecular hydrogen bonding facilitates the formation of aggregates. Assembled structures initially show blue fluorescence and turns into cyan emission in contact with water. The transition is directed by the breakage of hydrogen bonds in the presence of water molecules and can be regained once they evaporate.

1.2.5 Drug carriers

For the treatment of cancer, drugs need to be carried to the specific site of interest. Vesicles formed by the amphiphilic units serve as a promising candidate for drug delivery systems. Drugs can be loaded into the vesicles either using physical encapsulation or chemical conjugation. The loaded nanostructures circulate in the bloodstream and target the tumour tissue *via* both passive and active targeting mechanisms [44].

To control the physical properties of these materials, it is very important to understand the mechanisms by which they self-assemble.

1.3 Mechanisms of self-assembly

Consider the following equilibrium between entities of a supramolecular polymer.

$$X_i + X \underset{k_i^-}{\overset{k_i^+}{\rightleftharpoons}} X_{i+1} \tag{1.1}$$

here X_i represents a polymer of size i, X denotes a monomer, and k_i^+ and k_i^- are the rate constants for the forward (addition) and backward (removal) reactions. The equilibrium constant (K_i) of the reaction is the ratio of rate constants of forward to backward reactions, given by $K_i = \frac{k_i^+}{k_i^-}$.

Based on the magnitude of equilibrium constant between the molecules and its variation with oligomer size, self-assembly is broadly classified into two mechanisms-cooperative and isodesmic [30]. In the former case, $K_1 = K_2 = ...K_{n-1} < K_n = K_{n+1}.... = K_e$, where n is the nucleus. K_e stands for the equilibrium constant in elongation regime. For the latter one, equilibrium constant is identical during all the steps of polymerization ($K_1 = K_2 = ...K_{iso}$), where K_{iso} represents the equilibrium constant of an isodesmic growth.

The two mechanisms are distinguished using UV/visible absorption spectroscopy and circular dichroism spectra as a function of either concentration or temperature. In the process of achieving supramolecular self-assembly under thermodynamic control, the solution is heated to a high temperature where the supramolecules disintegrate and are in a molecularly dissolved (monomer) state. Further, the temperature is slowly decreased, typically at 1 K/min, to ensure that the aggregation proceeds in a thermodynamic limit.

During self-assembly, the UV/visible absorption spectrum changes, which indicates the formation of aggregates. The changes in the spectrum are monitored at a particular wavelength for all the temperatures, to obtain the degree of aggregation α defined as $\alpha = \frac{UV_T - UV_m}{UV_T - UV_{Agg}}$, where 'm', 'Agg' and 'T' stand for the monomer, aggregate and temperature, respectively. The shape of the curve determines the type of mechanism. Isodesmic mechanism follows a sigmoidal growth (Figure 1.2), whereas the cooperative one shows a sharp rise at a specific point (Figure 1.2), as a function of either temperature or concentration.

In an isodesmic growth (also known as equal K model), a monomer adds to any sized oligomer with an equilibrium constant of equal magnitude. Thus, the gain in

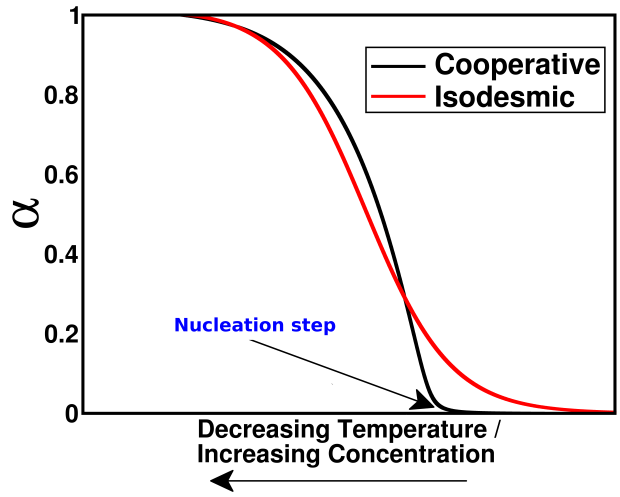

Figure 1.2: Schematic behaviour of normalized degree of aggregation (α) as a function of temperature or concentration for systems which follow an isodesmic and a cooperative mechanism of self-assembly. Here, α=0 represents the monomeric state, while α=1 represents the fully aggregated state. Isodesmic pathway shows a smooth sigmoidal behaviour, whereas the cooperative mechanism is identified by a sharp transition (kink). The point at which the kink is observed is the nucleation step.

free energy remains constant for the monomer addition and is independent of the oligomer size (Figure 1.3a). As a result, the free energy with respect to oligomer size does not change. Cooperative growth (also known as nucleation-elongation model) involves the formation of a nucleus at elongation temperature (T_e), which is identified as a point where α sharply raises. For temperatures below T_e, the nucleus elongates into long stacks. T_e separates the two regimes-nucleation and elongation. The equilibrium constant for the nucleation (K_n) regime is smaller than that in the elongation regime (K_e). The extent of cooperativity can be dependent on molecular and solvent characteristics. The degree of cooperativity (σ) is defined as the ratio of K_n to K_e. For a cooperative growth, σ is always less than 1. The strength of cooperativity depends on the smallness of σ. σ is equal to 1 for an isodesmic growth, since it does not involve any nucleus formation and monomer adds to an oligomer *via* a single equilibrium constant.

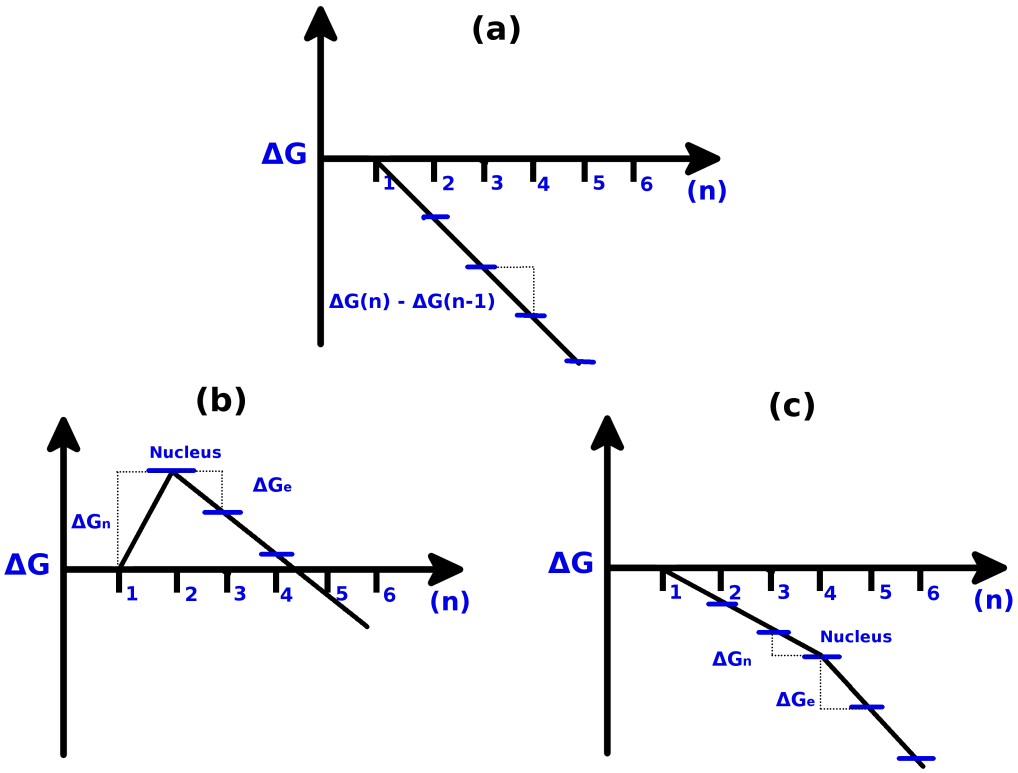

Figure 1.3: Schematic representation of Gibbs free energy profiles for various supramolecular polymerizations as a function of oligomer size. (a) Isodesmic mechanism: change in free energy (ΔG) is constant throughout the polymerization. (b) Uphill cooperative: ΔG becomes positive until the formation of nucleus followed by a favourable elongation. Nucleus is the highest free energy species. (c) Downhill cooperative: ΔG is always negative (favourable). The slope (gain in free energy ΔG_n) is constant until the formation of nucleus and later increases (ΔG_e).

Types of cooperative mechanism

Based on the behaviour of free energy of formation (ΔG) as a function of oligomer size (n), cooperative mechanism can further be sub-divided into uphill and downhill. In an uphill cooperative mechanism, the free energy increases until the formation of nucleus and is followed by a decrease in free energy during the elongation phase (Figure 1.3b). Nucleus is the highest free energy species (unstable) with respect to either monomers or oligomers. On the other hand, in a downhill cooperative pathway, the free energy always decreases with increase in oligomer size (Figure 1.3c). In this case, the monomer is the highest free energy species. However, the slope of the free

energy with oligomer size will change post the formation of a nucleus. Gas-phase quantum chemical calculations of oligomers have demonstrated a non-linear behaviour of the interaction energy between two molecules as a function of oligomer size [45, 46]. It was also proposed earlier that the mechanism of self-assembly can be identified based on specific features of the molecule [31]. It was conjectured that the presence of molecular motifs that give rise to long-range interactions along the growth (stacking) direction leads to a cooperative mechanism and lack of such interactions results in isodesmicity. The same was demonstrated in perylene-bisimide derivatives, both theoretically and experimentally.

1.3.1 Thermodynamic parameters of self-assembly

Meijer and co-workers have developed models to obtain thermodynamic parameters such as enthalpy of release, elongation temperature, change in entropy, degree of cooperativity and also the average size of an oligomer. Analytical expressions are used to fit the degree of aggregation (α) profiles. In a cooperative growth, α remains zero during the nucleation regime, followed by a sharp increase in the elongation regime and then saturates at low temperatures (Figure 1.2). The following expression can be used to fit the α (for T $< T_e$) in order to obtain the enthalpy release

$$\alpha = 1 - exp\left(\frac{h_e(T - T_e)}{RT_e^2}\right) \tag{1.2}$$

For an isodesmic self-assembly, α gradually increases upon cooling (Figure 1.2). It can be fitted with the expression,

$$\alpha = \frac{1}{1 + exp\left(\frac{T - T_m}{T^*}\right)} \tag{1.3}$$

T_m refers to the temperature at which α is 0.5 and T^* is a variable which is obtained from fitting the curve. The following expression is used to estimate the enthalpy of elongation (ΔH)

$$\Delta H = \frac{-RT_m^2}{0.908 \times T^*} \tag{1.4}$$

1.4 Role of stereochemistry

Chiral molecules play a major role in the field of supramolecular chemistry. A molecule is said to be chiral if it possesses a stereogenic center i.e. no two substituents on a given atom are equivalent. Stereocenters are classified into 'S' and 'R' based on the orientational order of substituents (see Figure 1.4). Both forms of the chiral molecules (enantiomers) are configurational isomers of each other and are non-superimposable on their mirror image. Self-recognition is a concept of aggregation which relies on 'like prefers like': molecules of same chirality can self-assemble in a mixture of chiral ones [47].

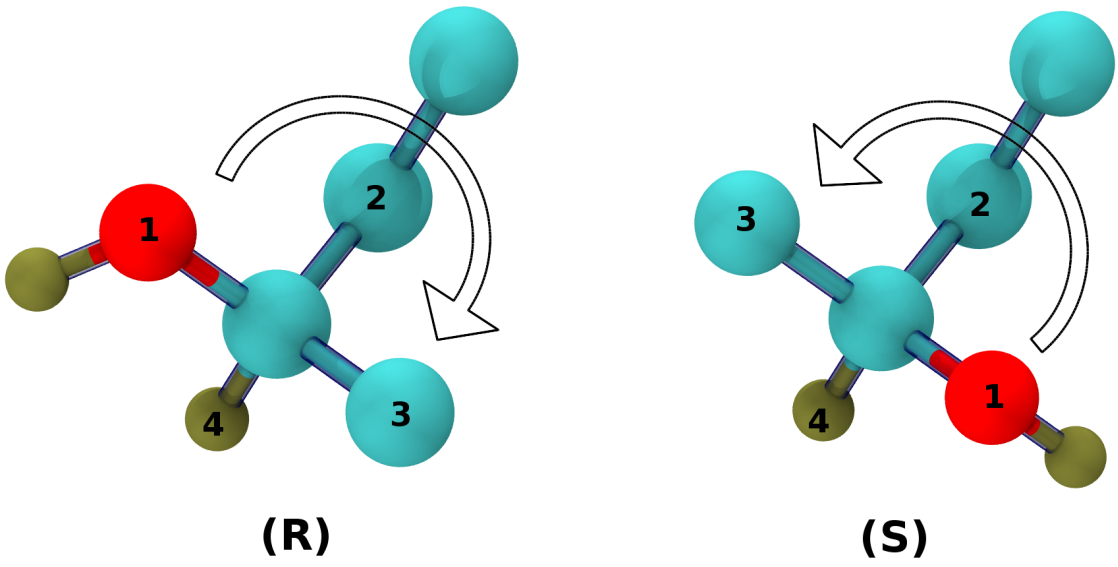

Figure 1.4: Enantiomers of 2-butanol. Sequence of groups attached to the central atom identified with clockwise rotation is denoted as R and counterclockwise as S. Color scheme: carbon-cyan; oxygen-red; hydrogen-tan.

During self-assembly, the presence of a stereogenic center in a molecule will enrich one of the handedness. As a result, only homochiral compounds prevail in nature; L-amino acids and D-sugars [48]. Many researchers have attempted to understand the origin of homochirality in nature [48, 49]. In the field of supramolecular chemistry, self-assembly of chiral molecules can fully bias one of the handedness i.e. diastereomeric excess (d.e.) is 100% (d.e. = ([M]-[P])/([M]+[P]) × 100%), thus, resulting in a chiro-optically active system which can be monitored by circular dichroism (CD) spectra [50]. Here, M and P stand for left- and right-handedness, respectively. Molecules lacking a chiral center are referred to as achiral. Such molecules do not have a preference for any of the handedness, and thus, their assembly results in equal amounts of left- and right-handed stacks, known as a racemic mixture. This system does not lead to a CD signal and is chiro-optically inactive. In such a system, the free energies of formation of stacks of either handedness are equal, thus yielding stacks of 50% left- and 50% right-handedness. Offsetting this balance can favour one of the handedness. In a typical example for benzene-1,3,5-tricarboxamide (BTA), isotopic substitution of deuterium (D) at one of the hydrogen leads to d.e. of 38% i.e. M helices are 69% and P are 31% [50]. Also, the balance between the free energy of formation can be altered by the molecular structure of the solvent as well as temperature [51].

Mixture of chiral and achiral molecules

In the search for the underlying principles of chirality in polyisocyanates, two major principles referred to as 'Sergeants-and-Soldiers' and 'Majority-Rules' were proposed [52]. Later, Meijer and co-workers have shown that these principles are operative even in supramolecular polymers [53]. To favour one of the helical handedness, it is just sufficient to add few chiral (sergeants) units to achiral (soldiers) units, or present a slight majority of R over S or *vice versa* in the solution.

Both the principles have been experimentally demonstrated for BTA derivatives [54], and the same is shown in Figure 1.5. In the Sergeants-and-Soldiers experiment, the addition of just 4% of chiral molecules (sergeants) is enough to fully

bias the achiral (soldiers) ones into adopting a specific handedness for stacking [55]. The experiment was demonstrated at four different temperatures. Figure 1.5a shows the increase in Cotton effect with the fraction of sergeant molecules. Majority-Rules explains the enhancement of helicity if there exists a minute excess of one of the enantiomers over the other [56]. Figure 1.5c represents the increase in CD intensity for a slight off balance between the enantiomers, which means the system will be CD active for non-zero value of enantiomeric excess (e.e.). With the increase in sergeant concentration or enantiomeric excess, the mixture evolves toward the homochiral system. Further, the net helicity versus the fraction of sergeants or e.e. is shown in Figure 1.5c,d. Saturation of net helicity, for fewer sergeants (4%) or minute e.e., corresponds to a fully homochiral system.

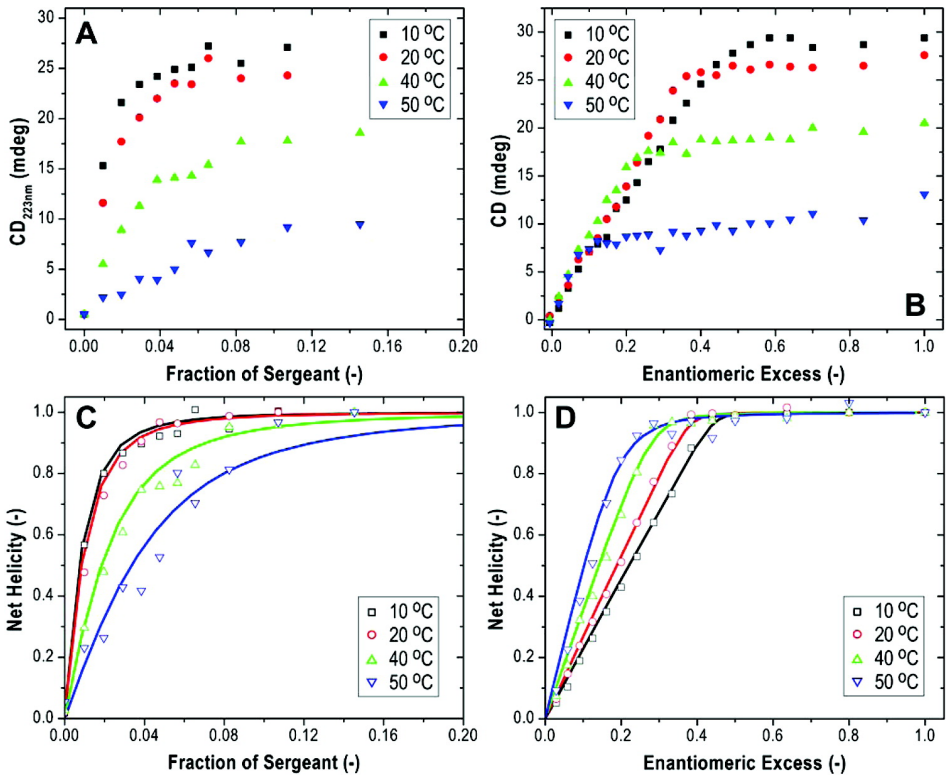

Figure 1.5: Self-assembly studies of achiral and chiral BTAs. (A),(C) demonstrate the 'Sergeants-and-Soldiers' principle. (B),(D) illustrates the 'Majority-Rules' principle. Reprinted with permission from Ref. [54] Copyright 2009 American Chemical Society.

Monomer exchange

The above principles are based on the underlying fact that the monomers can exchange from the solution to the stacks and *vice versa*. Molecules can exchange in the time-scales of seconds [55]. To understand the exchange of molecules, super-resolution microscopy was used to monitor the mixing of two long fibers labeled with different coloured dyes. Stochastic Optical Reconstruction Microscopy (STORM) imaging revealed that the process of mixing proceeds neither through polymerization-depolymerization nor by fragmentation-recombination, but was accounted to the exchange of molecules between the oligomers [57].

Figure 1.6: Schematic to illustrate monomer exchange phenomena. (a) At t=0, molecules are coloured differently to distinguish the monomers and two stacks. (b) Molecules that belong to stacks have exchanged with either monomers or molecules of another stack. (c) As time elapses, several monomer exchange events occur, and thus the stacks become indistinguishable.

1.5 Homochirality: symmetry breaking

In nature, chiral molecules prefer to exist in one kind of handedness due to favourable interactions between the stereocenters of various molecules and results in homochiral compounds [48]. Chiral amplification is one of the methods to achieve homochirality from a racemic mixture. Using external stimuli, one kind of handedness is preferentially enriched to obtain an enantiopure system. Controlling the chirality (handedness) of the system was demonstrated in molecular crystals [58], covalent [59, 60] and supramolecular polymers [61]. As the supramolecules are bound by non-covalent interactions, they are dynamic in nature. In such systems, obtaining

homochirality is a challenging task [62]. Stimuli such as stirring [63–65], circularly polarized light [62, 66], gravitational [67] forces, magnetic forces [68], electrochemical treatment [69] were demonstrated to drive the system towards homochirality. These studies serve as models to understand the existence of homochiral compounds in nature.

1.6 Molecules under study in the present thesis

The present thesis investigates the structure of oligomers and thermodynamic aspects of the supramolecular self-assembly. Molecules undertaken for the study are derivatives of Benzene-1,3,5-tricarboxamide (BTA) and perylene-bisimide (PBI).

1.6.1 Benzene-1,3,5-tricarboxamide

BTA based compounds have been widely studied in the literature by many research groups. In 1915, Curtius synthesized the BTA compound for the first time [70]. As shown in Figure 1.7a, benzene ring with three amide groups (O=C-N-H) at 1,3,5 positions forms a typical BTA molecule. The peripheral 'R' can be aliphatic or aromatic, chiral or achiral, symmetric or asymmetric, and polar or non-polar. BTAs self-assemble into one-dimensional aggregates, mainly driven by strong three-fold intermolecular hydrogen bonding network which propagates in a helical fashion. As a result, columnar stacks possess definite handedness. Clockwise rotation is referred to left-handedness and counterclockwise to right-handedness [71]. Aggregate structures and mechanism of self-assembly are much influenced by the peripheral moieties. For example, alkyl substituted BTAs form three-fold intermolecular hydrogen bonds to result in a cooperative growth of the supramolecular stack. On the other hand, bipyridine BTAs (see Figure 1.7b) self-assemble into one-dimensional aggregates with the help of six intramolecular hydrogen bonds and propeller shape of bipyridine rings. The growth follows an isodesmic path [10].

For BTAs with alkyl substitutions, the molecules self-assemble in non-polar solvents (for e.g. heptane, methylcyclohexane). A BTA monomer is planar in geometry and

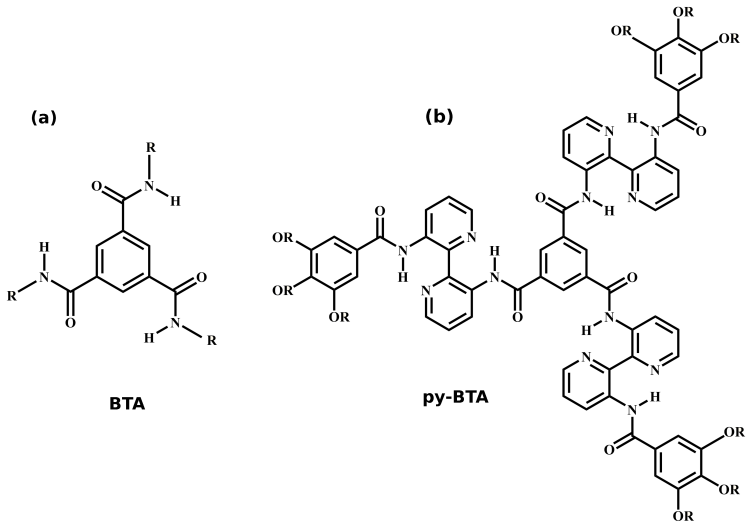

Figure 1.7: (a) Typical core of the BTA family and (b) 3,3'-diamino-2,2'-bipyridine BTA.

thus its dipole moment is zero. In an aggregate, the amide groups rotate about the benzene plane to form three intermolecular hydrogen bonds. As the amide groups get oriented out of the benzene plane, they contribute to a dipole moment along the stacking direction. Further, in a stack, these tiny dipoles located between the molecules add up, to result in a macrodipole along the stacking direction. Presence of the intrinsic macrodipole along the growth direction is responsible for the cooperative growth of BTA aggregates [31]. Self-assembly of achiral BTA molecules result in a racemic mixture. On the other hand, chiral methyl group attached to one of the alkyl tails can fully bias the system towards one of the handedness [50] (see Figure 1.8). Further, shifting the chiral methyl group closer to the amide position ($\delta - \gamma - \beta - \alpha$) increases the stability of columnar stacks which is evident from the higher clearing temperatures [72]. Here 'α' indicates the presence of a chiral center on the first carbon of an alkyl tail. Likewise, β, γ, δ refer to second, third and fourth carbon, respectively. Additionally, CD spectra of BTAs attached with chiral methyl at even (β & δ) and odd (α & γ) positions show different signs indicating the odd-even effect.

Chemists have synthesized various BTA derivatives to explore their properties in various phases: solid-state [73], liquid-crystalline [74, 75] and solution phase [72].

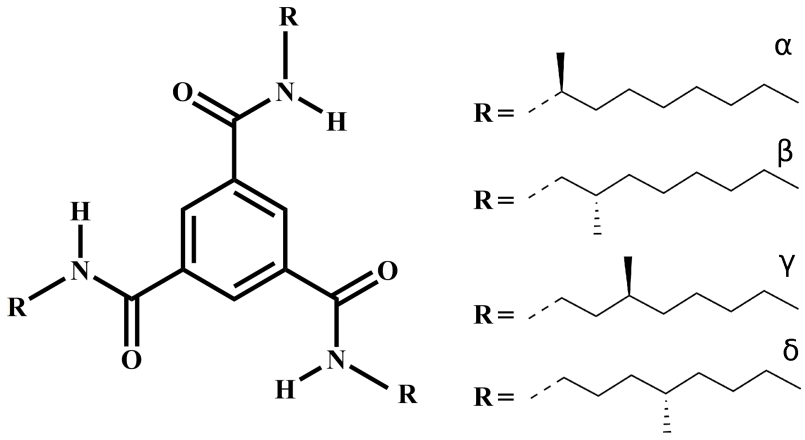

Figure 1.8: Chemical structure of C_3-symmetrical chiral BTA molecules. Position of the chiral methyl group shifting from first to fourth carbon can effect the stability of stacks. All the derivatives are shown in (*S*)-configuration.

Solid state

Crystal structures of BTA family with different side chains have been determined [76–78]. Molecular packing is seen to be very sensitive to the nature of the attached substituent. For N,N',N"-trimethyl-BTA, the crystal structure is a monoclinic $P2_1$ lattice with three intermolecular H-bonds as shown in Figure 1.9a. Two H-bonds (black) are formed in the lateral direction, and a third one (magenta) between the two molecules in a stack [76]. N,N',N"-tripropyl-BTA forms a primitive cubic three-dimensional network [77]. Each molecule is connected to six other molecules through hydrogen bonds. Three molecules are above the benzene plane and another three lie below the plane. Figure 1.9b shows a configuration of the molecule forming three hydrogen bonds with the three different molecules above the plane. For N,N',N"-tris(2-methoxyethyl)-BTA, Lightfoot *et al.* have reported π-stacked molecules with the three-fold H-bonding network [78] (see Figure 1.9c). Experimentalists have considered similar structural motif for self-assembled BTAs with longer alkyl tails in the solution phase [79]. When the substituent (R) is carboxymethyl, it crystallizes into a face-to-face dimerized configuration with six H-bonds. Further, the dimers extend into sheets *via* hydrogen bonding with the water molecules [80].

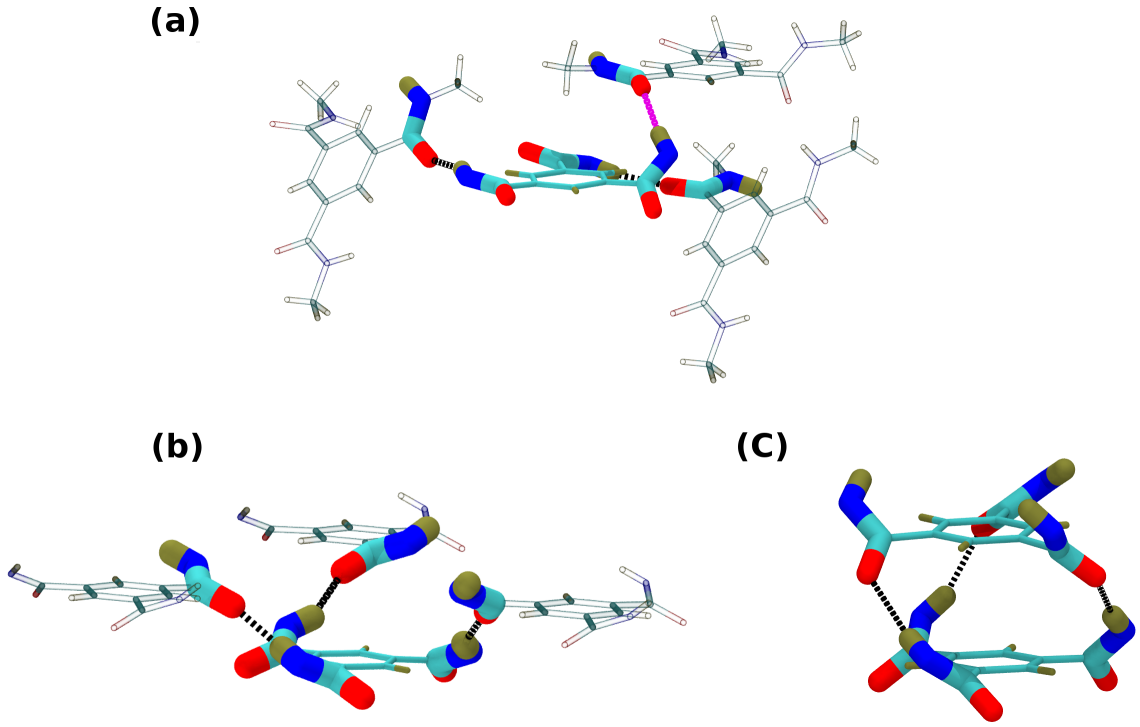

Figure 1.9: Molecular arrangements adapted in the crystal structure of BTA derivatives for various substitutions. (a) R=methyl: molecule forms two lateral hydrogen bonds (black dashed lines) and one (magenta) hydrogen bond between the molecules in a stack. (b) R=propyl: molecule forms three hydrogen bonds with three molecules above and also three hydrogen bonds with another three molecules below the plane of molecule. For clarity only above three are shown. (c) R= methoxyethyl: molecules form a triple helical hydrogen bonding network and resulting in one-dimensional aggregates. Color scheme: carbon-cyan; oxygen-red; nitrogen-blue; hydrogen-tan. Peripheral groups are not shown for clarity.

Liquid-crystalline (LC) phase

Matsunaga *et al.* [74] have synthesized BTAs with various length of alkyl tails and studied the phase behaviour at different temperatures, nearly three decades ago. They observed that BTAs can exhibit the LC phase only if the alkyl tail is longer than or equal to pentyl. In a LC phase, molecules form three-fold hydrogen bonding network that extends along one-dimension. These one-dimensional stacks are arranged in a honeycomb fashion *via* macrodipole-macrodipole interactions [81, 82]. Distance between the neighbouring stacks and distance between two molecules in a given stack

are determined for various length of alkyl chains using X-ray diffraction [81].

One-dimensional stacks of BTAs possess macrodipole along the stacking direction. As the stacks are aligned, macroscopic polarization ensus in the LC phase. Sijbesma and co-workers have exploited this feature to study the ferroelectric behaviour of the LC phase of BTA [83, 84]. In a similar approach, Shishido *et al.* have synthesized various BTA based compounds attaching the amide as well as alkyl chains at two (**2BC**) to six (**6BC**) positions of a benzene ring. They explored the ferroelectric response in the LC phase by applying an external electric field. It was demonstrated that LC phase of **2BC, 3BC**, and **5BC** to be ferroelectric, while **4BC** and **6BC** are paraelectric. In the latter ones, a presence of intramolecular hydrogen bonding inhibits the amide inversion about the benzene plane and thus they behave as paraelectric [85].

Solution phase

Solution phase studies of BTA derivatives were extensively carried out by Meijer and co-workers for the last two decades. Based on the peripheral groups attached to the BTA core, self-assembly can be either cooperative [55] or isodesmic [10]. Also, BTA molecules can self-assemble in non-polar solvents when alkyl chains are attached [86], while, self-assemble in polar solvents for ethylene glycol tails [57]. Structure of an aggregate is highly sensitive to the molecular shape of the solvents [87]. Linear alkyl solvents can intercalate with the alkyl branches of the aggregate, and thus increases the amide rotation about the benzene plane to 45°. In contrast, cyclic solvents cannot intrude with alkyl branches, thus dihedral rotation remains at 35°.

Amino ester-based BTA compounds have been shown to self-assemble either into long assemblies or dimers [88]. The structure of such assemblies is seen to be similar to that of typical BTA stacks, exhibiting triple helical hydrogen bonding between the amide-amide groups. In contrast, in the dimeric species, molecules approach in a face-to-face manner resulting in the formation of six hydrogen bonds between amide-carboxylate groups. Such a dimer does not possess any free hydrogen bonding sites and thereby cannot extend further to form long assemblies. There exist a

competition between the dimeric species and formation of long rods, which can be controlled by either temperature or concentration.

Water-soluble BTAs

In most of the applications such as bio-medical, foodstuffs and cosmetics, water-soluble supramolecular polymers are required [89]. Meijer and co-workers have designed water-soluble BTAs by attaching amphiphilic arms ($C_{12} - PEG_4 - OH$) [90]. Polyethylene glycol (PEG) chains at the termini were added to ensure solubility in aqueous media. Aliphatic tails were able to shield the central hydrogen bonding motifs from the surrounding polar media. Water-soluble BTAs also form one-dimensional aggregates *via* three-fold hydrogen bonding network.

1.6.2 Perylene bisimide

Perylene-3,4,9,10-tetracarboxylic acid bisimides (PBIs) are popularly used as industrial dyes, pigments, electronic and photonic materials [91]. The typical structure that belongs to the PBI family is shown in Figure 6.1. PBIs act as good n-type semiconductors [92]. The ordering of molecules in an aggregate is favoured by $\pi - \pi$ interactions between the cofacial arranged molecules. Crystal structures for various substitutions demonstrate the planar PBI core with a $\pi - \pi$ distance varying from 3.43 Å to 3.50 Å [93]. In an aggregate, each perylene molecule is rotated about an axis perpendicular to the plane of the molecule. Optimization of dipole-dipole interactions between the diimide moieties drive the rotation [92]. Self-assembled structures of PBI are mainly classified into H-type and J-type aggregates based on the relative arrangement of molecules in an oligomer. Absorption spectrum is used as a spectral signature to characterize the type of assembly. For a J-type aggregate, the absorption peak is red-shifted with respect to that of the monomer, whereas, the peak blue shifts for H-type aggregation [94]. Mechanism of the self-assembly for PBI derivatives can be of either isodesmic [95, 96] or cooperative [97, 98], based on the nature of substituents.

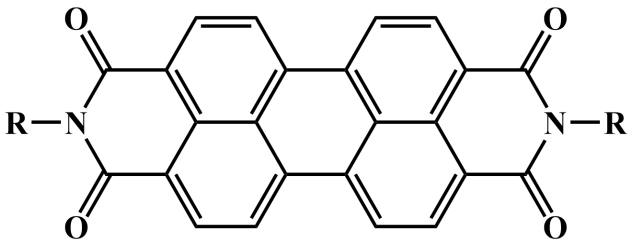

Figure 1.10: Structure of perylene bisimide.

1.7 Status of computational work on supramolecular polymers

A large number of molecules that can polymerize *via* supramolecular interactions have been synthesized by experimentalists and several techniques such as vibrational circular dichroism (VCD), nuclear magnetic resonance (NMR), and X-ray diffraction have been used to understand the structural aspects of oligomers. For a better understanding of geometries and interactions responsible for the stability, either quantum chemical calculations or empirical force field based simulations or both are essential. A handful of theoretical calculations performed to explore the optimized structures, relative stabilities, dominant interactions using electronic structure calculations have been reported so far [45, 46]. Time-dependent density functional theory (TD-DFT) calculations help in obtaining the UV/visible absorption and CD spectra to compare with the experimental ones [99]. Many a time, quantum chemical calculations are very expensive to handle such large molecules. Besides, such quantum calculations are carried out at zero K either in gas-phase or using implicit solvent models. However, the experiments are performed at a finite temperature in bulk solvent.

Force field approach based on the empirical potentials serve as a very good alternative to quantum chemical calculations. In the literature, Molecular Dynamics (MD) simulations have been employed in various fields to study self-assembly of phospholipid into vesicles [100], ionic liquids and amphiphilic polymers into micelles [101, 102] etc. More importantly, simulations are performed at a finite temperature in an

explicit solvent. Simulations are robust enough to predict the morphology at various concentrations too [103]. Perlstein and co-workers have used Monte Carlo (MC) technique to predict the structure [104] and photoreactivity [105] of one-dimensional aggregates. Notwithstanding the above, the magnitude of the computational work in this domain is nowhere commensurate to the progress made experimentally. Thus, a dire need to advance theoretical contributions is necessary. This thesis is an effort in that direction.

1.8 Simulation methodologies

A brief description of computational methods employed in this thesis is provided here for the sake of completeness.

1.8.1 Molecular Dynamics

Molecular Dynamics (MD) is a powerful simulation technique to obtain the static and dynamic properties of a classical many-body system [106–108]. In this approach, molecules are represented *via* a 'ball and stick' model. Equations of motion are used to generate the trajectory phase space (coordinates at various time stamps) which can then be employed to extract macroscopic observables. At a primary level, this method involves solving of Newton's equation of motion for the particles [109],

$$\mathbf{F}_i = m_i \frac{d\mathbf{r}_i^2}{dt^2} \tag{1.5}$$

herein, $\mathbf{F}_i$ represents the force exerted on particle i and m_i, $\mathbf{r}_i$ stands for mass, position of particle i, respectively.

Force can be expressed as the negative gradient of the potential,

$$\mathbf{F}_i = -\nabla_i U \tag{1.6}$$

Combining the above two equations,

$$m_i \frac{d\mathbf{r}_i^2}{dt^2} = -\nabla_i U \tag{1.7}$$

Numerical integration of the above equations allow us to obtain position and momenta of a collection of particles as a function of time. As every thermodynamic observable can be expressed as a function of position and momenta, MD can be employed to determine any structural and dynamical property [110, 111]. Any physical quantity determined experimentally is an ensemble average, while, in simulations, it is a time average. Ergodic hypothesis states that the time average approaches the ensemble average, provided the system explores all regions of phase space with probability appropriate to the particular ensemble. While Equation 1.5 generates a trajectory in the microcanonical ensemble, the same can be modified with additional thermostat and barostat degrees of freedom to generate trajectories in the isothermal-isobaric ensemble. In this thesis, we have exclusively used the Nosé-Hoover [112, 113] methods for the same.

Classical MD technique uses empirical potentials to evaluate the potential energy of the system. Empirical potentials (force fields) have been benchmarked against various physical properties such as density, heat of vapourization, viscosity, etc. The interaction energy can broadly be classified into bonded and non-bonded terms. Bonded interactions consist of bond, angle, dihedral and improper terms. Non-bonded interactions are described by Coulombic and van der Waals terms. To describe a molecule within a given force field, one has to provide all the details of the interaction parameters. In this thesis, the DREIDING force field [114] has been used extensively, as it was general enough to be adapted to several organic systems, considered here. Furthermore, results from the force field on small oligomers in gas phase, were benchmarked against quantum chemical data and were found to be satisfactory.

Various numerical integrators are available to solve the equations of motion.

Euler, Verlet, Leap-frog, velocity-Verlet, Gear predictor-corrector algorithm are a few examples of the integrators [115, 116]. The velocity-Verlet is the simplest and efficient algorithm which preserves time-reversibility and is described as

$$\boldsymbol{p}_i(t + \frac{1}{2}\delta t) = \boldsymbol{p}_i(t) + \frac{1}{2}\delta t \boldsymbol{f}_i(t) \tag{1.8}$$

$$\boldsymbol{r}_i(t + \delta t) = \boldsymbol{r}_i(t) + \delta t \boldsymbol{p}_i(t + \frac{1}{2}\delta t)/m_i \tag{1.9}$$

$$\boldsymbol{p}_i(t + \delta t) = \boldsymbol{p}_i(t + \frac{1}{2}\delta t) + \frac{1}{2}\delta t \boldsymbol{f}_i(t + \delta t) \tag{1.10}$$

All the simulations reported in this thesis employ the velocity-Verlet algorithm.

1.8.2 Free energy calculations

Free energy is indeed an important thermodynamic quantity, and can refer to Helmholtz (A) or Gibbs (G) free energy. At thermodynamic equilibrium, a system is at its minimum free energy. In the canonical ensemble, free energy is expressed in terms of partition function (Z) as A= - k_BT ln (Z). Determination of free energy will give access to various thermodynamic variables. In the canonical ensemble, entropy (S), pressure (P), chemical potential (μ) are expressed as

$$S = -\left(\frac{\partial F}{\partial T}\right)_{V,N} \qquad P = -\left(\frac{\partial F}{\partial V}\right)_{T,N} \qquad \mu = -\left(\frac{\partial F}{\partial N}\right)_{T,V} \tag{1.11}$$

Techniques to calculate the free energy of a system are useful to understand protein-ligand binding, phase-transitions, protein folding, relative stability of structures etc. The free energy differences in all these processes can be determined. Given that many of these processes are rare with respect to simulation timescales and unbiased MD simulations are unsuited to study them. Three classical approaches namely Thermodynamic Integration (TI), Free Energy Perturbation (FEP) and Particle

Insertion (PI) form the basis to determine the free energy difference between two states. Most advanced sampling methods include Steered Molecular Dynamics (SMD) [117], Adaptive Biasing Force (ABF) [118], Umbrella Sampling (US) [119], and Metadynamics [120]. Metadynamics has been combined with umbrella sampling technique to reduce the computational time for orthogonal collective variables [121]. In the present thesis, ABF and SMD methods have been extensively used to determine free energy differences and these are described briefly, below.

Adaptive Biasing Force

Adaptive Biasing Force (ABF) is a force based technique developed by Darve and Pohorille [118]. The change in free energy (ΔA) from state A to state B as a function of a reaction coordinate (RC) 'ξ' can be determined as follows. The entire RC is divided into smaller bins for the accumulation of instantaneous forces experienced on the ξ. Force on the RC is given by $(-\partial U/\partial \xi)$ and it is averaged in each bin for a given number of samples. Later, ABF applies an equal and opposite force as that of the average force so as to nullify the effective force on ξ.

$$-\langle F_\xi \rangle_\xi = \left\langle \frac{\partial U}{\partial \xi} - \frac{1}{\beta}\frac{\partial ln|J|}{\partial \xi} \right\rangle \tag{1.12}$$

here, $|J|$ is the determinant of the Jacobian for the transformation from the generalized to Cartesian coordinates. The first term refers to the average force exerted along the RC. Now, ABF applies an opposite force to nullify it,

$$F^{ABF} = -\langle F_\xi \rangle_\xi \nabla_x \xi \tag{1.13}$$

During the course of ABF simulation, the potential energy surface gradually becomes flatter and thus, allow the system for a free "flow" along the RC. The sampling of the RC, at times, depends on the diffusion rates along the RC. In order to obtain an adequate sampling for long reaction pathways, the entire ξ is divided into

shorter consecutive windows. ABF does not demand the consecutive windows to be overlapping. The free energy profiles in each window are stitched to obtain the final FE profile using a keyword 'inputprefix' in the colvars package [122].

Steered Molecular Dynamics

Steered Molecular Dynamics is a non-equilibrium approach developed by Schulten and co-workers [117]. The method operates in two modes: constant velocity and constant force. In constant velocity, one end of the spring (with force constant k) is attached to a SMD atom while the other end moves at a constant velocity. In constant force mode, a force of constant magnitude is applied on the SMD atom. In both the approaches, the SMD atom moves to the desired point and the system evolves from a state A to state B. Work done on the system is determined and further used to evaluate the free energy difference. Jarzynksi's equality [123] is employed to determine the equilibrium free energy difference from the non-equilibrium work.

$$e^{-\beta \Delta F} = \langle e^{-\beta \Delta W} \rangle \tag{1.14}$$

Here, W represents the work done on the system. Pulling experiments have to be performed several times in order to obtain various work trajectories. Ensemble average of these work trajectories is used to obtain the free energy difference.

1.9 Scope of the thesis

Computational methods can aid in obtaining a microscopic understanding of various phenomena and also unravel the interactions which determine the mechanism of self-assembly. The present thesis aims to investigate the structural and thermodynamic aspects of supramolecular self-assembly using computational methods. MD simulations have been performed using LAMMPS [124] package. DREIDING [114] force field has been adopted for modelling supramolecules. Where possible, results

from forcefields have been benchmarked against gas phase quantum chemical calculations carried out using either CP2K [125] or Gaussian09 [126].

Atomistic MD simulations have been performed on N,N',N"-trialkylbenzene-1,3,5-tricarboxamide to investigate the self-assembled structures in non-polar solvents at finite temperature. An asymmetric pattern of hydrogen-bonding in an assembly is favoured over the corresponding symmetric one due to dipole-dipole interactions. Dimerization and solvation free energies of BTAs attached with various alkyl tails have been determined. Free energy simulations to remove a molecule from oligomers of different size have been carried out which illustrate the cooperative mechanism of self-assembly.

Atomistic models involve huge degrees of freedom which limit the system size and simulation time-scales. Coarse-grain (CG) representation of molecules can alleviate some of these limitations. Coarse-grain potentials for alkyl BTA which rely on atomistic models have been developed to predict the self-assembly at millimolar concentrations, comparable to experimental concentrations. In one of the CG model, an intrinsic point dipole is embedded on an amide bead so as to impart a macrodipole to the oligomer along stacking direction, consistent with atomistic model. CG simulations have been carried out to understand the monomer exchange phenomena occurring either at the edge or at the core of an oligomer. Additionally, simulations have been performed which demonstrate the downhill cooperative nature of self-assembly whose nucleus size is shown to be three.

The thesis also reports simulations in the liquid-crystalline phase of BTA. Alignment of one-dimensional BTA stacks in a hexagonal packing ensures macroscopic polarization in the LC phase. Sijbesma and co-workers have demonstrated the polar switching of columnar stacks in the LC phase upon the application of an external electric field [83, 84]. MD simulations have been carried out to investigate the switching mechanism. Upon the application of an external electric field in a direction opposite to that of macrodipole direction, a supramolecular columnar stack reverses

its handedness in the process of aligning its macrodipole to the field. Experiments to verify such a helix handedness reversal in a supramolecular columnar stack have been proposed.

The structure of BTA aggregates is sensitive to the attached peripheral groups. BTAs with linear alkyl tails have been studied extensively. Further, simulations of three derivatives of amino ester BTAs (BTA-Met, BTA-Nle, and BTA-Phe) have been performed. Desmarchelier *et al.* have demonstrated that BTA-Met and BTA-Phe can form long assemblies while self-assembly of BTA-Nle is limited to just dimers, at ambient conditions [88]. Our studies reveal that two variants of dimers are feasible based on the intermolecular hydrogen bonding pattern. Amide-amide (AA) dimer consists of hydrogen bonds between amide groups, similar to alkyl BTA stacks. Amide-carboxylate (AC) dimer is formed *via* hydrogen bonding between amide and carboxylate groups, wherein also two molecules approach each other in a face-to-face manner. The AC dimer is favoured over the AA dimer by ≈ 20 kcal/mol at zero Kelvin in gas phase. MD simulations suggest that oligomers of BTA-Met and BTA-Phe are stabilized by weak CH$\cdots$S and CH$\cdots\pi$ hydrogen bonds respectively as well as 1-3 interactions. Free energy calculations for oligomerization clearly demonstrate the infeasibility of oligomerization in BTA-Nle and its possibility in the other two systems.

Experimentally, UV/visible absorption and circular dichroism studies help in distinguishing the mechanism of self-assembly. However, the origin of these mechanisms from a molecular level perspective is poorly understood. It has been conjectured that the presence of long-range interactions along the stacking direction results in cooperative mechanism and lack of such interactions lead to isodesmicity [31]. MD simulations presented in this thesis establish dipole driven cooperativity for perylene-bisimide (PBI) molecules appended with carbonate (as a linker) and cholesterol self-assembling moiety. Oligomers of other PBI derivatives which lack dipolar interactions along the growth direction stack irregularly and have been experimentally

seen to be assemble isodesmically. The MD simulations thus offer a microscopic rationale for the experimentally observed differences in self-assembly mechanisms of PBI derivatives.

Bibliography

[1] Lehn, J.-M. *Angew. Chem. Int. Ed.* **1988**, *27*, 89–112.

[2] Ciferri, A. *Supramolecular Polymers*; Taylor & Francis, 2005.

[3] Steed, J. W.; Atwood, J. L. *Supramolecular Chemistry*; Wiley, 2009.

[4] Lehn, J.-M. *Supramolecular Chemistry*; Wiley-VCH Verlag GmbH & Co. KGaA, 2006.

[5] Mahadevi, A. S.; Sastry, G. N. *Chem. Rev.* **2016**, *116*, 2775–2825.

[6] Ramaekers, M.; de Feijter, I.; Bomans, P. H. H.; Sommerdijk, N. A. J. M.; Dankers, P. Y. W.; Meijer, E. W. *Macromolecules* **2014**, *47*, 3823–3828.

[7] Cantekin, S.; de Greef, T. F. A.; Palmans, A. R. A. *Chem. Soc. Rev.* **2012**, *41*, 6125–6137.

[8] Papmeyer, M.; Vuilleumier, C. A.; Pavan, G. M.; Zhurov, K. O.; Severin, K. *Angew. Chem. Int. Ed.* **2016**, *55*, 1685–1689.

[9] Brocorens, P.; Linares, M.; Guyard-Duhayon, C.; Guillot, R.; Andrioletti, B.; Suhr, D.; Isare, B.; Lazzaroni, R.; Bouteiller, L. *J. Phys. Chem. B* **2013**, *117*, 5379–5386.

[10] Metzroth, T.; Hoffmann, A.; Martin-Rapun, R.; Smulders, M. M. J.; Pieterse, K.; Palmans, A. R. A.; Vekemans, J. A. J. M.; Meijer, E. W.; Spiess, H. W.; Gauss, J. *Chem. Sci.* **2011**, *2*, 69–76.

[11] Kulkarni, C.; Munirathinam, R.; George, S. J. *Chem. Eur. J.* **2013**, *19*, 11270–11278.

[12] Costa, C.; Francisco, V.; Silva, S. G.; do Vale, M. L. C.; García-Río, L.; Marques, E. F. *Colloids and Surfaces A: Physicochem. Eng. Aspects* **2015**, *480*, 71 – 78.

[13] Xie, Y.; Wang, X.; Huang, R.; Qi, W.; Wang, Y.; Su, R.; He, Z. *Langmuir* **2015**, *31*, 2885–2894.

[14] Li, L.; Wu, R.; Guang, S.; Su, X.; Xu, H. *Phys. Chem. Chem. Phys.* **2013**, *15*, 20753–20763.

[15] Heussner, K.; Grabau, M.; Forster, J.; Streb, C. *Eur. J. Inorg. Chem.* **2011**, *2011*, 5125–5131.

[16] Sánchez-Iglesias, A.; Grzelczak, M.; Altantzis, T.; Goris, B.; Pérez-Juste, J.; Bals, S.; Tendeloo, G. V.; Stephen H. Donaldson, J.; Chmelka, B. F.; Israelachvili, J. N.; Liz-Marzán, L. M. *ACS Nano* **2012**, *6*, 11059–11065.

[17] Tayi, A. S. et al. *Nature* **2012**, *488*, 485–489.

[18] Wang, C.; Guo, Y.; Wang, Z.; Zhang, X. *Langmuir* **2010**, *26*, 14509–14511.

[19] Ma, X.; Zhao, Y. *Chem. Rev.* **2015**, *115*, 7794–7839.

[20] Chevrier, M.; Kesters, J.; Blayo, C.; Richeter, S.; Van Der Lee, A.; Coulembier, O.; Surin, M.; Mehdi, A.; Lazzaroni, R.; Evans, R. C.; Maes, W.; Dubois, P.; Clément, S. *Macromol. Chem. Phys.* **2016**, *217*, 445–458.

[21] Tu, Y.; Peng, F.; Adawy, A.; Men, Y.; Abdelmohsen, L. K. E. A.; Wilson, D. A. *Chem. Rev.* **2016**, *116*, 2023–2078.

[22] Avinash, M. B.; Govindaraju, T. *Nanoscale* **2014**, *6*, 13348–13369.

[23] Service, R. F. *Science* **2005**, *309*, 95.

[24] Alberts, B.; Bray, D.; Lewis, J.; Raff, M.; Roberts, K.; Watson, J. D. *Molecular Biology of the Cell (3rd edition)*; Newyork: Garland Publishing, Inc., 1994.

[25] Thomas, P. J.; Qu, B.-H.; Pedersen, P. L. *Trends Biochem. Sci.* **1995**, *20*, 456 – 459.

[26] Boese, R.; Weiss, H.-C.; Bläser, D. *Angew. Chem. Int. Ed.* **1999**, *38*, 988–992.

[27] de Greef, T. F. A.; Meijer, E. W. *Nature* **2008**, *453*, 171–173.

[28] Das, A. K.; Hsu, D.-Y.; Hong, P.-D. *Macromol. Theory Simul.* **2011**, *20*, 19–30.

[29] Agnaou, R.; Capelot, M.; Tencé-Girault, S.; Tournilhac, F.; Leibler, L. *J. Am. Chem. Soc.* **2014**, *136*, 11268–11271.

[30] De Greef, T. F. A.; Smulders, M. M. J.; Wolffs, M.; Schenning, A. P. H. J.; Sijbesma, R. P.; Meijer, E. W. *Chem. Rev.* **2009**, *109*, 5687–5754.

[31] Kulkarni, C.; Balasubramanian, S.; George, S. J. *ChemPhysChem* **2013**, *14*, 661–673.

[32] Aida, T.; Meijer, E. W.; Stupp, S. I. *Science* **2012**, *335*, 813–817.

[33] Busseron, E.; Ruff, Y.; Moulin, E.; Giuseppone, N. *Nanoscale* **2013**, *5*, 7098–7140.

[34] Suzuki, M.; Hanabusa, K. *Chem. Soc. Rev.* **2010**, *39*, 455–463.

[35] Sangeetha, N. M.; Maitra, U. *Chem. Soc. Rev.* **2005**, *34*, 821–836.

[36] Tayi, A. S.; Kaeser, A.; Matsumoto, M.; Aida, T.; Stupp, S. I. *Nat. Chem.* **2015**, *7*, 281–294.

[37] Kumar, M.; Venkata Rao, K.; George, S. J. *Phys. Chem. Chem. Phys.* **2014**, *16*, 1300–1313.

[38] Bhosale, R.; Misek, J.; Sakai, N.; Matile, S. *Chem. Soc. Rev.* **2010**, *39*, 138–149.

[39] Colquhoun, H.; Klumperman, B. *Polym. Chem.* **2013**, *4*, 4832–4833.

[40] Hart, L. R.; Harries, J. L.; Greenland, B. W.; Colquhoun, H. M.; Hayes, W. *Polym. Chem.* **2013**, *4*, 4860–4870.

[41] Herbst, F.; Döhler, D.; Michael, P.; Binder, W. H. *Macromol. Rapid Commun.* **2013**, *34*, 203–220.

[42] Li, G.; Wu, J.; Wang, B.; Yan, S.; Zhang, K.; Ding, J.; Yin, J. *Biomacromolecules* **2015**, *16*, 3508–3518.

[43] Thirumalai, R.; Mukhopadhyay, R. D.; Praveen, V. K.; Ajayaghosh, A. *Sci. Rep.* **2015**, *5*, 9842.

[44] Thomas, S. N.; Schudel, A. *Curr. Opin. Chem. Eng.* **2015**, *7*, 65 – 74.

[45] Kulkarni, C.; Reddy, S. K.; George, S. J.; Balasubramanian, S. *Chem. Phys. Lett.* **2011**, *515*, 226 – 230.

[46] Filot, I. A. W.; Palmans, A. R. A.; Hilbers, P. A. J.; van Santen, R. A.; Pidko, E. A.; de Greef, T. F. A. *J. Phys. Chem. B* **2010**, *114*, 13667–13674.

[47] Sato, K.; Itoh, Y.; Aida, T. *Chem. Sci.* **2014**, *5*, 136–140.

[48] Blackmond, D. G. *Cold Spring Harb Perspect Biol.* **2010**, *2*, a002147.

[49] Breslow, R. *Tetrahedron Lett.* **2011**, *52*, 2028 – 2032.

[50] Cantekin, S.; Balkenende, D. W. R.; Smulders, M. M. J.; Palmans, A. R. A.; W., M. E. *Nat. Chem.* **2011**, *3*, 42–46.

[51] Cantekin, S.; Nakano, Y.; Everts, J. C.; van der Schoot, P.; Meijer, E. W.; Palmans, A. R. A. *Chem. Commun.* **2012**, *48*, 3803–3805.

[52] Green, M. M.; Peterson, N. C.; Sato, T.; Teramoto, A.; Cook, R.; Lifson, S. *Science* **1995**, *268*, 1860–1866.

[53] Palmans, A. R. A.; Vekemans, J. A. J. M.; Havinga, E. E.; Meijer, E. W. *Angew. Chem. Int. Ed.* **1997**, *36*, 2648–2651.

[54] Smulders, M. M. J.; Filot, I. A. W.; Leenders, J. M. A.; van der Schoot, P.; Palmans, A. R. A.; Schenning, A. P. H. J.; Meijer, E. W. *J. Am. Chem. Soc.* **2010**, *132*, 611–619.

[55] Smulders, M. M. J.; Schenning, A. P. H. J.; Meijer, E. W. *J. Am. Chem. Soc.* **2008**, *130*, 606–611.

[56] Smulders, M. M. J.; Stals, P. J. M.; Mes, T.; Paffen, T. F. E.; Schenning, A. P. H. J.; Palmans, A. R. A.; Meijer, E. W. *J. Am. Chem. Soc.* **2010**, *132*, 620–626.

[57] Albertazzi, L.; van der Zwaag, D.; Leenders, C. M. A.; Fitzner, R.; van der Hofstad, R. W.; Meijer, E. W. *Science* **2014**, *344*, 491–495.

[58] Viedma, C.; Ortiz, J. E.; Torres, T. d.; Izumi, T.; Blackmond, D. G. *J. Am. Chem. Soc.* **2008**, *130*, 15274–15275.

[59] Green, M. M.; Park, J.-W.; Sato, T.; Teramoto, A.; Lifson, S.; Selinger, R. L. B.; Selinger, J. V. *Angew. Chem. Int. Ed.* **1999**, *38*, 3138–3154.

[60] Green, M. M.; Cheon, K.-S.; Yang, S.-Y.; Park, J.-W.; Swansburg, S.; Liu, W. *Acc. Chem. Res.* **2001**, *34*, 672–680.

[61] Palmans, A. R. A.; Meijer, E. W. *Angew. Chem. Int. Ed.* **2007**, *46*, 8948–8968.

[62] Bisoyi, H. K.; Li, Q. *Angew. Chem. Int. Ed.* **2016**, *55*, 2994–3010.

[63] Ribó, J. M.; Crusats, J.; Sagués, F.; Claret, J.; Rubires, R. *Science* **2001**, *292*, 2063–2066.

[64] Yamaguchi, T.; Kimura, T.; Matsuda, H.; Aida, T. *Angew. Chem. Int. Ed.* **2004**, *43*, 6350–6355.

[65] Wolffs, M.; George, S. J.; Tomović Ž.; Meskers, S. C. J.; Schenning, A. P. H. J.; Meijer, E. W. *Angew. Chem. Int. Ed.* **2007**, *46*, 8203–8205.

[66] Bailey, J.; Chrysostomou, A.; Hough, J. H.; Gledhill, T. M.; McCall, A.; Clark, S.; Ménard, F.; Tamura, M. *Science* **1998**, *281*, 672–674.

[67] Edwards, D.; Cooper, K.; Dougherty, R. C. *J. Am. Chem. Soc.* **1980**, *102*, 381–382.

[68] Micali, N.; Engelkamp, H.; van Rhee, P. G.; Christianen, P. C. M.; Scolaro, L. M.; Maan, J. C. *Nat. Chem.* **2012**, *4*, 201–207.

[69] Yang, X.; Seo, S.; Park, C.; Kim, E. *Macromolecules* **2014**, *47*, 7043–7051.

[70] T., C. *J. Prakt. Chem.* **1915**, *91*, 39 – 100.

[71] Jung, S. H.; Jeon, J.; Kim, H.; Jaworski, J.; Jung, J. H. *J. Am. Chem. Soc.* **2014**, *136*, 6446–6452.

[72] Stals, P. J. M.; Smulders, M. M. J.; Martín-Rapún, R.; Palmans, A. R. A.; Meijer, E. W. *Chem. Eur. J.* **2009**, *15*, 2071–2080.

[73] Wegner, M.; Dudenko, D.; Sebastiani, D.; Palmans, A. R. A.; de Greef, T. F. A.; Graf, R.; Spiess, H. W. *Chem. Sci.* **2011**, *2*, 2040–2049.

[74] Matsunaga, Y.; Nakayasu, Y.; Sakai, S.; Yonenaga, M. *Mol. Cryst. Liq. Cryst.* **1986**, *141*, 327–333.

[75] Singer, J. C.; Giesa, R.; Schmidt, H.-W. *Soft Matter* **2012**, *8*, 9972–9976.

[76] Hanabusa, K.; Koto, C.; Kimura, M.; Shirai, H.; Kakehi, A. *Chem. Lett.* **1997**, *26*, 429–430.

[77] Jiménez, C. A.; Belmar, J. B.; Ortíz, L.; Hidalgo, P.; Fabelo, O.; Pasán, J.; Ruiz-Pérez, C. *Cryst. Growth Des.* **2009**, *9*, 4987–4989.

[78] Lightfoot, M. P.; Mair, F. S.; Pritchard, R. G.; Warren, J. E. *Chem. Commun.* **1999**, 1945–1946.

[79] de Greef, T. F. A.; Nieuwenhuizen, M. M. L.; Stals, P. J. M.; Fitie, C. F. C.; Palmans, A. R. A.; Sijbesma, R. P.; Meijer, E. W. *Chem. Commun.* **2008**, 4306–4308.

[80] Gong, B.; Zheng, C.; Yan, Y. *J. Chem. Crystallogr.* **1999**, *29*, 649–652.

[81] Timme, A.; Kress, R.; Albuquerque, R. Q.; Schmidt, H.-W. *Chem. Eur. J.* **2012**, *18*, 8329–8339.

[82] Albuquerque, R. Q.; Timme, A.; Kress, R.; Senker, J.; Schmidt, H.-W. *Chem. Eur. J.* **2013**, *19*, 1647–1657.

[83] Fitié, C. F. C.; Roelofs, W. S. C.; Kemerink, M.; Sijbesma, R. P. *J. Am. Chem. Soc.* **2010**, *132*, 6892–6893.

[84] Fitié, C. F. C.; Roelofs, W. S. C.; Magusin, P. C. M. M.; Wübbenhorst, M.; Kemerink, M.; Sijbesma, R. P. *J. Phys. Chem. B* **2012**, *116*, 3928–3937.

[85] Shishido, Y.; Anetai, H.; Takeda, T.; Hoshino, N.; ichiro Noro, S.; Nakamura, T.; Akutagawa, T. *J. Phys. Chem. C* **2014**, *118*, 21204–21214.

[86] Brunsveld, L.; Schenning, A. P. H. J.; Broeren, M. A. C.; Janssen, H. M.; Vekemans, J. A. J. M.; Meijer, E. W. *Chem. Lett.* **2000**, *29*, 292–293.

[87] Nakano, Y.; Hirose, T.; Stals, P. J. M.; Meijer, E. W.; Palmans, A. R. A. *Chem. Sci.* **2012**, *3*, 148–155.

[88] Desmarchelier, A.; Raynal, M.; Brocorens, P.; Vanthuyne, N.; Bouteiller, L. *Chem. Commun.* **2015**, *51*, 7397–7400.

[89] Baker, M. B.; Albertazzi, L.; Voets, I. K.; Leenders, C. M. A.; Palmans, A. R. A.; Pavan, G. M.; Meijer, E. W. *Nat. Commun.* **2015**, *6*.

[90] Leenders, C. M. A.; Albertazzi, L.; Mes, T.; Koenigs, M. M. E.; Palmans, A. R. A.; Meijer, E. W. *Chem. Commun.* **2013**, *49*, 1963–1965.

[91] Würthner, F. *Chem. Commun.* **2004**, 1564–1579.

[92] Struijk, C. W.; Sieval, A. B.; Dakhorst, J. E. J.; van Dijk, M.; Kimkes, P.; Koehorst, R. B. M.; Donker, H.; Schaafsma, T. J.; Picken, S. J.; van de Craats, A. M.; Warman, J. M.; Zuilhof, H.; Sudhölter, E. J. R. *J. Am. Chem. Soc.* **2000**, *122*, 11057–11066.

[93] Zugenmaier, P.; Duff, J.; Bluhm, T. *Cryst. Res. Technol.* **2000**, *35*, 1095–1115.

[94] Ghosh, S.; Li, X.-Q.; Stepanenko, V.; Würthner, F. *Chem. Eur. J.* **2008**, *14*, 11343–11357.

[95] Würthner, F.; Thalacker, C.; Diele, S.; Tschierske, C. *Chem. Eur. J.* **2001**, *7*, 2245–2253.

[96] Chen, Z.; Stepanenko, V.; Dehm, V.; Prins, P.; Siebbeles, L.; Seibt, J.; Marquetand, P.; Engel, V.; Würthner, F. *Chem. Eur. J.* **2007**, *13*, 436–449.

[97] Seki, T.; Asano, A.; Seki, S.; Kikkawa, Y.; Murayama, H.; Karatsu, T.; Kitamura, A.; Yagai, S. *Chem. Eur. J.* **2011**, *17*, 3598–3608.

[98] Yagai, S.; Usui, M.; Seki, T.; Murayama, H.; Kikkawa, Y.; Uemura, S.; Karatsu, T.; Kitamura, A.; Asano, A.; Seki, S. *J. Am. Chem. Soc.* **2012**, *134*, 7983–7994.

[99] Li, X.; Zhu, L.; Duan, S.; Zhao, Y.; Ågren, H. *Phys. Chem. Chem. Phys.* **2014**, *16*, 23854–23860.

[100] Marrink, S. J.; ; Mark, A. E. *J. Am. Chem. Soc.* **2003**, *125*, 15233–15242.

[101] Liu, X.; Zhou, G.; He, H.; Zhang, X.; Wang, J.; Zhang, S. *Ind. Eng. Chem. Res.* **2015**, *54*, 1681–1688.

[102] Liu, L.; Parameswaran, S.; Sharma, A.; Grayson, S. M.; Ashbaugh, H. S.; Rick, S. W. *J. Phys. Chem. B* **2014**, *118*, 6491–6497.

[103] Srinivas, G.; Discher, D. E.; Klein, M. L. *Nat. Mater.* **2004**, *3*, 638–644.

[104] Perlstein, J. *J. Am. Chem. Soc.* **1992**, *114*, 1955–1963.

[105] Song, X.; Perlstein, J.; ; Whitten, D. G. *J. Am. Chem. Soc.* **1997**, *119*, 9144–9159.

[106] Mentz-Stern, R.; Hoheisel, C. *Phys. Rev. A* **1989**, *40*, 4558–4563.

[107] Liu, J.; Cao, D.; Zhang, L. *J. Chem. Phys.* **2009**, *131*.

[108] Paul, W.; Smith, G. D.; Yoon, D. Y. *Macromolecules* **1997**, *30*, 7772–7780.

[109] Allen, M. P.; Tildesley, D. J. *Computer Simulation of Liquids*; Oxford science publications; Oxford University Press, USA, 1989.

[110] Mondal, A.; Balasubramanian, S. *J. Phys. Chem. B* **2014**, *118*, 3409–3422.

[111] Mondal, A.; Balasubramanian, S. *J. Phys. Chem. B* **2015**, *119*, 11041–11051.

[112] Nosé, S. *J. Chem. Phys.* **1984**, *81*, 511–519.

[113] Hoover, W. G. *Phys. Rev. A* **1985**, *31*, 1695–1697.

[114] Mayo, S. L.; Olafson, B. D.; Goddard, W. A. *J. Phys. Chem.* **1990**, *94*, 8897–8909.

[115] Frenkel, D., Smit, B., Eds. *Understanding Molecular Simulation: From Algorithms to Applications*, 1st ed.; Academic Press, Inc.: Orlando, FL, USA, 1996.

[116] Hansen, J.-P.; McDonald, I. R. *Theory of Simple Liquids, Third Edition*, 3rd ed.; 2006.

[117] Park, S.; Khalili-Araghi, F.; Tajkhorshid, E.; Schulten, K. *J. Chem. Phys.* **2003**, *119*, 3559–3566.

[118] Darve, E.; Pohorille, A. *J. Chem. Phys.* **2001**, *115*, 9169–9183.

[119] Torrie, G.; Valleau, J. *J. Comput. Phys.* **1977**, *23*, 187 – 199.

[120] Laio, A.; Parrinello, M. *Proc. Natl. Acad. Sci.* **2002**, *99*, 12562–12566.

[121] Awasthi, S.; Kapil, V.; Nair, N. N. *J. Comput. Chem.* **2016**, *37*, 1413–1424.

[122] Fiorin, G.; Klein, M.; Hénin, J. *Mol. Phys.* **2013**, *111*, 3345–3362.

[123] Jarzynski, C. *Phys. Rev. Lett.* **1997**, *78*, 2690–2693.

[124] Plimpton, S. *J. Comput. Phys.* **1995**, *117*, 1 – 19.

[125] Hutter, J.; Iannuzzi, M.; Schiffmann, F.; VandeVondele, J. *Wiley Interdiscip. Rev.: Comput. Mol. Sci.* **2014**, *4*, 15–25.

[126] Frisch, M. J. et al. Gaussian 09 Revision D.01. Gaussian Inc. Wallingford CT **2009**.

Chapter 2

Supramolecular Polymerization of Benzene-1,3,5-tricarboxamide: A Molecular Dynamics Simulation Study

2.1 Introduction

One of the molecules studied extensively in supramolecular chemistry is benzene-1,3,5-tricarboxamide (BTA), with a C_3 symmetric structure around a benzene ring core, as shown in Figure 2.1. BTA, with pentyl or longer alkyl tails exhibits a liquid crystalline phase [1]. The self-assembly of BTA derivatives in apolar solvents such as heptane and methylcyclohexane have been extensively studied by Meijer and co-workers [2–8]. BTA exists in monomeric form at high temperature and self-assembles in a cooperative fashion upon cooling to yield one-dimensional, helical columnar stacks.

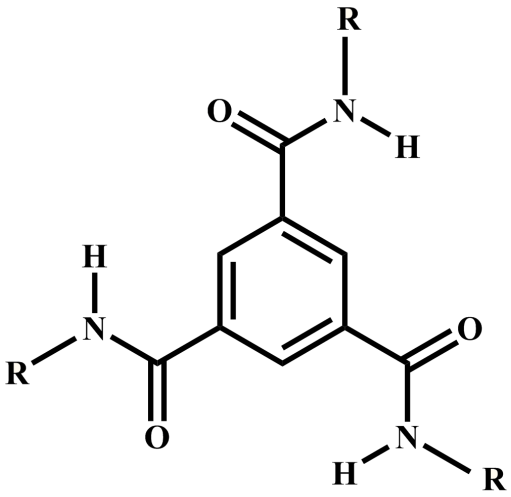

Figure 2.1: Benzene-1,3,5-tricarboxamide. **1a**: R=H **1b**: R=-$(CH_2)_2CH_3$ **1c**: R=-$(CH_2)_5CH_3$

Although the monomer is planar and hence has zero dipole moment, intermolecular C=O$\cdots$H-N hydrogen bonds between molecules present in an oligomer necessitates the amide and the carbonyl groups of a given molecule to orient themselves in opposite directions of the molecular plane, thus generating a molecular dipole moment. As the dipoles of individual molecules are oriented along the same direction, the magnitude of the total dipole moment of the stack (a macrodipole) increases with stack size. Stacks have been conjectured to interact *via* dipole-dipole forces to result in fibers [9].

Despite the large number of experimental studies on supramolecular polymers and a good number devoted to their mechanisms of assembly, there have been only a few theoretical studies. Gas phase quantum chemical calculations have shown the specific interactions responsible for oligomerization. Accurate calculations are prohibitively expensive due to the large number of atoms in a BTA molecule, and are thus limited to oligomers not exceeding a dodecamer [9, 10]. Cooperativity has been demonstrated in hydrogen bond lengths, torsional angles and binding energies. However, these gas phase zero Kelvin calculations need to be supplemented by finite temperature simulations which include the solvent as well. Molecular dynamics

(MD) is a powerful tool to explore the self-assembly at the molecular level [11–17]. Force field based MD simulations have been carried out to model supramolecular systems including a C_3 symmetric BTA based compound [18], anionic azo dye [19] and bis-urea [20]. MD simulations can reveal aggregation mechanisms, structural details, relative importance of various interactions, energetics, and temperature effects on columnar stacking. In this article, we provide results of atomistic MD simulations of BTA in a solvent of *n*-nonane. In anticipation of our results, we provide microscopic details of stack formation, signatures of cooperativity, and the role played by the dipole moment of the hydrogen bond in the structure of a column. The MD simulations have also been augmented by quantum chemical calculations to determine the exact configuration of hydrogen bond dipoles in oligomers. We have also determined the free energies of solvation and dimerization of these molecules in solution and have investigated self-assembly into stacks. The dynamics of pre-formed stacks have also been investigated.

2.2 Computational Details

The DREIDING force field [21] is employed to describe BTA molecules. In addition to a specific hydrogen bonding potential term, the force field offers specific potential types in which the atomic sites either contain a partial charge or not, hereinafter referred to as DREIDING-C and DREIDING-N respectively. In the former, Gasteiger charges [22] are identified on atomic sites.

$$E = \sum^{bond} K_r(r - r_o)^2 + \sum^{angle} K_\theta(\theta - \theta_o)^2 + \sum^{dihedral} K(1 - \cos[n(\phi - \phi_o)]) + \sum^{inversion} K(1 - \cos\phi) + E_{nb} \qquad (2.1)$$

$$
\begin{aligned}
E_{nb} &= E_{vdW} + E_Q + E_{hb} \\
E_{vdW} &= A\exp(-Cr_{ij}) - B/r_{ij}^6 \\
E_Q &= q_i q_j/(4\pi\epsilon_o r_{ij}) \\
E_{hb} &= D_{hb}[5(R_{hb}/R_{DA})^{12} - 6(R_{hb}/R_{DA})^{10}]\cos^4(\theta_{DHA})
\end{aligned}
\tag{2.2}
$$

here, E_{hb} is a three-body term that is used to describe hydrogen bond interactions.

In our simulations, BTA molecules were considered in an all-atom representation. All the simulations were performed with the MD program LAMMPS [23] at a temperature of 298.15 K maintained through the use of a Nosé-Hoover chain thermostat [24, 25] with a coupling constant of 1 ps. Three-dimensional periodic boundary conditions were applied on either cubic or orthorhombic boxes depending on the nature of the system. Non-bonded interactions were truncated at 12 Å. Long-range Coulombic interactions were treated using the particle-particle particle-mesh (PPPM) [26] solver. Long range corrections to energy and pressure were applied. Full scaling of 1-4 interactions was employed. Free energy calculations were carried out with a time step of 0.5 fs using the velocity-Verlet algorithm with *n*-nonane as solvent and the latter was modelled using the all-atom DREIDING-N model. In regular MD simulations (i.e., ones which did not involve free energy calculations), the TraPPE united atom model [27] of *n*-nonane was employed to reduce computational cost. Cross interactions between BTA and solvent were handled using DREIDING's mixing rules. In these runs, the multiple time step method, r-RESPA [28] was employed. The outer time step was 1 fs while all bond stretches were integrated with a time step of 0.5 fs. VMD [29] was used for visualization.

2.2.1 Adaptive Biasing Force (ABF)

Free energy (FE) calculations have been employed in a variety of problems – to determine stable structures, to overcome barriers, and in particular to predict the

energy difference between two states. Herein, FE profiles are obtained using the 'colvars' (collective variable) module [30] integrated with LAMMPS. Adaptive Biasing Force (ABF) [31] is a FE technique which employs the application of an external force on the system to explore the configurational space. In the ABF method, the force experienced on the reaction coordinate (RC) is averaged over a given number of steps ($N_{samples}$). ABF applies an external biasing force (F_{ABF}), which is exactly opposite to this average force $\langle F \rangle$, so as to smoothen the potential surface for uniform sampling. The full window of the RC is divided into smaller bins in each of which accumulation of force takes place. The width of each bin should be small enough to capture the variations in FE, but large enough to permit good statistics. In our simulations, the total RC was divided into non-overlapping windows to improve the sampling and the convergence of FE. The initial configurations for these windows were obtained from steered molecular dynamics (SMD) simulations [32]. Jacobian terms were included in all the FE calculations.

2.2.2 Dimerization free energy (DFE)

DFE represents the FE for the formation of a dimer from two separated monomers present either in gas phase or in solution, at a given temperature. Here, the RC is defined as the distance between the center of mass of the two molecules, excluding their alkyl groups.

Gas phase: Two BTA molecules in their dimerized state were placed in a cubic box of edge length 100 Å, large enough to avoid image interactions. The total RC, spanning from 2.5 Å to 26.5 Å was divided into four non-overlapping windows. $N_{samples}$ was chosen to be 200 and the bin width was set to 0.1 Å. The biasing force was obtained as an average over 200 steps.

Bulk phase: Two BTA molecules in their dimerized state were solvated in a pre-equilibrated box containing *n*-nonane molecules. Molecules of the solvent having hard contacts with the solute were removed. The RC was split into four non-overlapping

windows, each of 3.5 Å width so as to span the distance from 2.5 Å to 16.5 Å. $N_{samples}$ was chosen to be 1000 so as to provide sufficient time for the solvent molecules to equilibrate. The bin width to accumulate the force was chosen to be 0.1 Å. Simulations were carried out in the constant isothermal-isobaric (NPT) ensemble.

2.2.3 Solvation free energy (SFE)

150 *n*-nonane molecules were equilibrated in a cubic box under constant NPT conditions. The box length along the z-direction was later increased to 200 Å which created two liquid-vapor interfaces. Simulations to calculate the SFE of BTA in this solvent were performed subsequently in the canonical (NVT) ensemble. The RC was defined as the distance between the center of mass of all the nonane molecules and the lone BTA molecule (excluding its alkyl tails). The span of RC was chosen sufficiently large to ensure that the molecule was completely immersed in the solvent at one end and completely in vacuum at the other end of the RC. SFE is the difference in energy between the two plateaus. The RC spanned from 0 Å (center of nonane box) to 45 Å and was divided into five non-overlapping windows each of width 9 Å. The colvar style of 'distanceZ' was used to apply the force normal to the liquid surface. ABF parameters used were 1000 for $N_{samples}$, and 0.2 Å for bin width.

2.3 Results & Discussion

2.3.1 Gas phase oligomers: Comparison between force field and quantum data

As mentioned before, the monomer of **1a** is planar, while in an oligomer, the oxygen and amide hydrogens of a given molecule are oriented towards either side of the benzene plane, to form three intermolecular hydrogen bonds. The rotation of the amide group around the benzene ring is about 45° [33], which gives rise to a tiny but, non-negligible dipole moment. Such molecular dipole moments in a stack add up to impart a macrodipole along the stacking direction in an oligomer.

The geometries of oligomers of **1a** in gas phase, optimized with the DREIDING force field are compared in Table 2.1 against those determined by quantum chemical calculations [10]. Values of the hydrogen bond distance, π-π stacking distance, dihedral angles of the central core, binding energies, and the mean dipole moment per molecule of the oligomer are also provided. The latter was calculated as the ratio of the total dipole moment (macrodipole) of the oligomer to the oligomer size. Both DREIDING-C & DREIDING-N are able to provide a good account of many geometrical parameters. However, DREIDING-N slightly overestimates and DREIDING-C underestimates the binding energy compared to quantum chemical results. Interestingly, DREIDING-C, despite being a non-polarizable force field, is able to demonstrate cooperativity in the dependence of binding energy per molecule on stack size (Figure 2.2). Cooperativity was also observed across dihedral, hydrogen bond, Coulombic and van der Waals energies. The binding energy of the stack converges to values of -22.1 kcal/mol and -31.6 kcal/mol using DREIDING-C and DREIDING-N force fields respectively in comparison to a value of -27.1 kcal/mol obtained using PBE+vdW [10].

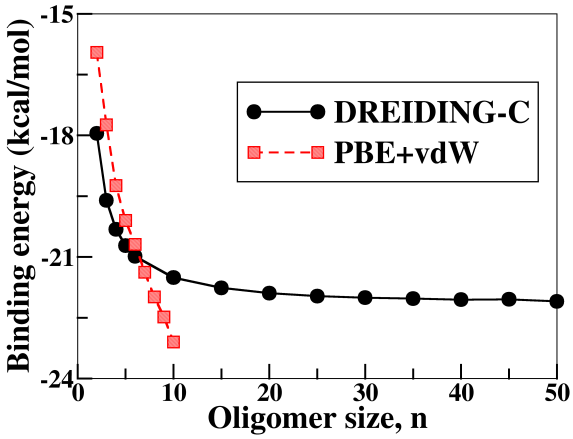

Figure 2.2: Binding energy (see Table 2.1 for definition) of geometry optimized oligomers as a function of their size n, obtained using DREIDING-C force field and PBE+vdW level of theory [10].

Table 2.1: Comparison of geometries of BTA oligomers optimized in gas phase using DREIDING force field and quantum density functional theory. Binding energy is defined as $\frac{E_n - nE_1}{(n-1)}$, where E_n is the energy of an oligomer of size n. Geometrical parameters pertain to the core region of an oligomer.
'*' Dipole moments of oligomers optimized with DREIDING-N were calculated using DREIDING-C charges.

Oligomer size (n)	Stacking distance (Å)	H-bond distance (Å)	O-C-C_{Ar}-C_{Ar} dihedral angle (degree)	H-N-C_{Ar}-C_{Ar} dihedral angle (degree)	Binding energy (kcal/mol)	Dipole moment per molecule* (D)
DREIDING-N						
2	3.44	1.84	36.9	38.2	-30.1	4.42
3	3.44	1.84	43.4	40.3	-30.9	4.50
5	3.45	1.84	42.2	39.1	-31.3	4.63
6	3.44	1.84	42.3	39.2	-31.4	4.65
10	3.44	1.84	42.2	39.1	-31.5	4.64
DREIDING-C						
2	3.31	1.89	9.4	35.6	-17.9	2.36
3	3.31	1.87	25.3	41.4	-19.6	2.91
5	3.31	1.86	24.4	39.8	-20.7	3.33
6	3.31	1.85	24.6	39.8	-21.0	3.43
10	3.32	1.85	24.8	39.9	-21.5	3.64
15	3.32	1.85	24.9	40.1	-21.7	3.75
20	3.32	1.85	24.9	40.0	-21.9	3.80
30	3.29	1.86	24.8	39.4	-22.0	3.83
40	3.33	1.85	25.0	40.2	-22.0	3.86
50	3.33	1.85	25.0	40.3	-22.0	3.89
PBE+vdW	3.72	1.82	36.8 [34]	42.4 [34]	-27.1	12.35

2.3.2 Columnar stack in solvent: stability

Prior to the exploration of self-assembly of BTA molecules, we need to evaluate the capability of the force field in maintaining the stability of a pre-built columnar stack in bulk solvent at a finite temperature. Towards this purpose, a MD simulation of a three-fold hydrogen bonded oligomer (of size 20) of **1c**, solvated in *n*-nonane was carried out at 298.15 K for a duration of 10 ns using both DREIDING-C & DREIDING-N force fields. Configurations were saved every 5 ps for visualization and

analyses. All hydrogen bonds were found to be intact throughout the simulation in both the runs implying that the force field adopted here could reasonably represent this system. Figure 7.1(a) exhibits a typical snapshot of this 20-mer near the end of this run. Three BTA molecules present within this stack are highlighted in 7.1(b).

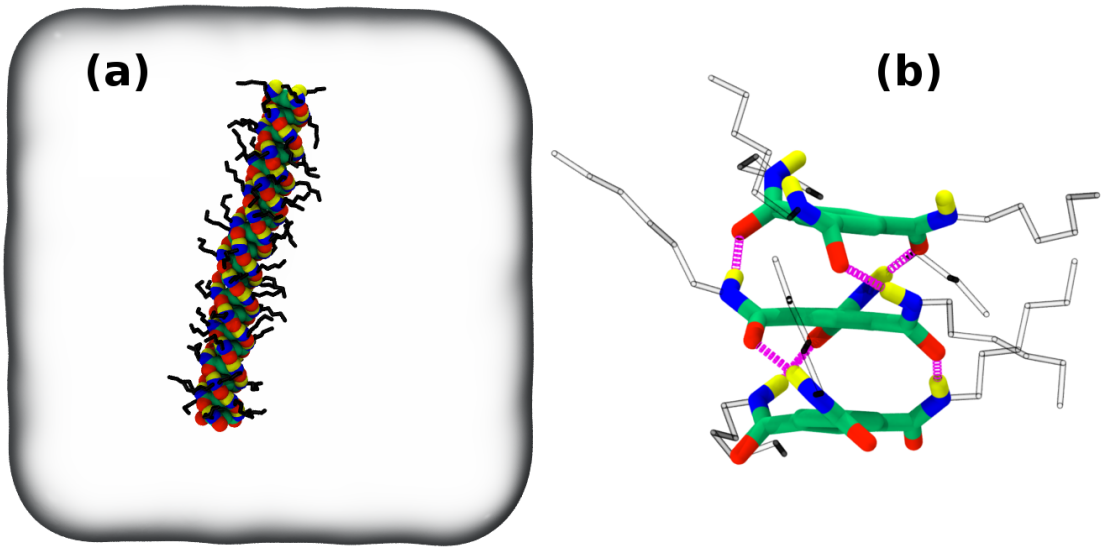

Figure 2.3: (a) Snapshot of a 20-mer of **1c** solvated in *n*-nonane at 298.15K taken from a MD run employing the DREIDING-C force field. (b) Three adjacent molecules taken from the center of the stack. Hydrogens on the alkyl tails are not shown for clarity. Color scheme: carbon-green, oxygen-red, nitrogen-blue, hydrogen-yellow, carbon (tail)-black. Dashed lines are hydrogen bonds. Note the opposite orientations of the carbonyl oxygens and amide hydrogens of a given molecule, with respect to the molecular plane. Intermolecular hydrogen bonds thus formed are aligned along the stack direction, imparting a macrodipole to the stack. The directions of the hydrogen bond dipole moment vector and that of the macrodipole of the stack are opposite to each other.

2.3.3 Cooperativity in bulk solvent

MD simulations of oligomer stacks of various sizes, each solvated in a box containing 5,457 *n*-nonane molecules were carried out at 298.15 K. In all, simulations of thirteen different stacks (of 3:0 type) were carried out. Each system was simulated under constant NPT conditions for at least 3 ns. In a given configuration along the MD run, the potential energy of each BTA molecule was calculated as the sum of its interaction energy with other BTA molecules and with those of the solvent. The value was then

averaged over all the BTA molecules in the stack. The mean potential energy of a molecule in a stack is plotted against oligomer size in Figure 2.4. Such simulations, carried out in bulk conditions and at finite temperature are a more robust check of cooperative behavior of self-assembly than gas phase, zero Kelvin calculations. The potential energy per molecule of a BTA stack displays a dependence on the oligomer size prior to saturation, illustrating the cooperative behavior of aggregation as seen in Figure 2.4. In fact, in a large enough stack, the potential energy of a molecule present in the core of the stack is more negative (i.e., more stabilized) than for one present in its periphery. This too is an evidence of cooperativity.

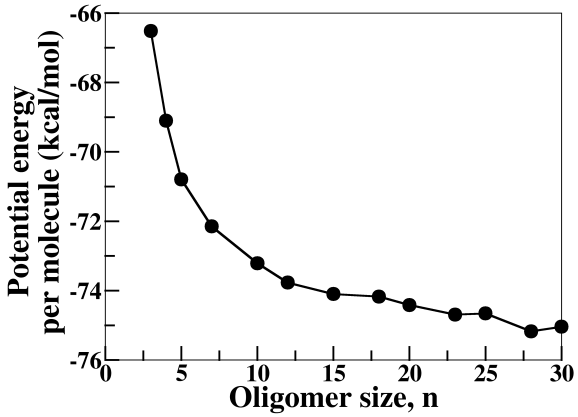

Figure 2.4: Cooperativity exhibited by mean potential energy per BTA molecule of oligomers of **1c** solvated in bulk *n*-nonane at 298.15 K.

2.3.4 Supramolecular aggregation

To understand the mechanism of self-assembly, we solvated 10 molecules of **1c** in a box containing 1,500 *n*-nonane molecules. The initial configuration contained BTA molecules placed randomly in this simulation box, using Packmol [35]. MD simulations were performed under constant NPT conditions at 298.15 K and coordinates were saved every 5 ps. A few snapshots illustrating the self-assembly process are shown in Figure 2.5. The monomers self-assemble to form small oligomers which coalesce to form a longer columnar stacks. Earlier experiments [36, 37] and computations [10, 38] have proposed that the stacks are constituted by molecules whose NH groups are all

oriented in one direction and the carbonyl oxygen atoms in the other direction, with respect to the benzene plane.

However, in our MD simulations, the molecules in the stack were found to have two amide NH groups and one carbonyl oxygen to be oriented along the same direction. Thus, each molecule participates in three intermolecular hydrogen bonds in a given direction; two of them are of donor type and one of acceptor type (or *vice versa*). At first sight, it may appear that this configuration may be metastable with respect to the one in which all acceptor hydrogen bonds of a molecule are oriented along the same direction. However, we observe (*vide infra*) that this configuration is indeed more stable than the one in which all the three amide NH groups form hydrogen bonds with the same molecule adjacent to it in the stack.

For now, let us define the configurations as follows:

(i) Symmetric: Three amide NH groups of a molecule oriented along the same direction (hereinafter referred to as 3:0). A dimer of this type is shown in Figure 2.6a.

(ii) Asymmetric: Two amide NH groups of a molecule oriented along one direction and the third in the opposite direction (hereinafter referred to as 2:1). A dimer of this type is shown in Figure 2.6b.

Once a 2:1 dimer is formed, any other molecule hydrogen bonds to this dimer in the same asymmetric fashion resulting in a columnar stack which is entirely constituted by hydrogen bonds of the 2:1 type. Such stacks were formed in simulations carried out with either DREIDING-N and DREIDING-C force fields. The only manner in which an initially established 2:1 character cannot propagate is through a defect – a site where there are fewer than three intermolecular hydrogen bonds.

Could the formation of stacks in the 2:1 configuration be due to inadequate sampling or inadequacy of force fields? In the following, we examine this question and show that it is indeed more stable energetically than the 3:0 configuration.

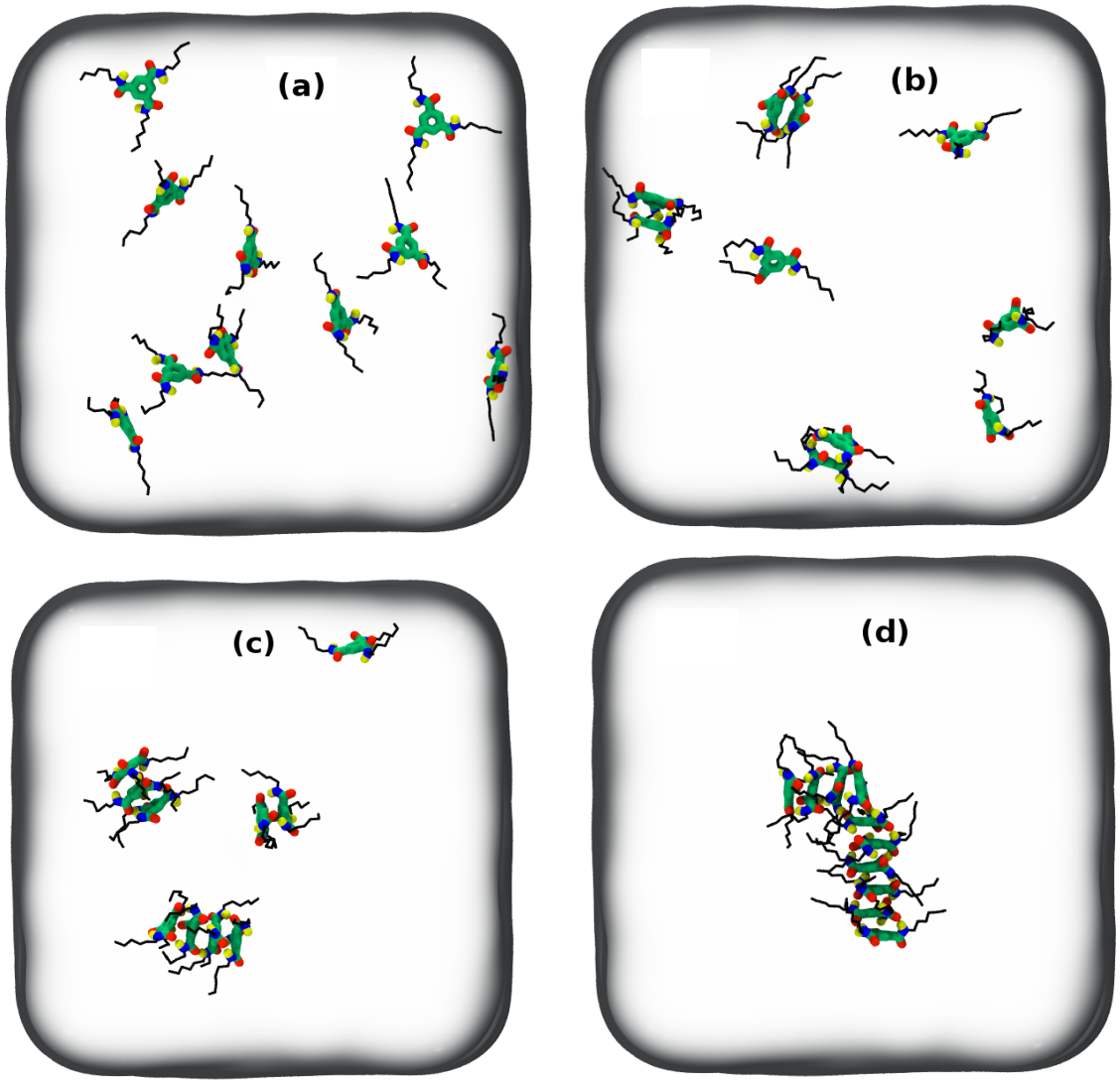

Figure 2.5: Snapshots exhibiting the progress of supramolecular self-assembly of **1c** in *n*-nonane starting from a random configuration at (a) 0 ns, (b) 2 ns, (c) 6.5 ns, and (d) 70 ns respectively, studied using DREIDING-C force field. Color scheme is the same as in the Figure 7.1.

2.3.5 Investigations of 2:1 stacks

Gas-phase calculations

Gas phase, zero Kelvin calculations of binding energies of geometry optimized oligomers of 2:1 and 3:0 stacks can provide an idea of their intrinsic stabilities. These were carried out using both varieties of DREIDING force field and the results are displayed in Table 2.2. Binding energies are marginally larger for the 2:1 stack

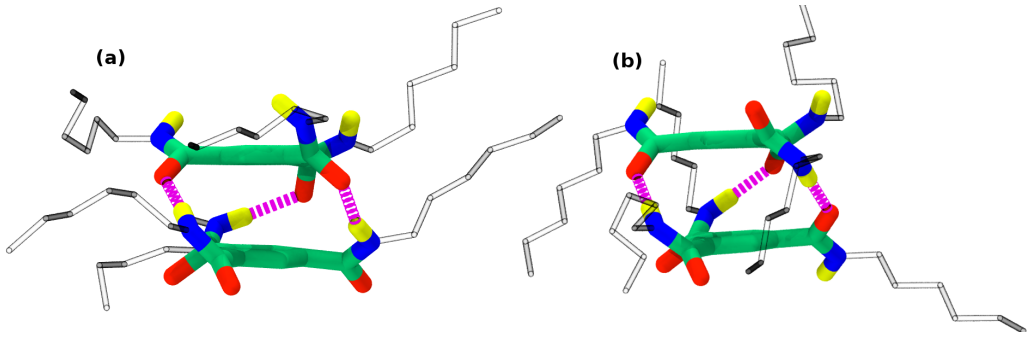

Figure 2.6: Two different configurations of **1c** dimer (a) 3:0 (alias symmetric) and (b) 2:1 (alias asymmetric).

compared to that for the 3:0 stack. Both stacking patterns exhibit cooperativity in binding energy as shown in Figure 2.7.

Table 2.2: Binding energies (in kcal/mol) of geometry optimized oligomers of **1a** in 3:0 and 2:1 stacking configurations obtained using DREIDING-N and DREIDING-C force fields.

Oligomer size (n)	DREIDING-N		DREIDING-C	
	3:0	2:1	3:0	2:1
2	-30.1	-30.5	-17.9	-17.2
3	-30.9	-31.2	-19.6	-19.9
4	-31.2	-31.4	-20.3	-20.8
5	-31.4	-31.5	-20.7	-21.2
6	-31.4	-31.6	-20.9	-21.5
10	-31.6	-31.7	-21.5	-21.9
15	-31.7	-31.8	-21.7	-22.1
20	-31.7	-31.8	-21.8	-22.2
25	-31.7	-31.8	-21.9	-22.3
30	-31.7	-31.8	-22.0	-22.3
40	-31.6	-31.8	-22.0	-22.4

Quantum chemical calculations

It is interesting that in both varieties of the DREIDING force field, the binding energies of a 2:1 stack are marginally higher (in magnitude) than the corresponding 3:0 one. Earlier quantum chemical studies had exclusively examined the 3:0 stacks only [10, 38, 39]. Thus, we have carried out gas phase density functional theory (DFT) based quantum chemical calculations at B3LYP/6-311+g(d,p) level of theory

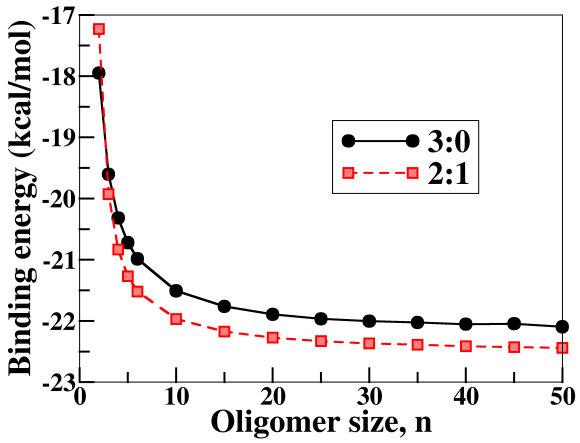

Figure 2.7: Cooperativity in binding energy exhibited by gas-phase geometry optimized oligomers of **1a** for 3:0 and 2:1 types of stacking obtained using DREIDING-C force field.

for a few oligomers of **1a** in both 2:1 and 3:0 configurations using Gaussian-09 [40] and NWChem [41]. While the M06-2X + DFT-D3 calculations were carried out using NWChem, the B3LYP ones were performed using Gaussian-09 [40]. Table 2.3 shows the binding energy of geometry optimized 2:1 oligomers to be larger than that of 3:0 stacks at both the levels of quantum theory, consistent with the results from the DREIDING force fields.

Table 2.3: Energy difference ($E_{3:0}$ - $E_{2:1}$) (in kcal/mol) between optimized geometries of 3:0 and 2:1 type BTA oligomers.

Oligomer size (n)	B3LYP/6-311+g(d,p)	B3LYP/6-311+g(d,p) // B3LYP/cc-pVTZ	B3LYP/6-311+g(d,p) // M06-2X/cc-pvTZ + DFT-D3
R=Hydrogen			
2	2.82	2.35	1.67
3	8.06	7.58	7.45
4	11.60	11.31	10.28
R=Methyl			
2	2.52	2.07	0.62
3	7.94	7.48	6.37
4	11.55	11.29	10.36

The replacement of an amide proton with a methyl group does not effect the relative stabilities of the two stacking types and the 2:1 dimer is found to be more stable than the 3:0 one by 2.52 kcal/mol at B3LYP/6-311+g(d,p) level of theory. In

an earlier study, Schmidt and co-workers compared the heats of formation for the two types of stacks using a semiempirical PM6 model [9]. For the BTA trimer with methyl tails, they observed the heat of formation for the 2:1 stacking type to be greater than that of the 3:0 one by around 7.17 kcal/mol, which is very much consistent with results from our DFT calculations. The above analyses show that oligomers of the 2:1 type are more stable than the corresponding 3:0 stacks. Furthermore, for a given length of the alkyl tail of BTA, the difference in stability increases with oligomer size.

The stability of the 2:1 oligomer relative to that of the 3:0 one can be explained as follows: Each intermolecular hydrogen bond possesses a dipole moment oriented from the carbonyl oxygen of one molecule to the amide hydrogen of another. Classical electrostatic interaction between these dipoles demands an anti-parallel arrangement to be the energetically favored configuration. Given that there are three hydrogen bonds between a pair of molecules, not all the three dipole-dipole configurations can be anti-parallel, a situation which is similar to the frustrated antiferromagnetic configuration of spins on a triangular lattice. Thus, one hydrogen bond dipole flips to provide two anti-parallel interactions. This is one of the causes for the stabilization of the 2:1 stack and the same was alluded earlier by Schmidt and co-workers [9]. The difference in the energies of a 3:0 and a 2:1 dimer should thus be 4E, where E is the dipole-dipole interaction energy between proximal intermolecular hydrogen bonds. Based on the atom charges (of DREIDING force field) and the distances in the optimized dimer configurations, we estimate E to be around 0.25 kcal/mol. Thus, the difference in energies between 3:0 and 2:1 dimers is estimated to be around 1.0 kcal/mol which is in the same scale as the value of 3.46 kcal/mol, the difference between 3:0 and 2:1 dimer energies. The odd number of dipoles in a C_3 symmetric molecule results in an unavoidable frustration in dipole orientation. On the other hand, for a C_2 symmetric molecule [42, 43] even number of dipoles can arrange in alternate up-down fashion to favour dipolar interactions.

The energy difference between the two kinds of dimers will depend on the length

of the alkyl tail. To investigate this aspect, dimers of 2:1 and 3:0 types for different alkyl tail lengths were geometry optimized. The difference in the energies between the two dimers decreases with increasing tail length up to a length of four, beyond which it saturates to a value around 2 kcal/mol (favoring the 2:1 configuration) as shown in Table 2.4. The energy difference between the two stacking types can be attributed to differences in the van der Waals interactions between the tails. The most favored distance between intermolecular CH_2 groups in *n*-alkanes is 4.5 Å. 2:1 type stacking has fewer CH_2 pairs at such a distance than the 3:0 one. This difference is the underlying reason for the decrease in the relative stability of the 2:1 dimer over the 3:0 one. However, since the alkyl groups attached to the two molecules in a dimer have a relative angle of 60^o (see Figure 2.6), this difference in CH_2 pair distances does not propagate beyond four carbon atoms in the alkyl chain. Thus, the $E_{3:0}$-$E_{2:1}$ saturates beyond R=butyl. Inclusion of zero-point energy (ZPE) for the dimers with R=H and R=Me does not significantly alter the energy difference. $E_{3:0}$-$E_{2:1}$ including the ZPE reduces marginally to values of 2.26 kcal/mol (R=H) and 2.13 kcal/mol (R=Me). The free energy difference (with contributions from vibrational, rotational and electronic degrees of freedom) at 298.15 K calculated within B3LYP/6-311+g(d,p) level of theory too favors the 2:1 dimer for both R=H (+1.76 kcal/mol) and R=Me (+1.52 kcal/mol). Thus, it is likely that the stability of the 2:1 dimer over the 3:0 one observed here is reliable.

Table 2.4: Energy difference ($E_{3:0}$ - $E_{2:1}$) (in kcal/mol) between geometry optimized dimers of BTA possessing different alkyl tails using B3LYP/6-311+g(d,p) level of theory.

Alkyl tail (R)	ΔE
Hydrogen	2.82
Methyl	2.52
Propyl	1.87
Butyl	1.87
Pentyl	2.13

Crystal structures [44–46] of BTA with *n*-alkyl tails (n=1, 2, 3 and 8) exhibit

sheet-like geometries instead of the one-dimensional structures expected in solution and studied herein. Thus, a direct comparison of the 2:1 stacking type with the molecular packing in the crystal is not possible. Only one crystal structure with one-dimensional stacking feature is known, but for R=Methoxyethyl. This structure exhibits three fold hydrogen bonds between π stacked molecules and the hydrogen bonds are of 3:0 type [34]. We presume that the ether linkage is responsible for the stabilization of the 3:0 geometry in this case.

2.3.6 2:1 and 3:0 stacks in solvent

MD simulations of a 20-mer stacked in either 2:1 or 3:0 fashion were carried out in bulk *n*-nonane at 298.15 K in the NPT ensemble for a duration of 5 ns. Intermolecular hydrogen bonds in both the stacks were seen to be preserved in these simulations. Thus, the nature of the stack (i.e., either 2:1 or 3:0 type) did not change during the course of the MD trajectory. The mean potential energy of a molecule in a stack was calculated as described earlier and is shown in Figure 2.8 as a function of time. Again, a molecule belonging to the 2:1 stack is found to be more stable than one present in the 3:0 one. The mean potential energy difference between a molecule present in these stacks is around 11.5 kcal/mol at ambient conditions. It is to be noted that a 2:1 stack can be realized in three different ways versus the single realization of a stack in the 3:0 manner (see Figure 2.9). Thus, the former is stabilized by entropic grounds, in addition to energetic reasons, making the 2:1 stack to be thermodynamically more stable than the corresponding 3:0 stack. Further, macrodipole of the two variants of stacks was determined and shown in Figure 2.8b. It fluctuates in time about a mean value, due to its flexibility and as expected, the 3:0 stack possesses a larger dipole moment (almost thrice) than the 2:1 stack. The amplitude of fluctuations will decrease with increase in stack size.

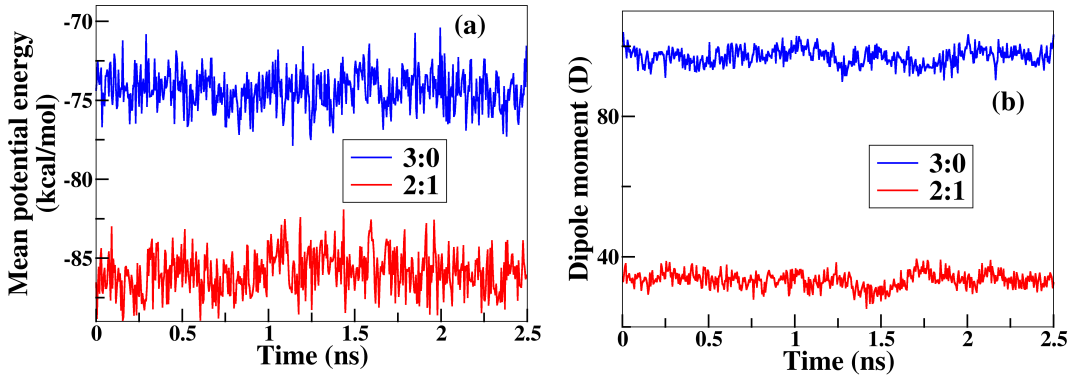

Figure 2.8: (a) Mean potential energy of a molecule present in a 20-mer solvated in *n*-nonane at 298.15 K. (b) Macrodipole moment of an oligomer size 20 in 3:0 and 2:1 type stacking structures.

Dihedral barrier between asymmetric and symmetric configurations

We have also performed calculations to estimate the dihedral barrier for the transformation of a molecule between the 3:0 and 2:1 structures. A molecule in the 2:1 configuration can be created from a 3:0 one by the rotation of the bond connecting the benzene ring to the carbonyl group. The ABF method was employed to obtain the free energy profile with respect to this dihedral angle over the range -180° to 180°, with a 5° bin width for a monomer of **1c** in both gas-phase and in bulk nonane (see Figure 2.10a). In both phases, the torsional barrier is sufficiently low (around 1 to 1.5 kcal/mol), implying that the bond rotation could be facile at ambient conditions. It is also noted that the effect of solvent on the torsional free energy profile is not significant. Furthermore, we observed that the barrier height does not depend on whether **1c** possessed only one alkyl group, instead of three. Thus, intramolecular tail-tail interaction does not seem to determine the barrier height. The low barrier is due to the formation of a weak intramolecular 'hydrogen bond' between the hydrogen of a methylene group and the carbonyl oxygen. To confirm the force field calculations, the torsional barrier of the compound with one hexyl group was also determined at B3LYP/6-311+g(d,p) level of theory, *via* a relaxed scan of this dihedral angle, using Gaussian-09. The barrier calculated using DREIDING-C at zero Kelvin was found to

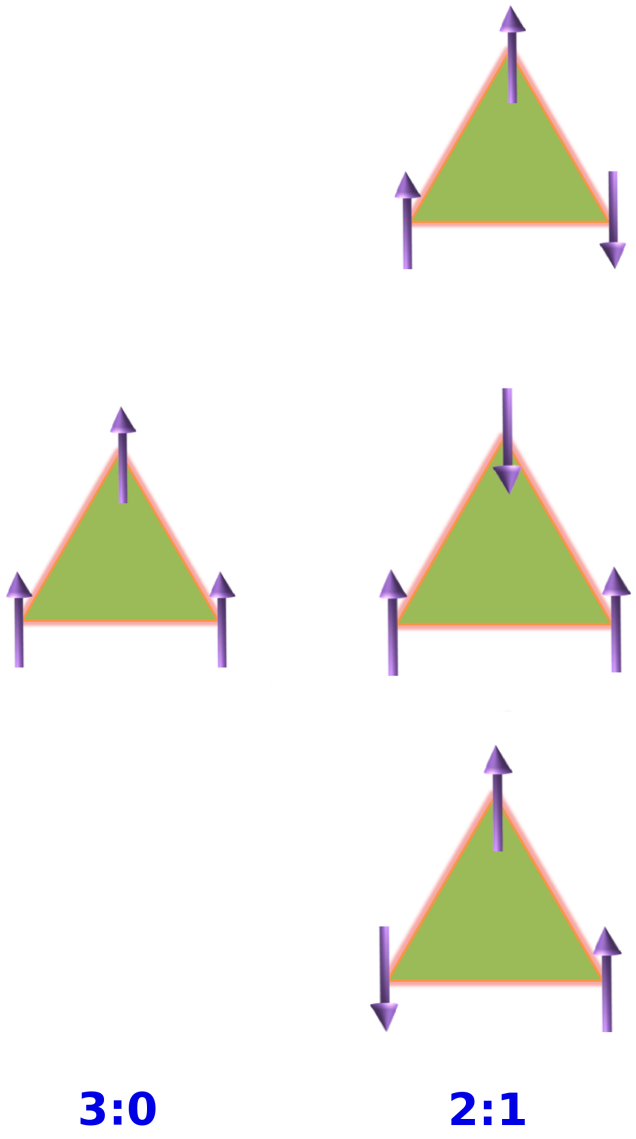

Figure 2.9: Possible dipole orientations in 3:0 and 2:1 configurations.

be in agreement with the DFT result as shown in Figure 2.10b.

2.3.7 Free energy calculations

Dimerization in gas phase and in bulk solvent

The FE of dimerization in gas phase was calculated in the NVT ensemble at 298.15 K using both varieties of the DREIDING force field. As mentioned earlier, the RC was split into four windows and MD simulations were carried out for 25 ns in each window to ensure the convergence of FE. The gas phase DFE profiles of **1a**, **1b**,

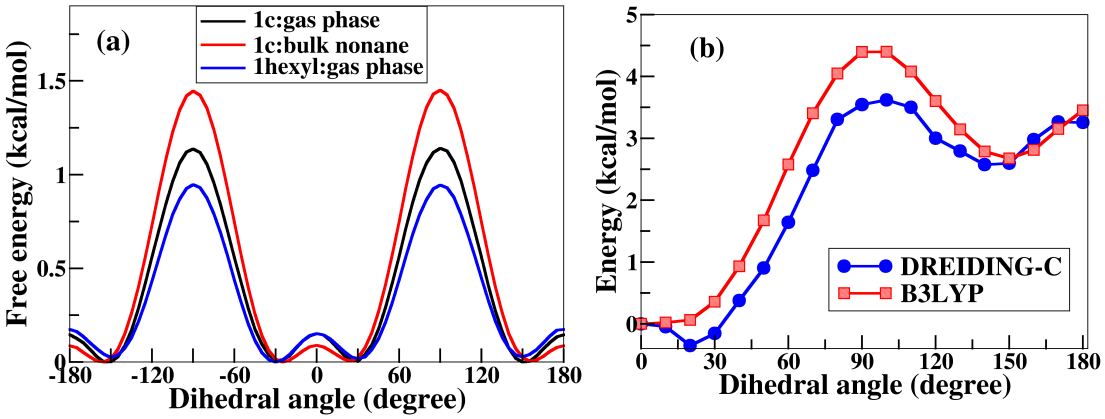

Figure 2.10: Free energy as a function of dihedral angle of the bond between the benzene carbon and the carbonyl carbon calculated at 298.15 K; Compound marked "1hexyl" is similar to **1c**, but with only one hexyl group instead of three. (b) Comparison of the dihedral barrier obtained using DREIDING-C force field and B3LYP/6-311+g(d,p) level of theory for the compound marked "1hexyl".

and **1c** are shown in Figure 2.11 and the values are given in Table 2.5.

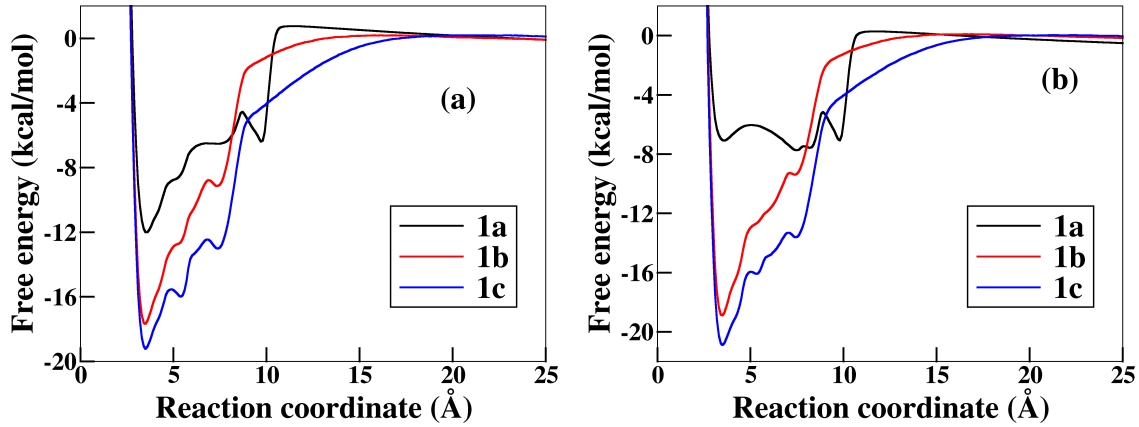

Figure 2.11: Dimerization free energy profiles of BTA molecules in gas phase at 298.15 K studied using (a) DREIDING-N and (b) DREIDING-C force fields.

Increasing the length of the alkyl chain results in increase in the stabilization of the dimer with respect to two monomers, as studied through both DREIDING-N and DREIDING-C force fields. The dimer of **1a** in gas phase is found to be not stable within the DREIDING-C force field. The force field has a specific potential term for the hydrogen bond interaction which contains an inner and outer distance cutoff.

The oscillations in the profiles are due to the break in the intermolecular hydrogen bonds, and the consequent inactivation of this potential term.

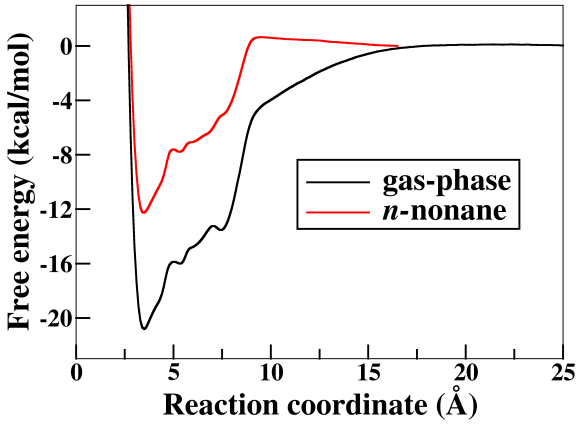

Figure 2.12: Comparison of dimerization free energy profiles of **1c** in gas-phase and in bulk *n*-nonane at 298.15 K.

To determine the DFE in *n*-nonane, MD simulations were carried out in the constant NPT ensemble at 298.15 K. Each window was run for 35 ns, and a total trajectory 140 ns was generated to obtain the FE profile for **1c**. The dimerization FE in solvent is smaller than that in gas phase, as expected. Further, solvent molecules penetrate between the two BTA molecules which results in the realization of the monomer state at a shorter distance compared to that in gas phase (see Figure 2.12).

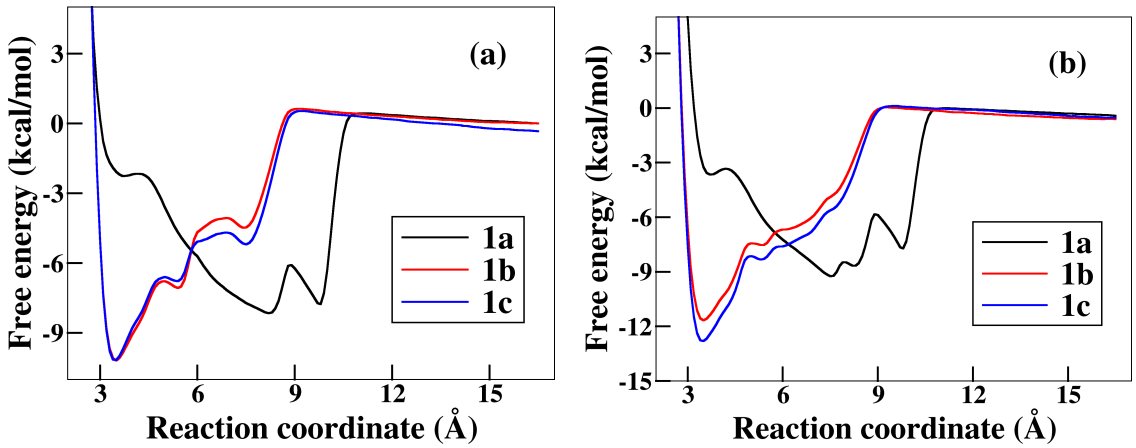

Figure 2.13: Dimerization free energy profiles in bulk *n*-nonane at 298.15 K obtained using (a) DREIDING-N and (b) DREIDING-C force fields.

Table 2.5: Dimerization (DFE) and solvation free energies (SFE) (in kcal/mol) of **1a**, **1b**, **1c** at 298.15 K.

Molecule	DREIDING-N	DREIDING-C
DFE (gas phase)		
1a	-12.01	-7.08
1b	-17.68	-18.90
1c	-19.22	-20.90
DFE (in *n*-nonane)		
1a	-8.15	-9.24
1b	-10.17	-11.67
1c	-10.18	-12.81
SFE		
1a	-2.07	-3.24
1b	-12.71	-10.39
1c	-20.33	-19.47

The DFE profiles for BTA in solvent are displayed in Figure 2.13 and the values are given in Table 2.5. While the self assembly of **1a** appears not to be feasible in the solvent, those of **1b** and **1c** are, signifying the importance of the additional stabilization offered by the alkyl groups to the dimer.

Solvation free energy (SFE)

SFE quantifies the stability offered by the solvent to a BTA molecule with respect to its state in gas phase. SFE profiles are shown in Figure 2.14 and the values are given in Table 2.5. The change in the FE as the molecule enters the solvent is gradual and converges when it is completely solvated. The range over which the FE varies increases with molecular size. While BTA molecules with longer alkyl groups tend to enter the solvent end-on, few solvent molecules too were seen to rise out of the planar liquid-vapor interface to interact with such alkyl groups of BTA. These events increase the range over which SFE varies. All BTA molecules are stabilized in *n*-nonane compared to gas phase. SFE increases with increase in the alkyl group length due to the increase in van der Waals interactions between the alkyl tails and nonane molecules.

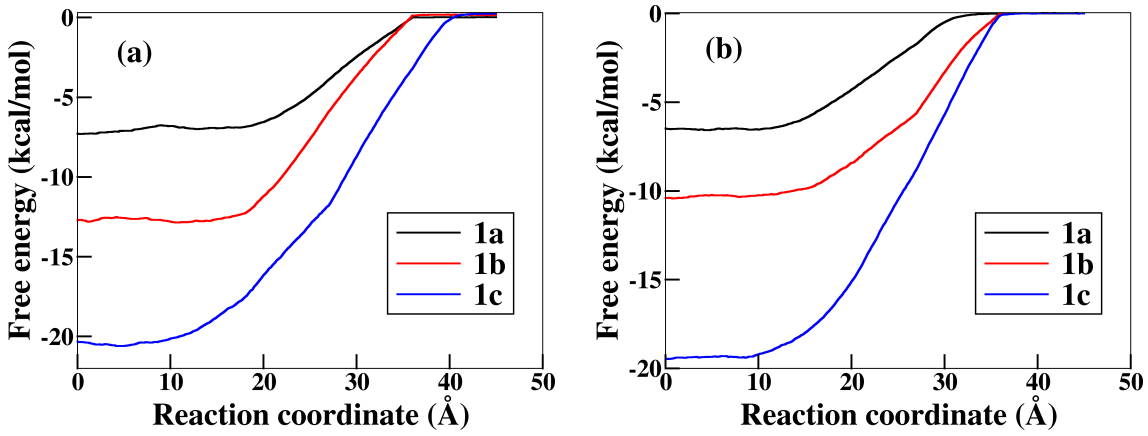

Figure 2.14: Solvation free energy profiles of BTA from vacuum (large distances) to bulk *n*-nonane at 298.15 K studied using the (a) DREIDING-N (b) DREIDING-C force fields.

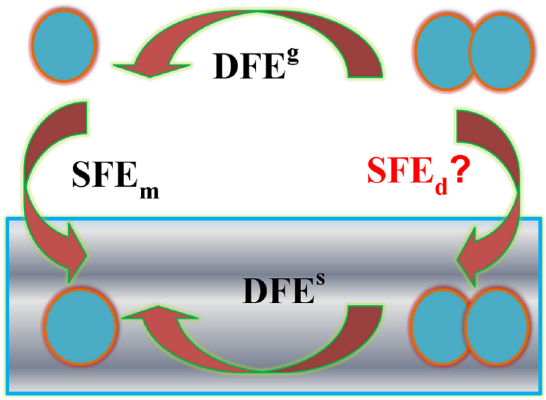

Figure 2.15: Schematic to determine the solvation free energy of a dimer from vacuum to bulk nonane employing the Born-Haber cycle.

Stability of the dimer in bulk solvent with respect to vacuum

Thus far, we have obtained the dimerization free energies (in gas phase and in solvent) and the solvation free energy of various BTA molecules. From these data, the SFE of a dimer (SFE_d) present in bulk *n*-nonane with respect to its existence in vacuum can be calculated using the Born-Haber cycle as represented in the schematic Figure 2.15. From the above three FE calculations, we have access to three pathways and the remaining pathway is rather ease to evaluate. SFE of dimer from both DREIDING-N and DREIDING-C are given in Table 2.6. As the dimer state of **1a** is

Table 2.6: Solvation free energy of BTA dimer from vacuum to bulk *n*-nonane at 298.15 K.

SFE_d (kcal/mol)	DREIDING-N	DREIDING-C
1b	-18.12	-13.61
1c	-31.95	-30.85

not well defined in solution, we did not attempt to calculate its SFE_d.

$$F_d^g - 2F_m^g = DFE^g \tag{2.3}$$

$$F_d^s - 2F_m^s = DFE^s \tag{2.4}$$

$$F_m^s - F_m^g = SFE_m \tag{2.5}$$

In the above expressions, subscripts represent monomer (m) and dimer (d) states while superscripts represent gas (g) and solution (s) phases. Combining the above yields,

$$F_d^s - F_d^g = SFE_d = DFE^s - DFE^g + 2SFE_m \tag{2.6}$$

2.3.8 Cooperativity examined through free energy

As discussed above, the self-assembly of BTA molecules proceeds via a cooperative mechanism. The strength with which each molecule binds to an existing stack increases with oligomer size; relative to a monomer, a molecule present in a dimer has a lower FE than one which is part of a larger oligomer, say a decamer. This aspect has earlier been probed by us and others using quantum chemical methods in gas phase at zero Kelvin temperature [9, 10, 38, 39]. In the present chapter, the same was studied using force fields (see Figure 2.7). Herein, we present a demonstration of the cooperative nature of self-assembly of BTA in solution, at ambient conditions. ABF calculations were used to calculate the FE profiles for the removal of one BTA molecule

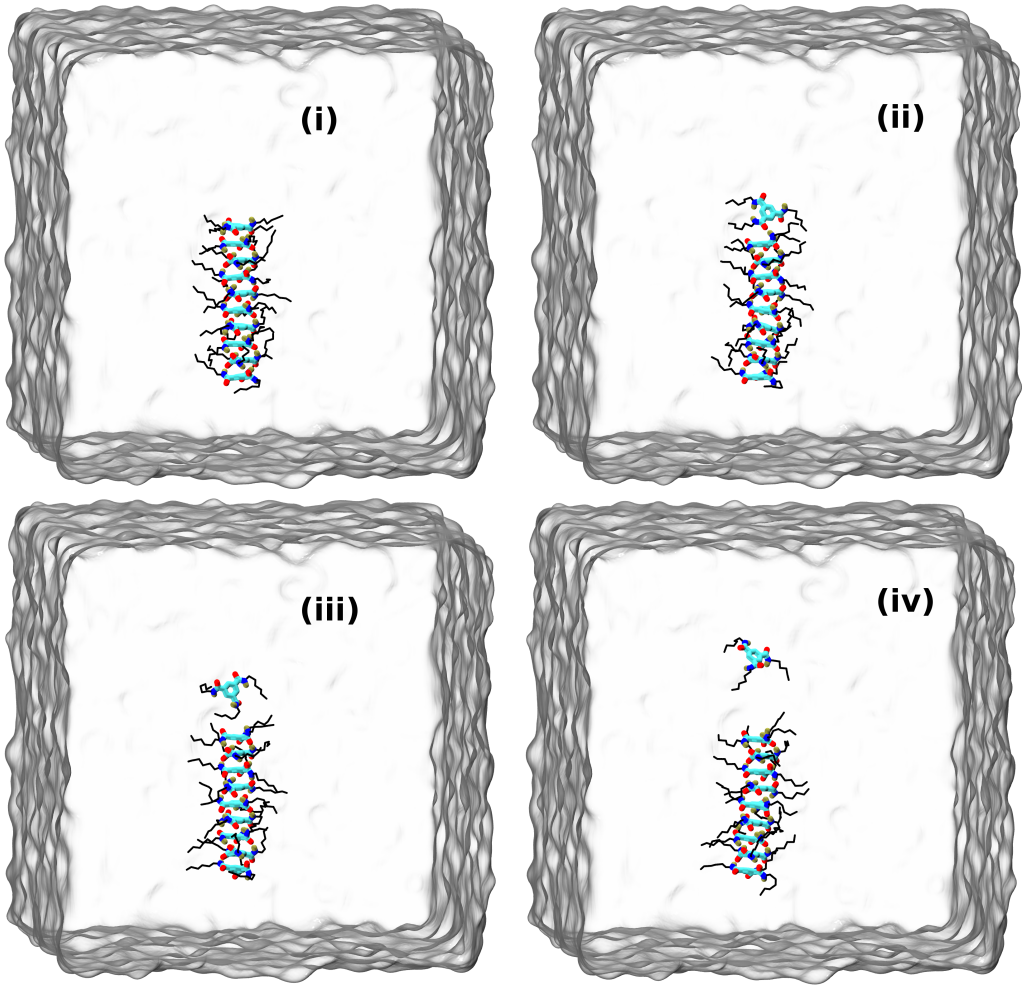

Figure 2.16: Representative snapshots of configurations at different reaction coordinate values illustrating the removal of a molecule from an oligomer.

from three oligomers of **1c** - dimer, tetramer, decamer. Figure 2.16 demonstrates the process of a removal of a molecule from an oligomer.

The dimer, tetramer and decamer of **1c** BTA were solvated in a pre-equilibrated box containing 500, 750 and 2000 *n*-nonane molecules, respectively. For all the three systems, RC was defined as the distance between the centers of mass of the two BTA molecules which lie on the exterior of the stack (excluding its alkyl tails). Two collective variable (colvar) styles, 'distanceZ' and 'distanceXY', were used in evaluating the FE profiles. DistanceXY is used to restrict the BTA molecule to lie within a cylinder defined coaxially along the stack. The RC, 'distanceZ' is the

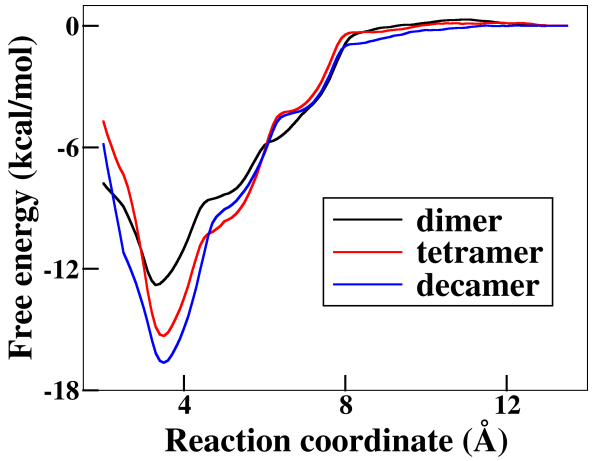

Figure 2.17: Free energy profiles for the release of a molecule from a dimer, tetramer and decamer of **1c** solvated in *n*-nonane at 298.15 K. The reaction coordinate is the distance between the center of mass of the released molecule with respect to the center of mass of the next molecule present in the oligomer.

distance between the BTA molecule in one exterior of the stack and the center of mass of its immediate neighbor that is present in the stack. It was divided into three non-overlapping windows with $N_{samples}$ as 2000 and bin width as 0.1 Å. Each window was run for 25 ns and the the convergence of FE was ascertained. Figure 2.17 clearly exhibits the cooperative behavior of assembly in the FE profiles.

The energy needed to remove a molecule from a decamer of **1c** is calculated to be 16.6 kcal/mol, while the corresponding values from a tetramer and dimer are 15.3 kcal/mol and 12.8 kcal/mol, respectively. In other words, larger the oligomer size, greater is the binding strength of a molecule in solvent, at ambient conditions.

2.4 Conclusions

Atomistic molecular dynamics simulations using two variants of the DREIDING force field [21] have been carried out to establish the nature of cooperative interactions that occur during the self-assembly of BTA in the solvent *n*-nonane under ambient conditions, and as a function of the length of its pendant alkyl groups. Cooperativity in binding energy has so far been reported only for small gas phase oligomers at zero Kelvin, using quantum chemical calculations [9, 10, 38, 39]. Our main finding is that

cooperative self-assembly is observed even using a non-polarizable force field, not only in terms of the gas phase binding energy, but also under experimentally relevant thermodynamic conditions i.e., for the potential energy with increasing oligomer size in the solvent, and the free energy for the release of a BTA molecule from an oligomer.

Importantly, the self-assembly of BTA molecules from an arbitrarily dispersed configuration in *n*-nonane to a columnar stack has been demonstrated using atomistic MD simulations. The formation of a stack is seen to occur on a time scale of tens of nanoseconds. A key structural feature is the asymmetric intermolecular hydrogen bonding, i.e., a given BTA molecule forms two donor and one acceptor type hydrogen bond with a neighbor, which we denoted here as a 2:1 oligomer rather than a 3:0 oligomer, which has three donor and zero acceptor hydrogen bonds. 2:1 oligomers are found to be more stable than their 3:0 counterparts as studied using the DREIDING force field as well as through quantum density functional theory calculations. The stabilization is due to favorable anti-parallel alignment of hydrogen bond dipole moments in the 2:1 state. Our calculations and simulations suggest the possibility of this configuration to be the ground state; however, the energy difference between the 2:1 and 3:0 dimer is in the range of 1 to 2 kcal/mol. An unambiguous identification of the ground state would require further experiments [47] and better quantum methods.

The dimerization free energy profile of BTA as well as its solvation free energy profile, in *n*-nonane have been determined using force field based simulations. The solvated dimer of **1c** (BTA with hexyl tails) is more stable than two of its solvated monomers by 12.8 kcal/mol. The solvation FE for the same compound is calculated to be -19.5 kcal/mol. These values increase with increasing length of the alkyl group.

The FE profiles calculated here will be useful benchmarks for the development of a coarse grained (CG) model for BTA. Such an approach has been accomplished in other systems earlier [48–53]. In the present context, a CG model could be used to study the mechanism of not only columnar self-assembly but also fiber formation, which is

of direct relevance to contemporary experiments. [4, 54] In principle, this approach could be extended to molecules that self-assemble *via* an isodesmic mechanism as well. MD simulations based on chemically specific CG models should be able to delineate microscopic events and energetics of these two contrasting mechanisms that are operative in supramolecular polymerization. These CG models will greatly extend the length and time scales of MD simulations beyond that undertaken here. In the next chapter, we will discuss the strategies employed in developing such coarse-grain potentials.

Bibliography

[1] Matsunaga, Y.; Nakayasu, Y.; Sakai, S.; Yonenaga, M. *Mol. Cryst. Liq. Cryst.* **1986**, *141*, 327–333.

[2] Nakano, Y.; Markvoort, A. J.; Cantekin, S.; Filot, I. A. W.; ten Eikelder, H. M. M.; Meijer, E. W.; Palmans, A. R. A. *J. Am. Chem. Soc.* **2013**, *135*, 16497–16506.

[3] Korevaar, P. A.; Schaefer, C.; de Greef, T. F. A.; Meijer, E. W. *J. Am. Chem. Soc.* **2012**, *134*, 13482–13491.

[4] Stals, P. J. M.; Korevaar, P. A.; Gillissen, M. A. J.; de Greef, T. F. A.; Fitié, C. F. C.; Sijbesma, R. P.; Palmans, A. R. A.; Meijer, E. W. *Angew. Chem. Int. Ed.* **2012**, *51*, 11297–11301.

[5] Cantekin, S.; de Greef, T. F. A.; Palmans, A. R. A. *Chem. Soc. Rev.* **2012**, *41*, 6125–6137.

[6] Cantekin, S.; Nakano, Y.; Everts, J. C.; van der Schoot, P.; Meijer, E. W.; Palmans, A. R. A. *Chem. Commun.* **2012**, *48*, 3803–3805.

[7] Smulders, M. M. J.; Schenning, A. P. H. J.; Meijer, E. W. *J. Am. Chem. Soc.* **2008**, *130*, 606–611.

[8] Brunsveld, L.; Schenning, A. P. H. J.; Broeren, M. A. C.; Janssen, H. M.; Vekemans, J. A. J. M.; Meijer, E. W. *Chem. Lett.* **2000**, *29*, 292–293.

[9] Albuquerque, R. Q.; Timme, A.; Kress, R.; Senker, J.; Schmidt, H.-W. *Chem. Eur. J.* **2013**, *19*, 1647–1657.

[10] Kulkarni, C.; Reddy, S. K.; George, S. J.; Balasubramanian, S. *Chem. Phys. Lett.* **2011**, *515*, 226–230.

[11] Klein, M. L.; Shinoda, W. *Science* **2008**, *321*, 798–800.

[12] Yu, T.; Lee, O.-S.; Schatz, G. C. *J. Phys. Chem. A* **2013**, *117*, 7453–7460.

[13] Yu, T.; Schatz, G. C. *J. Phys. Chem. B* **2013**, *117*, 9004–9013.

[14] Lee, O.-S.; Stupp, S. I.; Schatz, G. C. *J. Am. Chem. Soc.* **2011**, *133*, 3677–3683.

[15] Das, J.; Eun, C.; Perkin, S.; Berkowitz, M. L. *Langmuir* **2011**, *27*, 11737–11741.

[16] Santo, K. P.; Berkowitz, M. L. *J. Phys. Chem. B* **2012**, *116*, 3021–3030.

[17] Jeon, J.; Mills, C. E.; Shell, M. S. *J. Phys. Chem. B* **2013**, *117*, 3935–3943.

[18] Danila, I.; Riobé, F.; Piron, F.; Puigmartí-Luis, J.; Wallis, J. D.; Linares, M.; Ågren, H.; Beljonne, D.; Amabilino, D. B.; Avarvari, N. *J. Am. Chem. Soc.* **2011**, *133*, 8344–8353.

[19] Chami, F.; Wilson, M. R. *J. Am. Chem. Soc.* **2010**, *132*, 7794–7802.

[20] Brocorens, P.; Linares, M.; Guyard-Duhayon, C.; Guillot, R.; Andrioletti, B.; Suhr, D.; Isare, B.; Lazzaroni, R.; Bouteiller, L. *J. Phys. Chem. B* **2013**, *117*, 5379–5386.

[21] Mayo, S. L.; Olafson, B. D.; Goddard, W. A. *J. Phys. Chem.* **1990**, *94*, 8897–8909.

[22] Gasteiger, J.; Marsili, M. *Tetrahedron* **1980**, *36*, 3219 – 3228.

[23] Plimpton, S. *J. Comput. Phys.* **1995**, *117*, 1–19.

[24] Nosé, S. *J. Chem. Phys.* **1984**, *81*, 511–519.

[25] Hoover, W. G. *Phys. Rev. A* **1985**, *31*, 1695–1697.

[26] Hockney, R. W.; Eastwood, J. W. *Computer Simulation Using Particles*; Taylor & Francis, 1989.

[27] Martin, M. G.; Siepmann, J. I. *J. Phys. Chem. B* **1998**, *102*, 2569–2577.

[28] Tuckerman, M.; Berne, B. J.; Martyna, G. J. *J. Chem. Phys.* **1992**, *97*, 1990–2001.

[29] Humphrey, W.; Dalke, A.; Schulten, K. *J. Molec. Graphics* **1996**, *14*, 33–38.

[30] Fiorin, G.; Klein, M.; Hénin, J. *Mol. Phys.* **2013**, *111*, 3345–3362.

[31] Darve, E.; Rodríguez-Gómez, D.; Pohorille, A. *J. Chem. Phys.* **2008**, *128*.

[32] Park, S.; Khalili-Araghi, F.; Tajkhorshid, E.; Schulten, K. *J. Chem. Phys.* **2003**, *119*, 3559–3566.

[33] Nakano, Y.; Hirose, T.; Stals, P. J. M.; Meijer, E. W.; Palmans, A. R. A. *Chem. Sci.* **2012**, *3*, 148–155.

[34] Lightfoot, M. P.; Mair, F. S.; Pritchard, R. G.; Warren, J. E. *Chem. Commun.* **1999**, 1945–1946.

[35] Martínez, L.; Andrade, R.; Birgin, E. G.; Martínez, J. M. *J. Comput. Chem.* **2009**, *30*, 2157–2164.

[36] Fitié, C. F. C.; Roelofs, W. S. C.; Magusin, P. C. M. M.; Wübbenhorst, M.; Kemerink, M.; Sijbesma, R. P. *J. Phys. Chem. B* **2012**, *116*, 3928–3937.

[37] Stals, P. J. M.; Smulders, M. M. J.; Martín-Rapún, R.; Palmans, A. R. A.; Meijer, E. W. *Chem. Eur. J.* **2009**, *15*, 2071–2080.

[38] Smulders, M. M. J.; Buffeteau, T.; Cavagnat, D.; Wolffs, M.; Schenning, A. P. H. J.; Meijer, E. W. *Chirality* **2008**, *20*, 1016–1022.

[39] Filot, I. A. W.; Palmans, A. R. A.; Hilbers, P. A. J.; van Santen, R. A.; Pidko, E. A.; de Greef, T. F. A. *J. Phys. Chem. B* **2010**, *114*, 13667–13674.

[40] Frisch, M. J. et al. Gaussian 09 Revision D.01. Gaussian Inc. Wallingford CT **2009**.

[41] Valiev, M.; Bylaska, E. J.; Govind, N.; Kowalski, K.; Straatsma, T. P.; Dam, H. J. J. V.; Wang, D.; Nieplocha, J.; Apra, E.; Windus, T. L.; de Jong, W. A. *Comput. Phys. Commun.* **2010**, *181*, 1477 – 1489.

[42] Anetai, H.; Wada, Y.; Takeda, T.; Hoshino, N.; Yamamoto, S.; Mitsuishi, M.; Takenobu, T.; Akutagawa, T. *J. Phys. Chem. Lett.* **2015**, *6*, 1813–1818.

[43] Shishido, Y.; Anetai, H.; Takeda, T.; Hoshino, N.; ichiro Noro, S.; Nakamura, T.; Akutagawa, T. *J. Phys. Chem. C* **2014**, *118*, 21204–21214.

[44] Hanabusa, K.; Koto, C.; Kimura, M.; Shirai, H.; Kakehi, A. *Chem. Lett.* **1997**, *26*, 429–430.

[45] Hou, X.; Schober, M.; Chu, Q. *Cryst. Growth Des.* **2012**, *12*, 5159–5163.

[46] Jiménez, C. A.; Belmar, J. B.; Ortíz, L.; Hidalgo, P.; Fabelo, O.; Pasán, J.; Ruiz-Pérez, C. *Cryst. Growth Des.* **2009**, *9*, 4987–4989.

[47] Wegner, M.; Dudenko, D.; Sebastiani, D.; Palmans, A. R. A.; de Greef, T. F. A.; Graf, R.; Spiess, H. W. *Chem. Sci.* **2011**, *2*, 2040–2049.

[48] Bhargava, B. L.; Devane, R.; Klein, M. L.; Balasubramanian, S. *Soft Matter* **2007**, *3*, 1395–1400.

[49] DeVane, R.; Jusufi, A.; Shinoda, W.; Chiu, C.-c.; Nielsen, S. O.; Moore, P. B.; Klein, M. L. *J. Phys. Chem. B* **2010**, *114*, 16364–16372.

[50] DeVane, R.; Klein, M. L.; Chiu, C.-c.; Nielsen, S. O.; Shinoda, W.; Moore, P. B. *J. Phys. Chem. B* **2010**, *114*, 6386–6393.

[51] Li, Z.; Wang, P.; Yan, Y.; Wang, R.; Zhang, J.; Dai, C.; Hu, S. *J. Phys. Chem. Lett.* **2013**, *4*, 3962–3966.

[52] He, J.; Huang, X.; Li, Y.-C.; Liu, Y.; Babu, T.; Aronova, M. A.; Wang, S.; Lu, Z.; Chen, X.; Nie, Z. *J. Am. Chem. Soc.* **2013**, *135*, 7974–7984.

[53] Schor, M.; Ensing, B.; Bolhuis, P. G. *Faraday Discuss.* **2010**, *144*, 127–141.

[54] Singer, J. C.; Giesa, R.; Schmidt, H.-W. *Soft Matter* **2012**, *8*, 9972–9976.

Chapter 3

Supramolecular Polymerization: A Coarse Grained Molecular Dynamics Study

3.1 Introduction

Atomistic simulations of benzene-1,3,5-tricarboxmide (BTA) predicted the self-assembly of molecules in *n*-nonane solution, as described in the previous chapter. However, the large number of degrees of freedom associated an atomistic representation limits the system size and simulation time-scales. Coarse-grain (CG) representation of molecules can redress some of the limitations. Many questions on the mechanism of self-assembly can be answered if models with fewer degrees of freedom are constructed. They could permit the study of mechanism and thermodynamics of self-assembly from a microscopic perspective.

The main aim of the present work is to develop a chemically specific coarse-grain (CG) model for BTA and employ the same to probe the mechanism of its self-assembly in a non-polar solvent. Coarse-graining is a powerful tool which can be employed to access length and time scales that exist between atomistic and mesoscale simulations [1]. It is possible to build coarse grain models which reduce the number of degrees of freedom drastically, yet retain chemical specificity [2–5]. Furthermore, due to the softness of the interactions between CG beads, a larger time step can be used to integrate the equations of motion. Self-assembled structures in various domains have been explored through CG models [6–8]. Following the approach of many researchers in the development of CG models [9–12], the dimerization (DFE) and solvation (SFE) free energy profiles for BTA as determined from AA MD simulations in the previous chapter, were used as benchmark in developing the CG potentials here.

The mapping scheme and the systematic procedure adopted in developing two CG models will be presented in the next section. The self-assembly of BTA molecules in *n*-nonane solution is demonstrated later. Furthermore, free energy (FE) calculations are employed to explore the phenomenon underlying monomer exchange within the sergeants-and-soldiers principle [13]. Using free energy calculations, we observe that the self-assembly behavior can be characterised as downhill cooperative and the critical nucleus is diagnosed to be a trimer.

3.2 Methodology & Simulation Details

3.2.1 Mapping scheme

In the CG model, a set of atoms were grouped together to be represented by a single entity called 'bead'. The mass and position of the bead were taken to be the sum of the masses of atoms and the center of mass of atoms constituting it, respectively. The benzene core of BTA was mapped onto three BZ beads and each amide was represented by a NCO bead. The mapping of alkyl tails and solvent *n*-nonane were adopted from Shinoda *et al.* [9]. Figure 3.1 describes the mapping

scheme. Charge on the beads was evaluated as described below. Firstly, all-atom

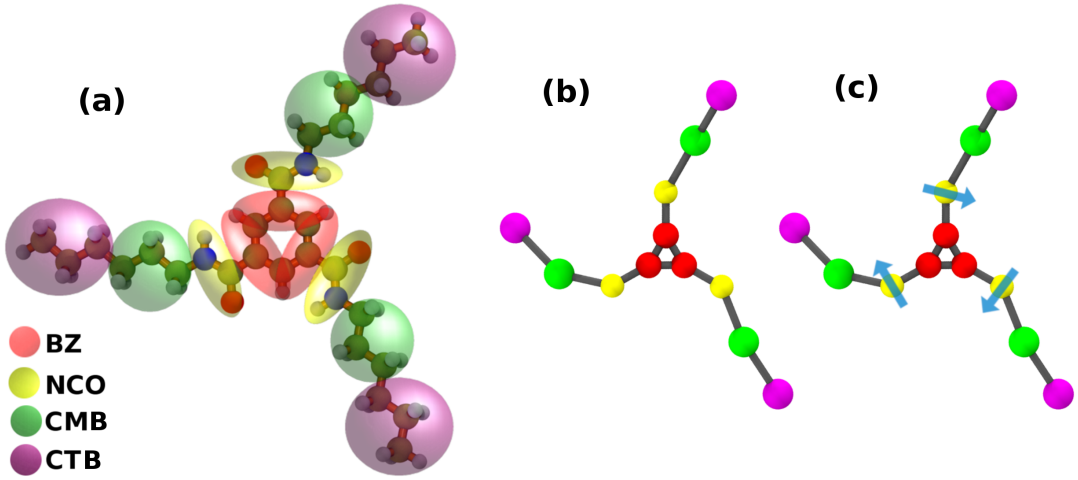

Figure 3.1: (a) Schematic representation of CG mapping on atomistic representation. CG representation of a monomer in (b) Model A and (c) Model B. Blue arrow represents point dipole on the NCO bead.

BTA charges were evaluated using the Gasteiger [14] method, imposing the criterion of a chargeless alkyl tail, so that a CG model which can be deployed for BTA systems with any alkyl chain length can be developed. The charge on the CG bead is taken to be the sum of charge on all the atoms, onto which it is mapped. Thus, the charge of the BZ bead is 0.06182 e and that of the NCO bead is -0.06182 e, where e is the electron charge. We call this model as Model A. Through this approach, a BTA molecule with three hexyl tails consisting of 78 atoms can be represented by just 12 beads. A coarse grained representation of BTA has 4 atom types. With this mapping scheme, and with the bead-bead interaction parameters determined through benchmarks against AA simulations, the model was able to exhibit self-assembly (*vide infra*); however, a crucial feature of oligomers modelled within the atomistic approach is the development of a macrodipole along the stacking direction – one which is absent in the CG model developed above. Thus, it is crucial that a CG model be developed which possesses this feature. We call such a model as Model B.

$$q_{BZ} = q_{C_1} + \frac{1}{2}\left(q_{C_2} + q_{H_2} + q_{C_3} + q_{H3}\right)$$
$$q_{NCO} = q_{C_4} + q_N + q_O + q_{H_1} \tag{3.1}$$

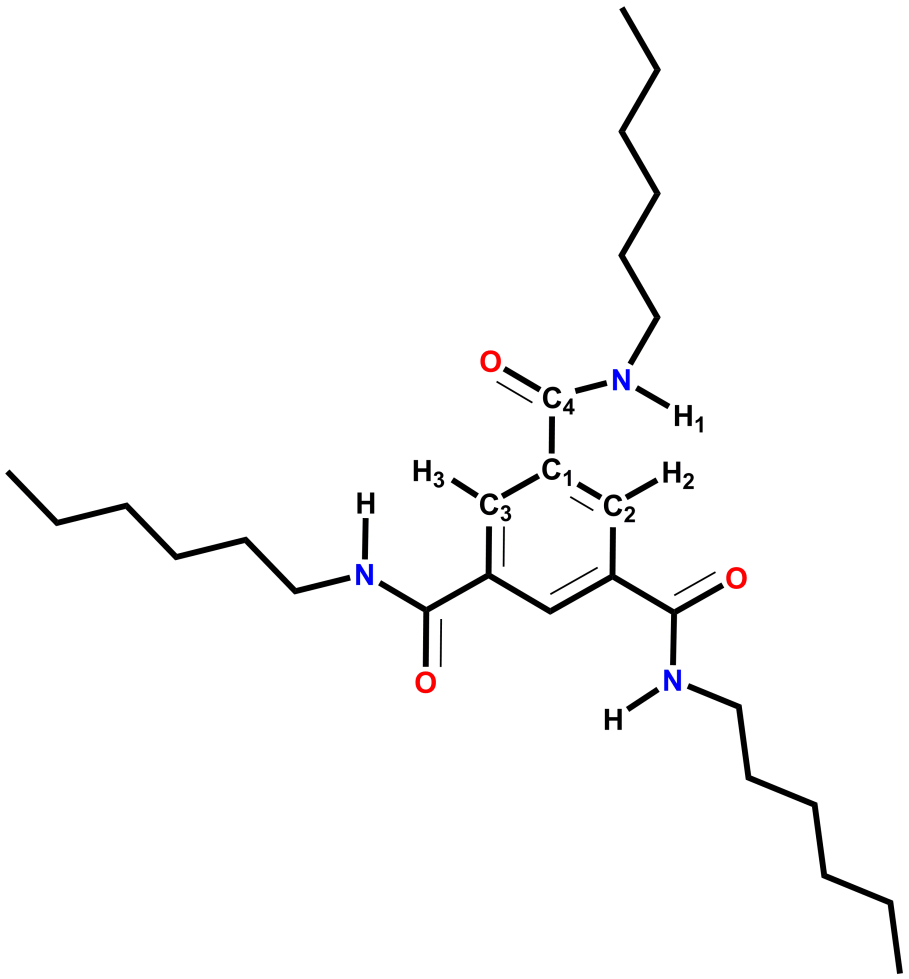

Figure 3.2: Structure of an all-atom BTA monomer.

Model B

In a single molecule of BTA in gas phase, the C=O and N-H bond vectors present in each branch are coplanar, and thus the molecule possesses zero net dipole

moment. Upon oligomerization, hydrogen bonds are formed between amide groups of neighboring molecules. Thus a dipole moment is generated for each hydrogen bond which arises due to the fact that the N-H and C=O groups of a molecule are oriented normal to the benzene plane in either direction (see Chapter 2). The dipole moment of every amide group adds up along the stacking direction, to result in a macrodipole for the stack. Note that there are three amide groups per molecule and it has shown in the previous chapter that the 2:1 configuration, one in which the dipole vectors of only two amide groups are oriented parallel to each other is more stable than the 3:0 configuration. Model-A described earlier lacks this dipole moment. In order to impart a dipole moment to the NCO bead, we have borrowed the idea of tagging a point dipole over an atom from the Stockmayer fluid model [15, 16] which has been effectively used in modelling liquid crystals. An intrinsic point dipole with moment 1.82 D was introduced to lie on each NCO bead (see Figure 3.1). Orsi [17, 18] has developed CG models for water and lipids using a similar approach. In Model B, the non-bonded interactions include van der Waals (E_{LJ}), charge-charge (E_{qq}), dipole-point charge (E_{qp}) and dipole-dipole (E_{pp}).

3.2.2 Simulation details

The intramolecular potential terms included bond and angle energy functions. Beads separated by more than two bonds interacted via a non-bonded potential. All beads were treated as point particles, except the NCO beads in Model-B which were treated as spherical. In addition to the charge, the NCO bead also possesses a point dipole vector (in Model-B) whose magnitude was chosen so as to give a significant macrodipole (*vide infra*) along the stacking direction. All the point particles were coupled to a Nosé-Hoover thermostat [19, 20]. For spherical particles, both the center of mass and dipole rotational degrees of freedom were coupled to a Langevin thermostat [21]. All the CGMD simulations were performed using LAMMPS [22]. A real space cutoff of 15 Å was used for the non-bonded interactions. Long range

Coulombic interactions were treated using particle-particle particle-mesh (PPPM) solver with an accuracy of 1E-5. A time step of 4.0 fs was used to integrate the equation of motions. Three-dimensional periodic boundary conditions were applied. Free energy (FE) calculations were performed using the collective variables module [23] integrated with LAMMPS. For both models, 9-6 type Lennard-Jones potential was employed for the non-bonded interactions. VMD [24] and JMOL [25] were used for visualizations. The non-bonded interactions are as follows:

$$
\begin{aligned}
E_{nb} &= E_{LJ} + E_{qq} + E_{qp} + E_{pp} \\
where, E_{LJ} &= \frac{27}{4}\epsilon\left[\left(\frac{\sigma}{r}\right)^9 - \left(\frac{\sigma}{r}\right)^6\right] \\
E_{qq} &= \frac{q_i q_j}{(4\pi\epsilon_o r_{ij})} \\
E_{qp} &= \frac{q}{r^3}(\vec{p}.\vec{r}) \\
E_{pp} &= \frac{1}{r^3}(\vec{p_i}.\vec{p_j}) - \frac{3}{r^5}(\vec{p_i}.\vec{r})(\vec{p_j}.\vec{r})
\end{aligned}
\tag{3.2}
$$

Here, q and $\vec{p}$ represent charge and dipole on the bead respectively.

Force field parameters

The potential parameters for the two CG models are provided in Table 3.1 and Table 3.2.

Table 3.1: Intramolecular potential parameters are the same in both the CG models. The form of the intramolecular potential is the same as that in Ref. [9].

Bond type	force constant (kcal/mol/Å^2)	r_o(Å)
BZ-BZ	363.0	1.840
BZ-NCO	197.0	2.239
Angle type	force constant (kcal/mol/rad^2)	$\theta_o(^o)$
BZ-BZ-BZ	220.0	60.0
BZ-BZ-NCO	72.0	154.85

Table 3.2: Non-bonded potential parameters of the CG models. [a]cutoff= 5 Å. All other pair interactions have a cutoff of 12 Å.

Type	Model-A		Model-B	
	ϵ (kcal/mol)	σ (Å)	ϵ (kcal/mol)	σ (Å)
BZ-BZ	1.2	3.12	0.99	3.16
BZ-NCO	0.45	4.03	0.59	3.85
NCO-NCO	0.49	3.98	0.48	4.05
NCO-NCO[a]	2.2	4.03	1.6	4.12
BZ-CMB	0.25	5.5	0.25	5.5
BZ-CTB	0.3	5.8	0.3	5.8
NCO-CMB	0.35	5.2	0.35	5.2
NCO-CTB	0.38	5.4	0.38	5.4
BZ-CM	0.4	4.0	0.4	4.0
BZ-CT	0.35	4.15	0.35	4.15
NCO-CM	0.35	4.25	0.35	4.25
NCO-CT	0.30	4.40	0.30	4.40

3.3 Parametrization of CG potentials

3.3.1 Bonded parameters

As mentioned earlier, beads separated by one and two bonds interacted *via* bond and angle potentials respectively. In order to obtain these potentials, an AA simulation of one BTA molecule in gas phase was carried out at 298.15 K. From this trajectory, the positions of CG beads were identified as the center of mass of the corresponding atom group onto which they are mapped. Bond distance and angle distributions from this trajectory were used as the reference for the development of intramolecular CG potentials. Initial guess for these intramolecular terms were obtained by a Boltzmann inversion of the bond and angle distributions (between bead centers) obtained from the reference AA MD simulations. These were refined multiple times until the distributions of bead-bead distances and angles obtained from the CGMD simulations of a monomer matched those from the AA MD simulations.

Intramolecular bond and angle distributions for beads associated with the alkyl tails can be bimodal due to their conformational flexibility. In our parametrization,

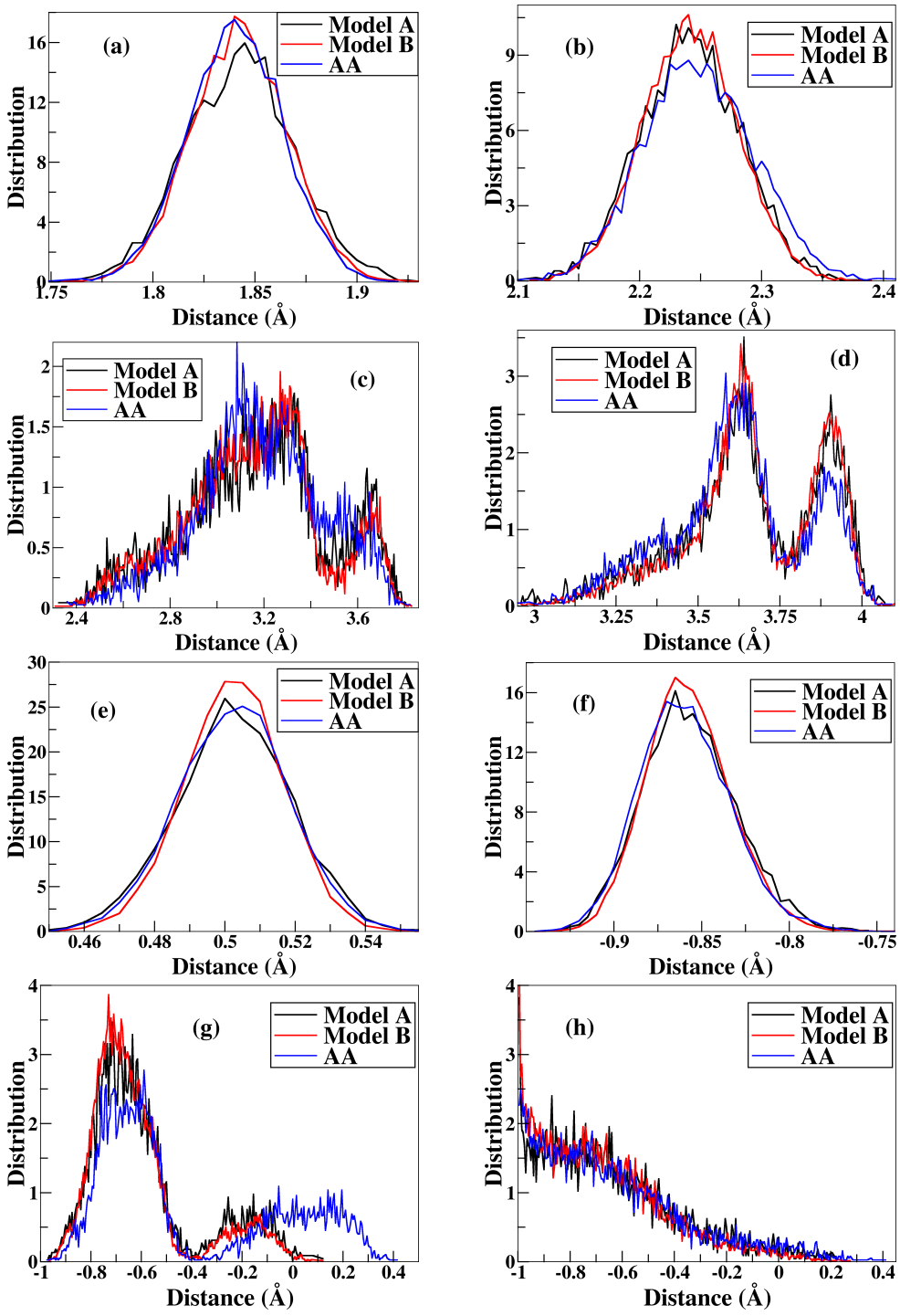

Figure 3.3: Comparison of bond and angle distributions from AA and CG simulations of one BTA in the gas phase carried out at 298.15 K. (a) BZ-BZ (b) BZ-NCO (c) NCO-CMB (d) CMB-CTB (e) BZ-BZ-BZ (f) BZ-BZ-NCO (g) BZ-NCO-CMB (h) NCO-CMB-CTB

bond and angle potentials were fitted to a harmonic form where such distributions were unimodal, while bimodal distributions were reproduced using tabulated potentials as

shown in Figure 3.3.

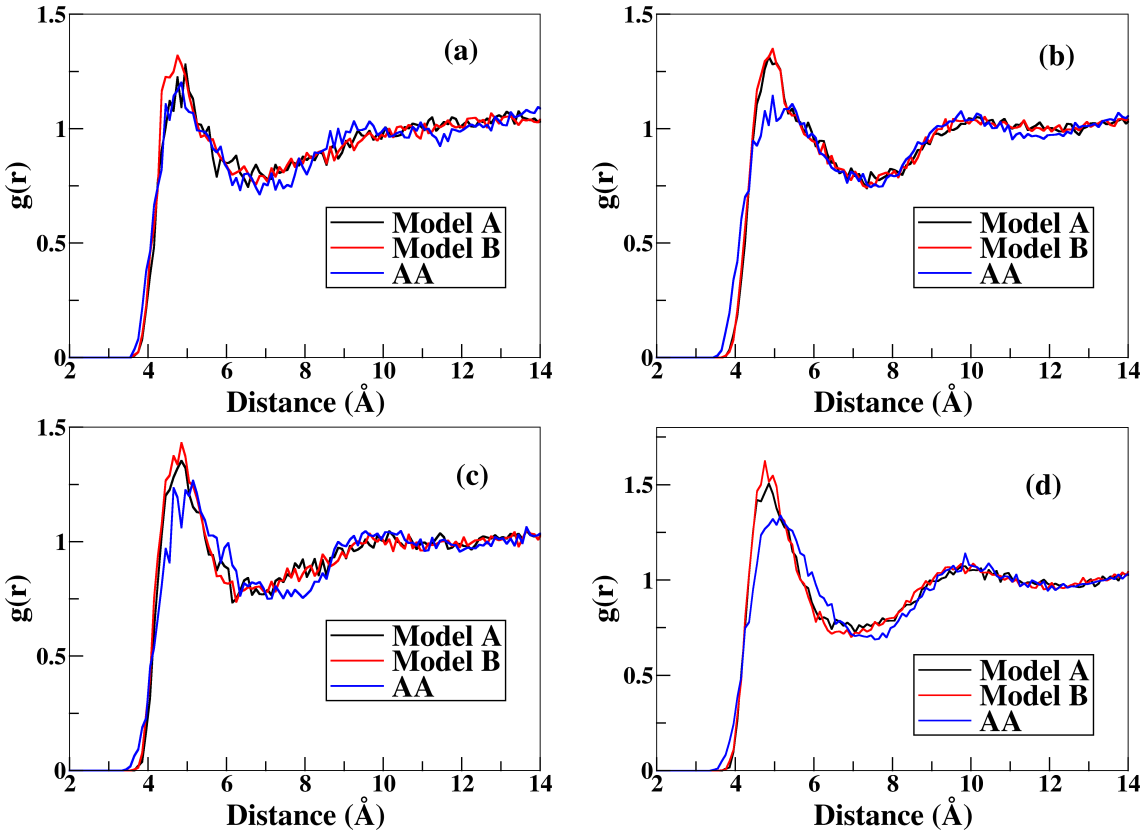

Figure 3.4: Radial distributions functions between the CG beads of BTA and nonane. (a) BZ-CM (b) BZ-CT (c) NCO-CM (d) NCO-CT

3.3.2 Non-bonded parameters

The parameterization of non-bonded potentials was a more challenging task. Three sets of interactions – BTA-BTA, BTA-nonane, and nonane-nonane were required. Nonane-nonane parameters were adopted from Shinoda *et al.* [9]. Next, we were interested in obtaining the cross interactions between BTA and solvent beads. Towards this purpose, MD simulation of one AA BTA molecule soaked in a box of AA *n*-nonane was carried out at 298.15 K in the canonical (NVT) ensemble. The radial distribution functions (RDF) between the bead positions of BTA and nonane were obtained. The potential of mean force (PMF) between the beads was obtained as -k_BT ln(g(r)). The PMF formed the initial guess for the interaction potentials. Analogous CGMD

simulations were performed with this potential to compare the g(r) against those obtained from the AA simulation. The non-bonded interaction parameters between BTA and nonane beads were refined iteratively until satisfactory agreement was obtained, as demonstrated in Figure 3.4. Parameters of Shinoda *et al.* [9] were found to be effective in describing the interactions between the alkyl tails of BTA and nonane and thus were employed as-is.

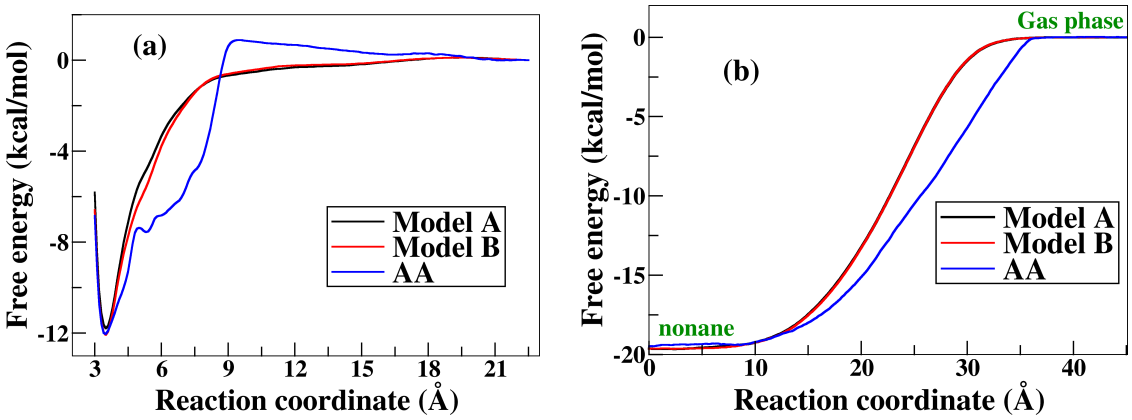

Figure 3.5: Comparison of the (a) dimerization and (b) solvation free energy profiles. AA: All-atom; Models A and B are coarse grained representations.

In order to derive BTA-BTA interaction parameters, the procedure of matching RDF profiles in either its liquid state or in the solution state can lead to representation which possesses the capability of forming a hydrogen bond with the amide group of a neighboring molecule. The strength of one such hydrogen bond in a BTA dimer is around 5 kcal/mol, as described in the previous chapter. The AA model of BTA included a specific hydrogen bond potential term which was not only short ranged (typically less than 5 Å) but also possessed an orientation dependence; this short-range interaction needs to be incorporated in the CG model as well. In order to mimic such short range hydrogen bond interactions, the NCO-NCO potential was split into two Lennard-Jones (9-6, see Eq. 3.2) terms, one with the default cutoff (15 Å) having smaller 'ϵ' and a shorter-ranged one (5 Å cutoff) with a higher 'ϵ' value. Adaptive Biasing Force (ABF) [26] simulations were repeatedly performed by refining the

parameters of these nonbonded interactions until the DFE and SFE profiles obtained from the CGMD simulations matched with the corresponding AA ones. The same are shown in Figure 3.5 and the values are provided in Table 3.3.

3.3.3 Stack stability & intermolecular distance

CGMD simulations of a pre-formed BTA oligomer of size 20 were carried out in *n*-nonane solution at 298.15 K using both the models. All $\pi - \pi$ contacts were found to be intact throughout the simulation duration of 10 ns; the stack structure too was found to be preserved. Thus, it can be inferred that the CG parameters developed here represent the system well. The distribution of intermolecular distances measured between benzene ring centres of neighboring molecules *via* the AA and CG models are shown in Figure 3.6. The mean values obtained from the CG distributions are in good agreement with those from AA and are summarized in Table 3.3.

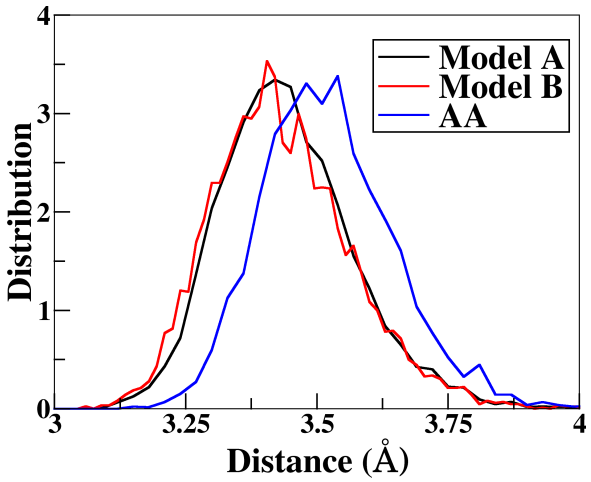

Figure 3.6: Distributions of intermolecular distances obtained from simulations of the pre-formed oligomer of size 20 in solvent.

3.3.4 Dipole orientations

In the previous chapter, we have shown that the asymmetric stacking structure (2:1 hydrogen bonded) is more stable than a symmetric one (3:0 hydrogen bonded). Representative dimers of these two configurations are shown in Figure 3.7a. A symmetric dimer, in which all the three hydrogen bond dipoles are parallel to each

Table 3.3: Dimerization (DFE) and solvation (SFE) free energies (in kcal/mol) for AA and CG models. Last column is the intermolecular distance (in Å).

	DFE	SFE	π-π distance
Model A	-11.79	-19.65	3.44
Model B	-12.07	-19.64	3.43
All-Atom	-12.03	-19.47	3.52

other results in three 'ferromagnetic-like' interactions whereas in an asymmetric dimer, two h-bond dipoles are parallel to each other while the third is antiparallel to both, resulting in two 'antiferromagnetic-like' and one 'ferromagnetic-like' interactions. A preference for the 2:1 configuration was seen in the gas phase quantum chemical calculations as well as empirical force field based AA MD simulations. We were thus curious to see if the CG model (Model-B) will reproduce this feature. A CGMD simulation of a pre-formed decamer (initiated in 3:0 fashion) soaked in *n*-nonane was carried out at 298.15 K. Rotational degrees of freedom of dipoles were coupled to a Langevin thermostat as described before and were free to rotate. The dipoles were seen to rearrange themselves in an asymmetric (2:1) fashion within 1.5 ns and remained so thereafter for over 20 ns as shown in Figure 3.7b, consistent with results from AA simulations.

3.3.5 Supramolecular aggregation

Having compared the results of the CGMD simulations to those from AA MD, what remains to be verified is the process of self-assembly of BTA in solution, starting from a random initial configuration. Towards this end, an initial configuration of 30 monomers randomly dispersed in *n*-nonane solution was generated using Packmol [27]. MD simulations of the system was carried out at 298.15 K in the NPT ensemble using both the CG models A and B. The formation of smaller oligomers which later grew into larger ones was observed in both the models. Snapshots illustrating the self-assembly are shown in Figure 3.8 and 3.9. In Model-B, due to the presence of an intrinsic point dipole, the oligomer possesses a macrodipole moment along the

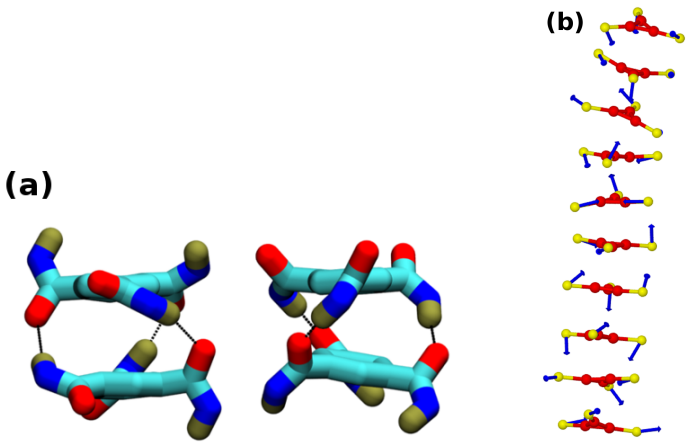

Figure 3.7: (a) Two possible configurations of BTA dimer in its AA representation. Color scheme: carbon-cyan; hydrogen-tan; nitrogen-blue; oxygen-red. (b) Snapshot of a decamer, represented using Model-B at 298.15 K in *n*-nonane which prefers the asymmetric (2:1) configuration of dipole vectors. Thick arrows in blue represent the point dipole on NCO beads. CMB and CTB beads, as well as solvent molecules are not shown for clarity.

stacking direction. Since a macrodipole is an essential feature of BTA based systems, all further analyses presented here have been carried out using Model-B. Based on a simulation of a system containing 10 BTA molecules in a solvent bath of 1000 *n*-nonane molecules, we observe a 400-fold improvement in the wall-clock time needed to generate a trajectory of the same duration (real-time) for the CG model over the AA one.

3.4 Results and Discussion

3.4.1 Self-assembly

Supramolecular polymerization of BTA proceeds spontaneously even at very dilute (μM) concentrations. In the previous section, self-assembly in a non-polar solvent was demonstrated through both the CG models. While the concentration of BTA employed in experiments is in the range of μM, the same cannot be readily realized in simulations (even within a coarse grain approach) due to the computational challenges. A modest attempt is made herein, where we study the self-assembly of BTA at mM concentration. The simulation system contained 250 BTA molecules dispersed in a

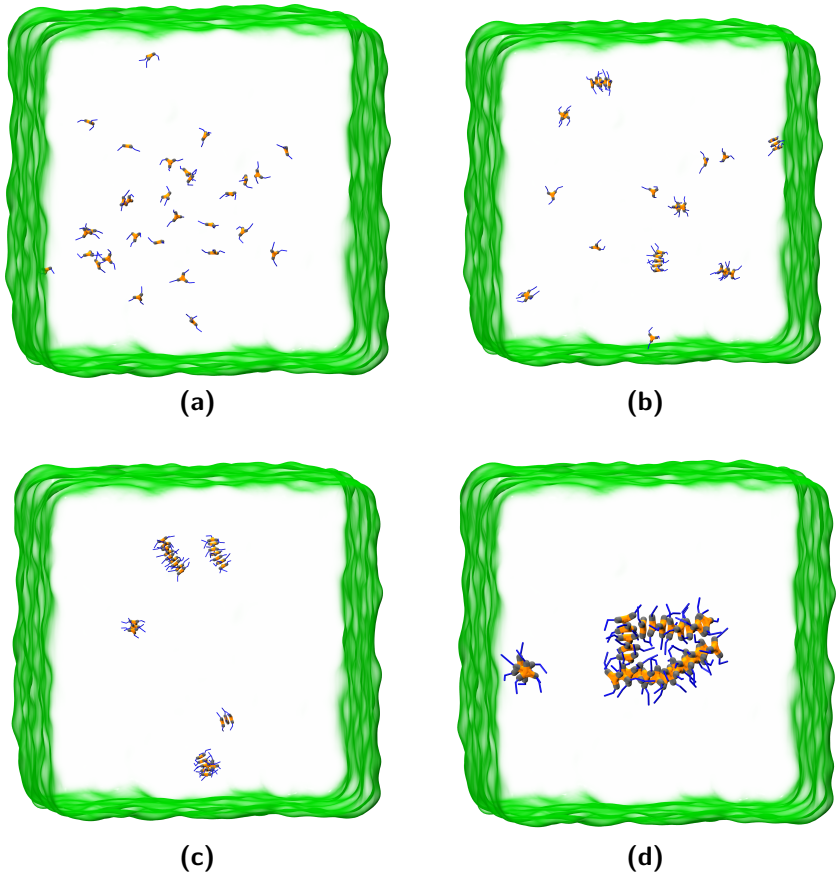

Figure 3.8: Snapshots illustrating the self assembly process of 30 CG BTA molecules dispersed in 20000 *n*-nonane molecules, extracted from MD simulations carried out using **Model A** at a temperature of 298.15 K. Time stamps: (a) 0 ns, (b) 10 ns, (c) 30 ns, and (d) 72 ns. Final snapshot is zoomed in for clarity. Color scheme: BZ-orange; NCO-grey; CMB and CTB - Blue. Nonane molecules are represented using 'QuickSurf' drawing method.

bath of two lakh *n*-nonane molecules, within a cubic box whose edge length is 40.0 nm corresponding to 6.03×10^5 CG beads in all. MD simulations were carried out in the canonical (NVT) ensemble at 298.15 K. BTA molecules were modelled using 'Model-B' as described above. Configurations were saved every 8 ps for post-processing analysis. Snapshots showing the progress of self-assembly as a function of time are exhibited in Figure 3.10. Within few tens of nanoseconds, monomers coalesce to form smaller oligomers and these elongate into longer oligomers over hundreds of nanoseconds. One such oligomer containing fourteen molecules is highlighted in Figure 3.10 for

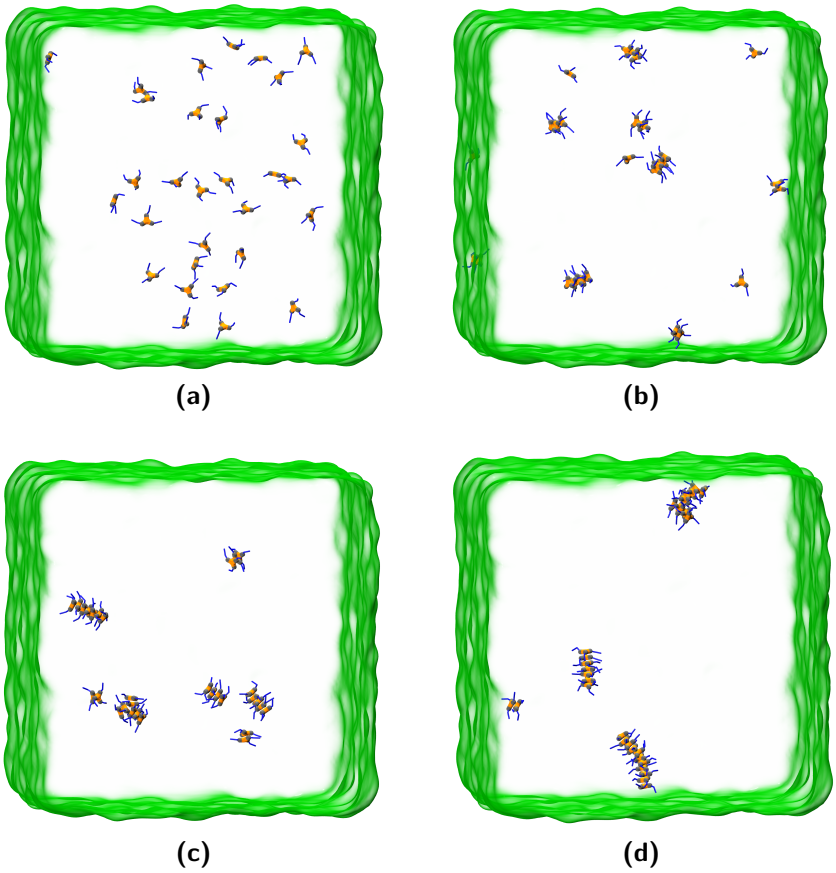

Figure 3.9: Progress of aggregation using **Model B** at various time stamps (a) 0 ns, (b) 10 ns, (c) 30 ns, and (d) 72 ns. Color scheme is same as previous figure. Point dipoles on NCO beads are not shown for clarity.

a clear visualization. The macro-dipole moment of an oligomer was determined as $\sum(q_i \times \vec{r}_i) + \sum \vec{p}_i$, where q_i, $\vec{r}_i$ are the charge and position of bead i respectively while $\vec{p}_i$ is the point dipole of NCO bead. The macro-dipole moment along the stacking direction for this oligomer was found to be 8.22 D. The time evolution of the number of aggregates and their sizes are presented in Figure 3.11 which was obtained through a cluster analysis. This was carried out by considering the BZ beads of each molecule. Two molecules whose BZ beads were within 4 Å were considered to be part of a cluster.

It should be borne in mind that the dynamics in CG representation is typically much faster [28] than in the AA one due to the softer and smoother potentials

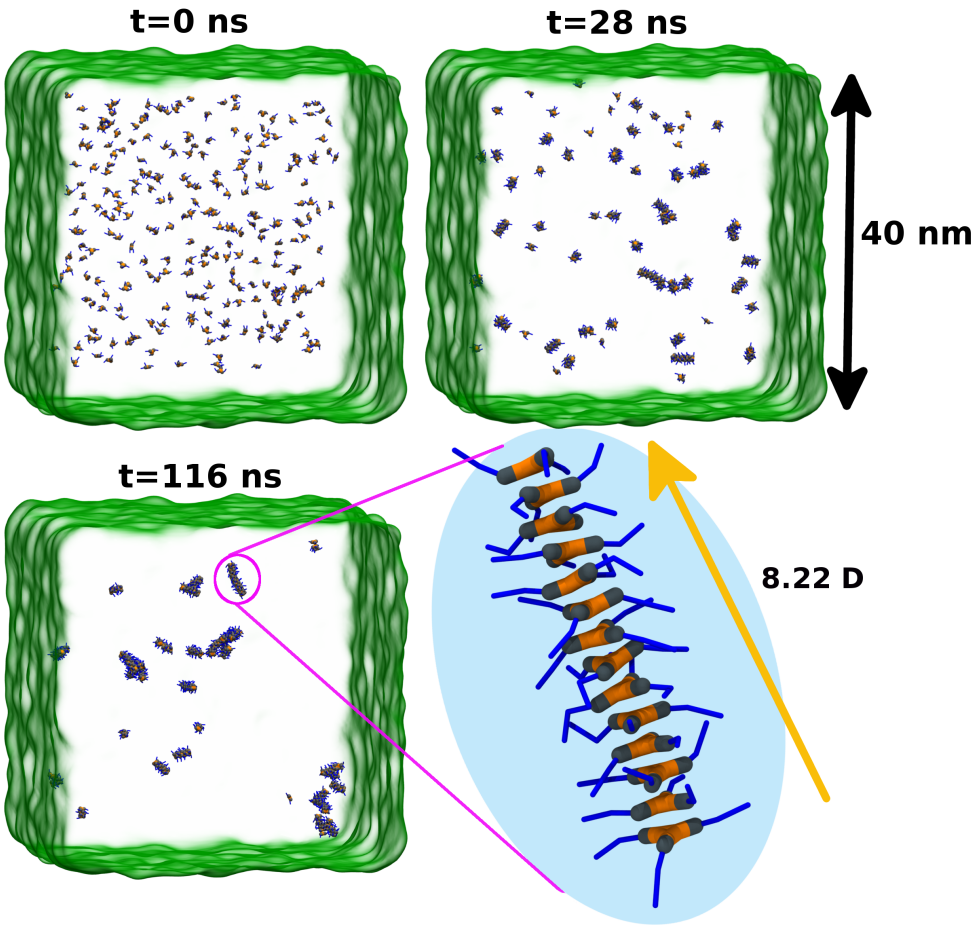

Figure 3.10: Snapshots illustrating the aggregation of 250 CG BTA molecules dispersed in 2 lakh *n*-nonane molecules at 298.15 K, over time. A magnified view of one oligomer with its dipole vector of magnitude 8.22 Debye is also shown. Color scheme is same as previous figure.

employed. Hence, the CG timescales observed here need to be stretched to compare against realistic ones.

3.4.2 Dynamic equilibrium between molecules of different stacks

Self-assembly of disc shaped C_3-symmetric molecules obey the 'Sergeants-and-Soldiers' [13] principle. Oligomers of achiral molecules do not exhibit any specific handedness i.e., an equal proportion of P and M enantiomers exist in solution. Introduction of a small amount of chiral molecules (sergeants) into such a solution

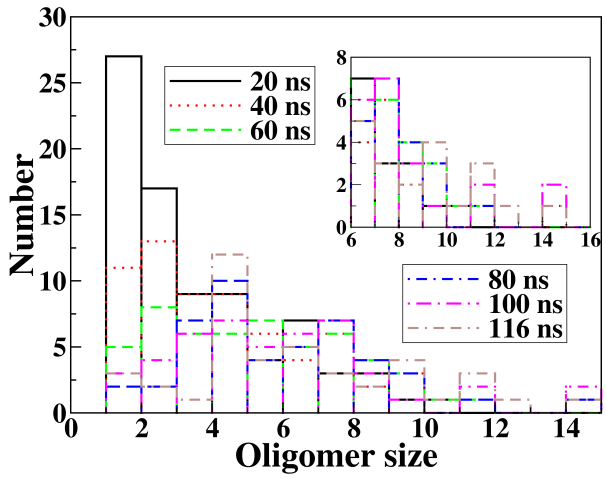

Figure 3.11: Evolution of aggregate sizes as a function of simulation time. Inset: Same data focussing on larger oligomers. BZ beads of two different molecules present within 4 Å of each other were considered to be part of an oligomer.

of achiral (soldiers) molecules induces a specific handedness to the supramolecular polymer. Such a solution exhibits a circular dichroism (CD) signal in accordance with the nature of the added sergent molecules. Recently, Meijer and co-workers [29] showed that a mixture of two separate fibers labelled with different dyes, could not be distinguished after 24 h. This process of mixing proceeds neither through *'polymerization-depolymerization'* nor by *'fragmentation-recombination'* and was accounted for by the dynamic exchange of molecules between the oligomers.

We would like to understand the phenomenon of exchange of monomers using MD simulations and estimate the FE change associated with this process. Towards this aim, a simulation box consisting of a pre-formed oligomer of size 20 soaked in 12,834 *n*-nonane molecules was constructed. Steered Molecular Dynamics (SMD) [30, 31] simulations were carried out in the isothermal-isobaric (NPT) ensemble to determine the FE change for the removal of a molecule from this oligomer into the bulk solution. SMD is a non-equilibrium method in which accumulation of work as a function of the extent of steering can be determined. However, the FE difference is an equilibrium quantity which can be obtained from several non-equilibrium trajectories using the

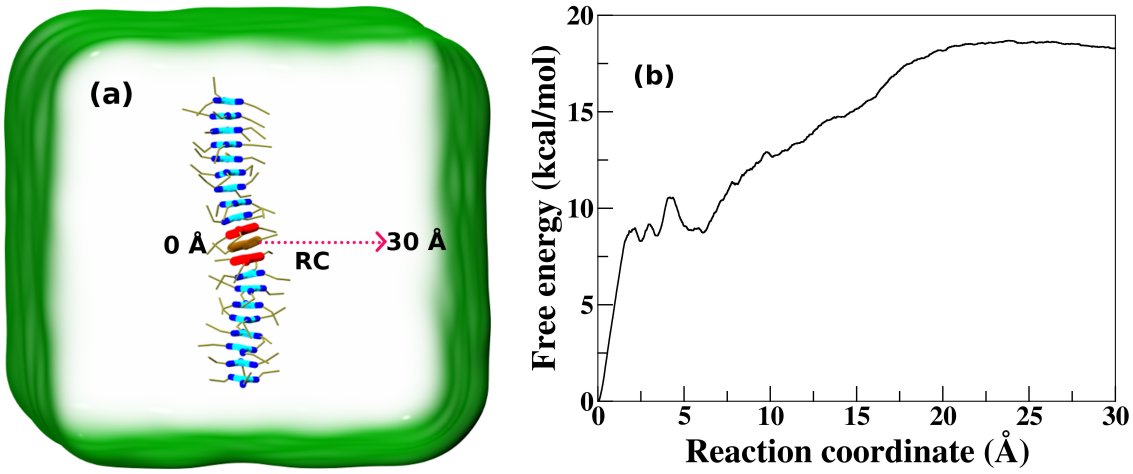

Figure 3.12: (a) Schematic representation of reaction coordinate (RC) for pulling a molecule from the middle of a 20-mer stack into bulk solution. Molecules 10 and 12 are shown in red and molecule 11 is represented in brown. (b) Free energy profile averaged using Jarzynski's equality over 30 SMD work trajectories. Simulations were carried out using Model-B at a temperature of 298.15 K.

Jarzynski equality [32]. In our simulations, the SMD spring constant was chosen to be 100 kcal/mol/Å^2 and SMD calculations were performed in constant velocity mode at various pulling rates. The reaction coordinate (RC) was defined as the distance between the center of BZ beads of molecule 11, and the mean position obtained from BZ beads of molecules 10 and 12 (see Figure 3.12a). 'Distance' style was employed to remove a molecule from the stack. The entire stack, other than molecule 11, was restricted within a parallelepiped so as to preserve its columnar structure during the evolution of the RC. The converged FE profile, shown in Figure 3.12b, was obtained using Jarzynski's equality [32], averaged over 30 SMD profiles. The individual non-equilibrium work profiles from SMD are shown in Figure 3.13. The molecule in the center of the stack is stabilized by 18.2 kcal/mol compared to its monomeric state in bulk solution. When a monomer in bulk solution approaches the core of an oligomer, the FE gradually decreases up to a distance of 4 Å. The profile at shorter distances is rugged and exhibits small barriers. This is due to the adoption of various orientations that the molecule inserting itself into the oligomer takes. The

only possibility for a monomer to incorporate itself within the core of the stack is by keeping its benzene plane parallel to the molecules which are part of the oligomer. Since the barriers are only around 1-2 kcal/mol, this process is indeed accessible to thermal energy at ambient conditions. This observation implies that a molecule in the center of the stack can indeed exchange with the pool of monomers in the bulk solution [13].

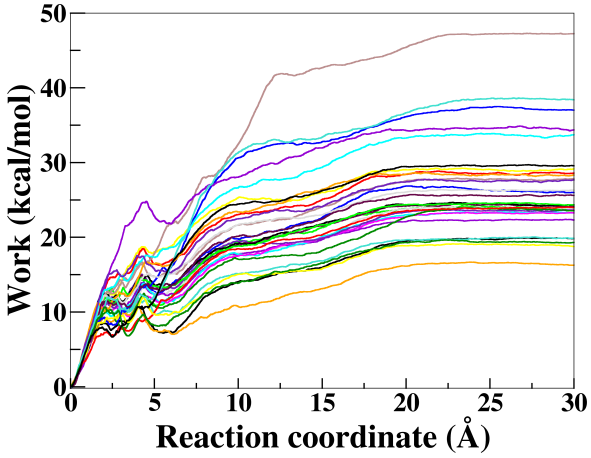

Figure 3.13: Work profiles corresponding to different pulling rates, for dragging a molecule from the core of 20-mer stack into bulk solution at a temperature of 298.15 K. These were obtained as part of the Steered MD (SMD) runs employed to generate free energy profile as shown in 3.12b.

3.4.3 Nature of cooperativity and critical size of the nucleus

BTA monomers present in a high temperature solution self-assemble upon slow cooling *via* the formation of a nucleus. The nucleus formation can be associated either with lowering the free energy (downhill) or an increase (uphill) with respect to monomers [33]. It is challenging to distinguish the two experimentally. For a better understanding of the experiments, analytical models [34, 35] have been developed by assuming the nucleus size to be 2 (i.e., a dimer). Such models form the basis to evaluate thermodynamic properties and determine the self-assembly mechanism. We are thus inquisitive to find out (i) the nature of cooperativity: downhill or uphill and (ii) the size of the nucleus.

From a theoretical point of view, the free energy of formation of an oligomer (from monomers) as a function of its size determines the mechanism of polymerization [33]. In the previous chapter employing an all-atom model, ABF simulations were used to demonstrate cooperativity in the FE for the removal of a molecule from an oligomer. The RC was defined as the distance between the center of mass of BZ beads of two outermost molecules, hydrogen bonded to each other (see Figure 3.14a). In these simulations, RC was divided into bins of 0.1 Å, in each of which the force experienced on it was averaged over 500 steps. Entire RC was divided into two non-overlapping windows spanning the distance from 3 Å to 25 Å. 'Distance' colvar style was employed to determine the FE along the RC. BZ beads of molecule 2 were fixed to define a coaxial cylinder of radius 3 Å using 'distanceXY' along z-axis and molecule 1 was restricted in the cylinder (See Figure 3.14 for definition of molecule indices). Two sets of simulations were carried out by modelling BTA either with Model A or Model B. All the simulations were performed for at least 100 ns to obtain converged FE profiles and the same are displayed in Figure 3.14b,c. The ratio of maximum to minimum samples collected across the RC was ≈ 8. The free energy of binding of a monomer to an oligomer increases gradually from a dimer to a tetramer, beyond which it converges to a value around 16 kcal/mol. Besides the exhibition of self-assembly from dispersed monomers, cooperativity in FE is another important validation for the CG models developed here.

Irrespective of whether a molecule from solution adds to the end of a stack or to its middle, the free energy change should be the same. Thus, the difference in the FE changes reported here for the end-addition (around 16 kcal/mol) and the addition to the centre (around 18 kcal/mol) should be seen as nominal and likely to arise from sampling and methodological differences.

In general, apart from a monomer, a short oligomer too can add to a pre-existing stack on the latter's terminal. We have studied the free energy change involved in this process as a function of the size of the short oligomer, using the ABF method.

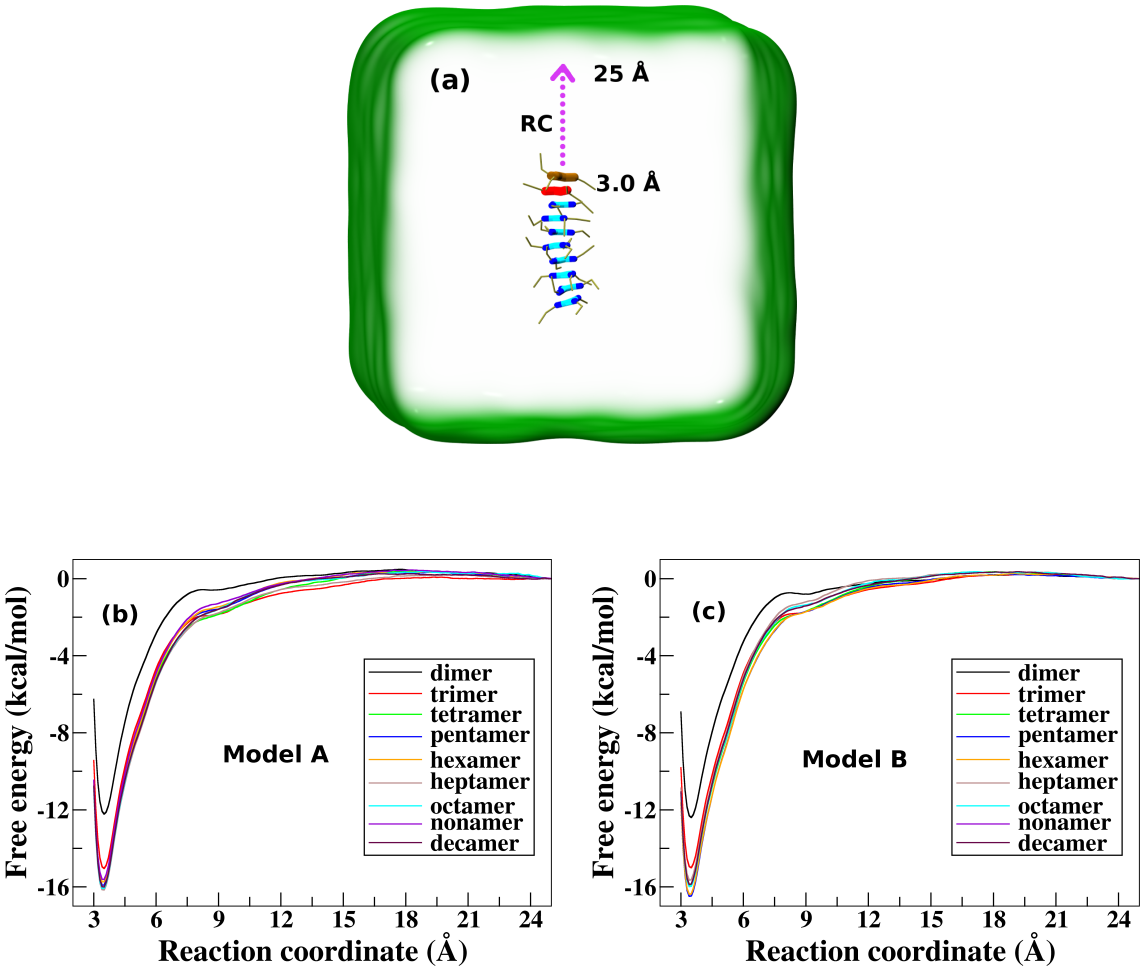

Figure 3.14: (a) Schematic representation of RC for removing a molecule from one end of the stack. RC is the distance between the centers of mass of the molecule being removed and the one that is closest to it present in the oligomer. Molecule 1 is shown in brown and molecule 2 is represented in red. (b), (c) Free energy profiles associated with the process of removing a molecule from oligomers of various sizes, each solvated in *n*-nonane solution at 298.15 K using Model A and Model B respectively.

Once again, the 'DistanceZ' style was employed in determining the change in FE, and RC was defined as the distance between the center of the short oligomer (n=2,3,5,7) and the closest molecule in the stack [36]. BZ beads of the closest molecule were fixed to define a coaxial cylinder along z-axis. Table 3.4 shows the corresponding FE differences. While the monomer joins a stack (19-mer) with a free energy gain of around 16 kcal/mol, a dimer is seen to add to a 18-mer with a FE gain of around 20 kcal/mol. This FE change remains more or less at the same value for larger oligomers

fusing with a stack. The change in FE between a monomer addition and a dimer addition to a pre-existing stack further points to cooperativity in self-assembly.

Table 3.4: Free energy change for the removal of an oligomer from the terminus of a stack into bulk solution at 298.15 K using Model B. The total number of molecules in the stack is 20.

Oligomer	ΔG (kcal/mol)
monomer	15.92
dimer	19.76
trimer	21.50
pentamer	21.44
heptamer	21.67

Type of cooperativity

In the following, G_n denotes the free energy of a n-mer in solution. The free energy of formation of a n-mer out of n individual monomers is denoted as ΔG_n. It is challenging to determine this quantity directly, which may involve the effective use of coordination number as a reaction coordinate. However, the results obtained so far can themselves be used to determine ΔG_n. We illustrate this procedure through the free energy of formation of a trimer from three monomers in solution ($\Delta G_3 = G_3 - 3G_1$) in the following manner:

1. Two out of the three dispersed molecules can form a dimer and the free energy change associated with this process is dimerization free energy (DFE) which has been determined earlier ($\Delta G_2 = G_2 - 2G_1$).

2. A third molecule can bind to the dimer and the free energy change for this process can be quantified by the reverse process – that of removing a molecule from a trimer (G_3 - G_2 - G_1), as discussed above.

The FE of a trimer with respect to the three monomers ($\Delta G_3 = G_3 - 3G_1$) can be simply obtained by adding the above two quantities. The FE of formation for oligomers ($\Delta G_n = G_n - nG_1$) of different sizes (n) were determined likewise and are

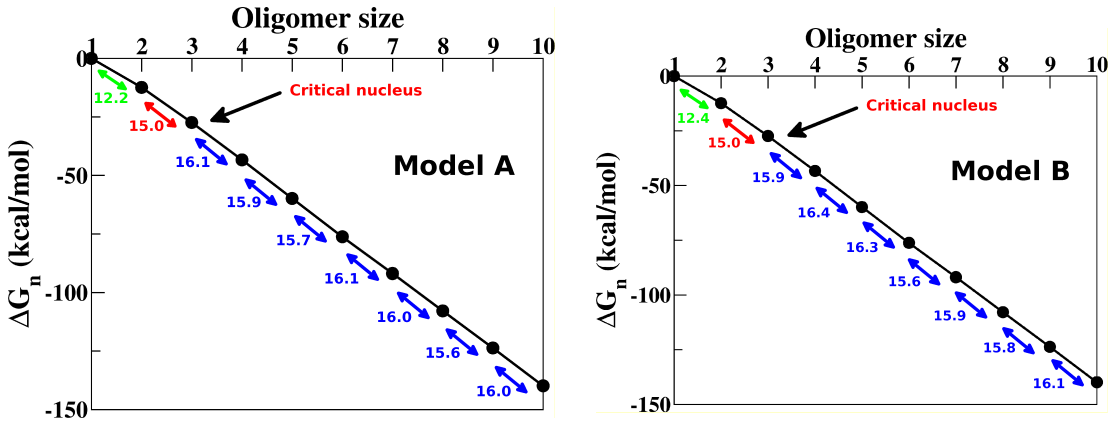

Figure 3.15: Free energy of formation ($\Delta G_n = G_n - nG_1$) for various sizes of oligomers in *n*-nonane solution at 298.15 K. The difference in FE of formation between oligomers differing by one molecule ($\Delta G_n - \Delta G_{n-1}$) are written as text within the figure. The critical size of the nucleus is identified as a trimer.

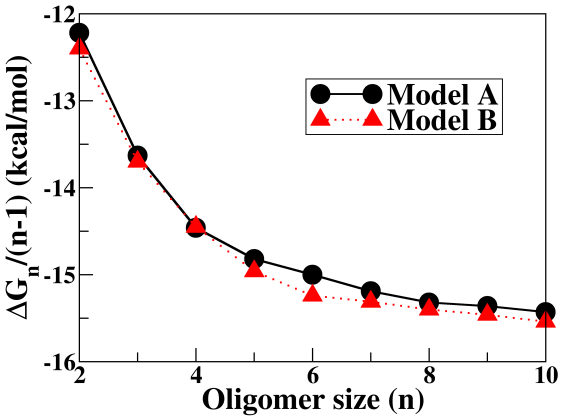

Figure 3.16: Free energy of formation of an oligomer from individual monomers, normalized per contact ($\Delta G_n/(n-1)$). Both models predict a cooperative nature of self-assembly of BTA molecules.

presented in Figure 3.15. The trend is similar to what was delineated for downhill cooperativity in Ref. [33]. Prior to the formation of the nucleus, the change in the formation FE for an oligomer increases but attains a constant value beyond the point of nucleation. During the elongation process, monomers attach to an oligomer with the same binding strength (association constant). Clearly, the trimer appears to be the likely nucleus, beyond which size the change in FE per molecule converges to a value of around 16 kcal/mol. In BTA systems, a n-mer possesses 3(n-1) hydrogen

bonds. Thus, the ratio of the free energy of formation of a n-mer (ΔG_n) to the number of triplets of hydrogen bonds present in the stack provides information on the stabilization of a molecule *via* not only the h-bonds it forms with its neighbors, but also through long range interactions it is involved in. Such a quantity is displayed in Figure 3.16. $\Delta G_n/(n-1)$ increases with oligomer size (n) until saturation, which is a signature of cooperativity in the self-assembly of BTA molecules.

3.5 Conclusions

We have developed two coarse-grained models (Models A and B) for benzene-1,3,5-tricarboxamide which have exhibited a good potential for the study of self-assembly of BTA in an apolar, n-nonane solvent. Intramolecular potential terms in the coarse grain representation have been fitted to either a harmonic form (for unimodal distributions) or to tabulated potentials (for bimodal ones). A short range potential is employed to capture hydrogen bonding interactions. In Model B, an intrinsic point dipole is introduced on one of the coarse grain beads to represent the dipole moment of the intermolecular hydrogen bond. Consequently, a BTA stack acquires a macro-dipole along the stacking direction. Dimerization and solvation FE profiles obtained from AA simulations were reproduced using both the CG models. The stability of asymmetric stacking (2:1) over a symmetric one (3:0) was also demonstrated using Model-B.

A series of steered MD simulations were performed to determine the free energy change in removing a molecule from the center of a stack. A monomer in the core of an oligomer is stabilized by $\approx$ 18 kcal/mol with respect to its dispersed state in bulk solvent. These simulations demonstrate the feasibility of monomer exchange between the stacks and the bath of monomers in solution, which forms the basis of a principle called 'Sergeants-and-Soldiers' [13] in the domain of supramolecular polymers. ABF simulations yielded rich details on the cooperativity in FE in the binding of a molecule to oligomers of various sizes. A molecule is more strongly bound to longer oligomers than to smaller ones. These FE calculations also demonstrate

that polymerization in these systems is one of downhill cooperativity and that the size of the nucleus is more likely to be three rather than two [34, 35].

The approach presented in this chapter can be adopted for many molecules being investigated in the domain of supramolecular polymer chemistry [37]. In particular, the sticky dipole approach has not been explored much in molecular systems and we hope that the current work will motivate more efforts in this direction. Although the model developed here is specific for BTA with hexyl tail, it is applicable to systems with other lengths of alkyl tail. This aspect encourages us to study the effects of varying alkyl tail lengths on the aggregate morphology. Modifications in the molecule such as the addition of different functionalities, linkers and the self-assembling moiety can, in principle, be modelled using the procedure followed here. It may also be pertinent to develop much simpler models which incorporate solvent effects implicitly [38].

We have extensively used atomistic and coarse-grain simulations to characterize the mechanisms of self-assembly, structural details of assemblies and predict the supramolecular aggregation starting from the random configurations in *n*-nonane solution. This encourages us to extend our study to explore liquid-crystalline phase of BTAs.

Bibliography

[1] Karimi-Varzaneh, H. A.; van der Vegt, N. F. A.; Müller-Plathe, F.; Carbone, P. *ChemPhysChem* **2012**, *13*, 3428–3439.

[2] Shinoda, W.; Discher, D. E.; Klein, M. L.; Loverde, S. M. *Soft Matter* **2013**, *9*, 11549–11556.

[3] Prasitnok, K.; Wilson, M. R. *Phys. Chem. Chem. Phys.* **2013**, *15*, 17093–17104.

[4] Kawamoto, S.; Shinoda, W. *Soft Matter* **2014**, *10*, 3048–3054.

[5] Nawaz, S.; Carbone, P. *J. Phys. Chem. B* **2014**, *118*, 1648–1659.

[6] Samanta, S. K.; Bhattacharya, S.; Maiti, P. K. *J. Phys. Chem. B* **2009**, *113*, 13545–13550.

[7] Mondal, J.; Mahanthappa, M.; Yethiraj, A. *J. Phys. Chem. B* **2013**, *117*, 4254–4262.

[8] Klein, M. L.; Shinoda, W. *Science* **2008**, *321*, 798–800.

[9] Shinoda, W.; DeVane, R.; Klein, M. L. *Mol. Simul.* **2007**, *33*, 27–36.

[10] Schor, M.; Ensing, B.; Bolhuis, P. G. *Faraday Discuss.* **2010**, *144*, 127–141.

[11] Bhargava, B. L.; Devane, R.; Klein, M. L.; Balasubramanian, S. *Soft Matter* **2007**, *3*, 1395–1400.

[12] DeVane, R.; Klein, M. L.; Chiu, C.-c.; Nielsen, S. O.; Shinoda, W.; Moore, P. B. *J. Phys. Chem. B* **2010**, *114*, 6386–6393.

[13] Palmans, A. R. A.; Vekemans, J. A. J. M.; Havinga, E. E.; Meijer, E. W. *Angew. Chem. Int. Ed.* **1997**, *36*, 2648–2651.

[14] Gasteiger, J.; Marsili, M. *Tetrahedron* **1980**, *36*, 3219 – 3228.

[15] Stockmayer, W. H. *J. Chem. Phys.* **1941**, *9*, 398–402.

[16] Bartke, J.; Hentschke, R. *Phys. Rev. E* **2007**, *75*, 061503.

[17] Orsi, M. *Mol. Phys.* **2014**, *112*, 1566–1576.

[18] Orsi, M.; Essex, J. W. *Faraday Discuss.* **2013**, *161*, 249–272.

[19] Nosé, S. *J. Chem. Phys.* **1984**, *81*, 511–519.

[20] Hoover, W. G. *Phys. Rev. A* **1985**, *31*, 1695–1697.

[21] Schneider, T.; Stoll, E. *Phys. Rev. B* **1978**, *17*, 1302–1322.

[22] Plimpton, S. *J. Comput. Phys.* **1995**, *117*, 1 – 19.

[23] Fiorin, G.; Klein, M.; Hénin, J. *Mol. Phys.* **2013**, *111*, 3345–3362.

[24] Humphrey, W.; Dalke, A.; Schulten, K. *J. Molec. Graphics* **1996**, *14*, 33–38.

[25] Jmol: an open-source Java viewer for chemical structures in 3D. http://www.jmol.org/.

[26] Darve, E.; Rodríguez-Gómez, D.; Pohorille, A. *J. Chem. Phys.* **2008**, *128*, 144120.

[27] Martínez, L.; Andrade, R.; Birgin, E. G.; Martínez, J. M. *J. Comput. Chem.* **2009**, *30*, 2157–2164.

[28] Diffusion coefficients were determined from AA and CG simulations of one BTA in 500 *n*-nonane molecules at 298.15 K. $D_{AA} = 1.68 \times 10^{-7}$ cm^2 s^{-1} and $D_{CG} = 34.26 \times 10^{-7}$ cm^2 s^{-1}.

[29] Albertazzi, L.; van der Zwaag, D.; Leenders, C. M. A.; Fitzner, R.; van der Hofstad, R. W.; Meijer, E. W. *Science* **2014**, *344*, 491–495.

[30] Park, S.; Khalili-Araghi, F.; Tajkhorshid, E.; Schulten, K. *J. Chem. Phys.* **2003**, *119*, 3559–3566.

[31] Park, S.; Schulten, K. *J. Chem. Phys.* **2004**, *120*, 5946–5961.

[32] Jarzynski, C. *Phys. Rev. Lett.* **1997**, *78*, 2690–2693.

[33] De Greef, T. F. A.; Smulders, M. M. J.; Wolffs, M.; Schenning, A. P. H. J.; Sijbesma, R. P.; Meijer, E. W. *Chem. Rev.* **2009**, *109*, 5687–5754.

[34] Jonkheijm, P.; van der Schoot, P.; Schenning, A. P. H. J.; Meijer, E. W. *Science* **2006**, *313*, 80–83.

[35] Markvoort, A. J.; ten Eikelder, H. M. M.; Hilbers, P. A. J.; de Greef, T. F. A.; Meijer, E. W. *Nat. Commun.* **2011**, *2*, 509.

[36] RMSD was used as the colvar variable to restrain the geometry of the oligomer.

[37] Jain, A.; George, S. J. *Mater. Today* **2015**, *18*, 206–214.

[38] Vila Verde, A.; Frenkel, D. *Soft Matter* **2016**, *12*, 5172–5179.

Chapter 4

External Electric Field Reverses Helical Handedness of a Supramolecular Columnar Stack

4.1 Introduction

Chiral amplification is the process by which a racemic mixture is preferentially enriched towards an enantiopure system. Molecular crystals [1], covalent [2, 3] and supramolecular polymers [4] have often served as models for biological systems to understand homochirality. Circularly polarized light [5], external fields [6, 7], stirring [8–10] and electrochemical treatment [11] have been used to break the chiral symmetry.

As discussed in previous chapters, benzene-1,3,5-tricarboxamides (BTA) are a class of extensively studied molecules [12]. Each molecule of BTA can form three intermolecular hydrogen bonds, through which self-assembly proceeds in a cooperative

Reprinted with permission from "External Electric Field Reverses Helical Handedness of a Supramolecular Columnar Stack" *Chem. Commun.* **2015**, 51, 16049-16052. Copyright 2015, Royal Society of Chemistry. http://dx.doi.org/10.1039/C5CC05569E

manner leading to the formation of one-dimensional columnar stacks (see Chapter 2). The triple hydrogen bonded network is helical and the dipole moment of the individual hydrogen bonds sum up to yield a macrodipole along the stacking direction (Figure 4.1). Although the formation of such stacks require longer alkyl tails, the generation of a macrodipole can be illustrated with molecules containing a methyl group which reduces the computational cost considerably.

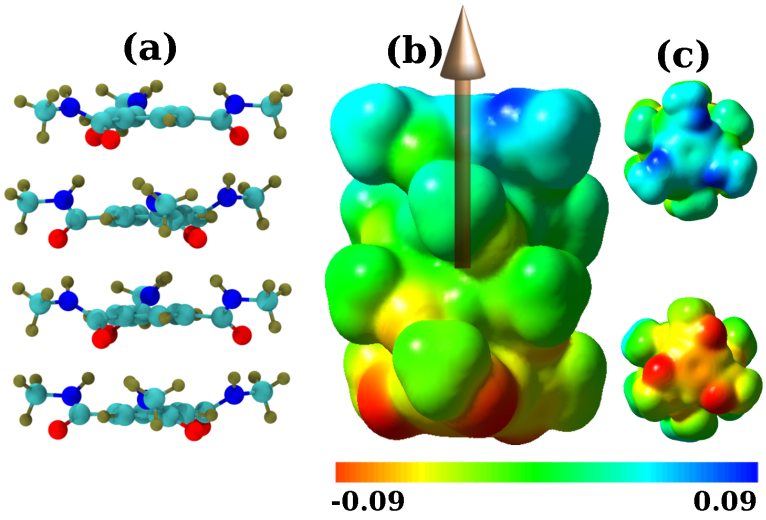

Figure 4.1: (a) Optimized geometry of tetramer of *N,N',N''*-tris(methyl)benzene-1,3,5-tricarboxamide at B3LYP/6-311+g(d,p)//B3LYP/cc-pVTZ level of theory. Side chains are methyl groups. Color: C-cyan; O-red; N-blue; H-tan. (b) Isosurface of electrostatic potential at 0.004 e bohr^{-3}. Arrow indicates macrodipole. (c) Top and bottom views of a tetrameric stack.

In a sample where the supramolecular stacks and fibers are aligned, a macroscopic polarization ensues, whose direction can be switched by an external electric field. Exploiting this aspect, Fitié *et al.* [13, 14] studied the ferroelectric behavior of the liquid crystalline (LC) phase of BTA. Ferroelectricity was demonstrated through a hysteresis loop for systems of achiral BTA molecules. Reorientation of amide bonds was suggested to be responsible for the polar switching [14]. The present chapter explores the microscopic details of these experiments through atomistic molecular dynamics (MD) simulations. Serendipitously, we observe the reversal of the handedness of the molecular assembly on the application of electric field, which

on hindsight, is to be expected based on electrostatic grounds. Thus, an electric field can reorient not only the direction of polarization (the macrodipole vector of a stack), but also the handedness of a supramolecular assembly. In the following, we examine the effects of an external electric field for the cases of chiral and achiral molecular systems in the LC phase using atomistic MD simulations.

In chapter 2, we have shown that a hydrogen-bonded dimer of BTA can exist in two configurations - symmetric (3:0) and asymmetric (2:1), where the symbols in paranthesis denote the number of pairs of hydrogen bond dipole vectors which are parallel:antiparallel to each other. In symmetric stacking, all the oxygens of a molecule are oriented in the same direction with respect to the benzene plane. However, in asymmetric stacking, two oxygens are on one side and the third is on the other side of the benzene plane. Since a stack of BTA molecules consists of three hydrogen-bonded helical networks, the direction of the macrodipole moment of one helix in an asymmetric stack is opposite to those of the other two helices. Asymmetric stacking was argued and shown to be a thermodynamically favoured state over the symmetric one.

4.2 Computational Details

MD simulations were performed using LAMMPS [15] program. BTA molecules were modelled using the DREIDING force field [16]. Gasteiger charges [17] were adopted as partial charges on the atoms. Non-bonded interactions were truncated at 12 Å and long range Coulombic interactions were handled using particle-particle particle-mesh (PPPM) method. Long range corrections to energy and pressure were applied. Three-dimensional periodic boundary conditions were applied. In four of the simulations, α and β were fixed to 90° and the other four cell parameters ($a, b, c, and\ \gamma$) were flexible. Full scaling for 1-4 interactions was adopted. The equations of motion were integrated with a time step of 0.5 fs. The MD simulation was carried out in the constant temperature-constant stress ensemble [18] at 400 K, at which temperature

the LC phase is stable [14]. Snapshots were visualized using VMD [19]. Mean value of the simulation cell parameters when field is OFF and ON are given in Table 4.1 and 4.2, respectively.

Table 4.1: Mean value of the simulation cell parameters when field is in **OFF** state. Lengths and angles are in Å and degrees, respectively.

System	No. of atoms	Run length	a	b	c	α	β	γ
2:1	10260	4 ns	58.2	57.8	35.4	90.0	90.0	113.6
3:0 (400 K)	10260	4 ns	60.9	60.3	35.0	90.0	90.0	58.7
3:0 (370 K)	10260	4 ns	60.1	58.5	35.0	90.0	90.0	61.7
racemic	12480	3 ns	44.3	91.6	35.1	96.6	97.2	77.9
chiral (9 decamers)	9720	4 ns	57.4	57.3	35.3	90.0	90.0	116.6
chiral (16 decamers)	17280	3 ns	55.8	100.1	35.0	81.7	87.1	74.6

Table 4.2: Mean value of the simulation cell parameters when field is in **ON** state. Lengths and angles are mentioned in Å and degrees, respectively.

System	No. of atoms	Run length	a	b	c	α	β	γ
2:1	10260	5 ns	60.0	59.8	35.0	90.0	90.0	61.1
3:0 (400 K)	10260	2 ns	60.7	58.0	35.1	90.0	90.0	64.0
3:0 (370 K)	10260	5 ns	57.6	59.8	35.0	90.0	90.0	62.5
racemic	12480	3 ns	44.0	91.9	35.1	77.7	85.2	95.9
chiral (9 decamers)	9720	3.5 ns	58.0	56.9	35.1	90.0	90.0	115.8
chiral (16 decamers)	17280	3 ns	54.5	103.8	35.1	99.9	76.9	103.8

4.3 Results and Discussion

4.3.1 Solution-phase

The mechanism by which oligomers relax in bulk solution upon application of the applied field has been explored. The simulation was carried out by solvating an oligomer of size 20 in *n*-nonane solution at 298.15 K. An electric field of 0.01 V/Å was applied in a direction opposite to that of the macrodipole. Unlike the LC phase, the oligomer in solution is free to rotate. The stacks are seen to tumble over so as to

align their macrodipole with $\vec{E}$, instead of the hydrogen bond reorganization that was observed in the LC phase (*vide infra*). Such an overall rotation of the stack is not associated with change of handedness. The process is characterized by the angle between initial and instantaneous orientation of an oligomer as shown in Figure 4.2. The cosine of the angle starts at 1 and ends at around -1 indicating the antiparallel orientation of the final configuration with respect to the the initial one. Solution phase is not suitable to study the reversal of handedness in a supramolecular columnar stack.

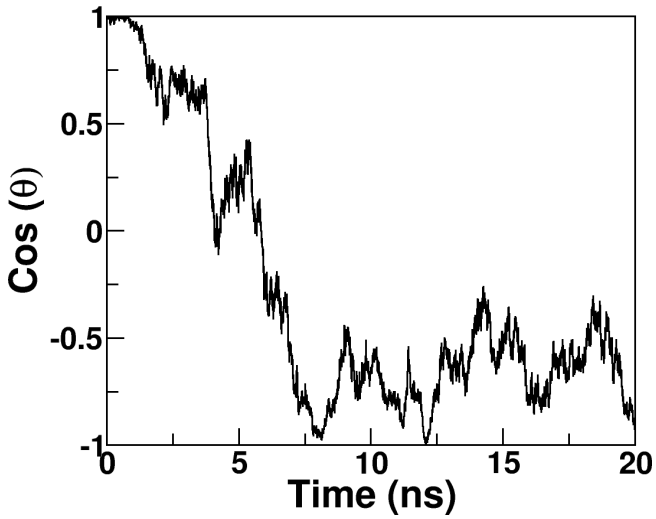

Figure 4.2: MD simulations of a pre-formed BTA oligomer of size 20 solvated in *n*-nonane solution. θ is the angle made by the long axes of the stack in its instantaneous configuration with respect to its initial configuration. The electric field is applied at t=0. In solution, the stack displays an overall rotation upon application of the electric field, with no change in handedness.

4.3.2 Asymmetric LC phase

Nine pre-formed decamers (2:1 kind) of BTA with decyl substituents on the amide hydrogen were taken in a non-orthogonal box, an arrangement which closely resembles the extended LC phase [20], *via* periodic boundary conditions. The stacks were aligned along the z-direction. An initial inter-stack spacing of 30 Å was chosen to avoid hard contacts between alkyl tails. The system was equilibrated for 2 ns during which time the distance between the stacks converged to around 22 Å. Cross-sectional

and side views of the equilibrated system are displayed in Figure 4.3.

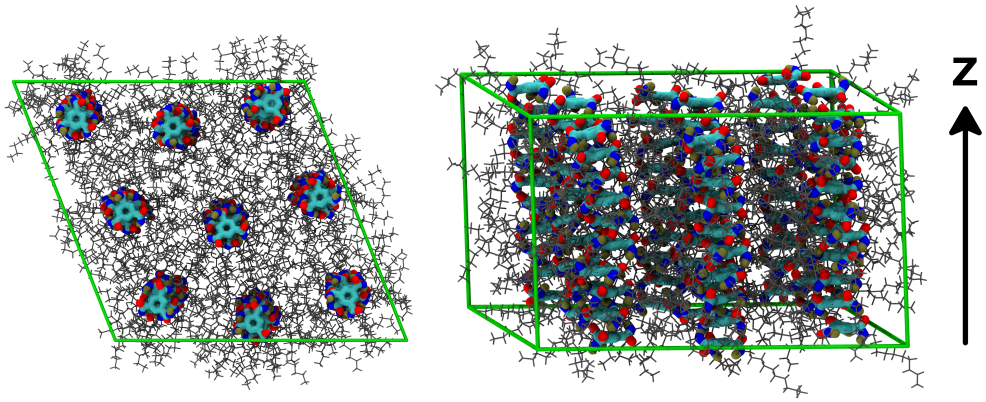

Figure 4.3: Top (left) and side (right) views of the liquid crystalline phase of BTA at 400 K obtained from MD simulations.

Subsequently, a constant external electric field ($\vec{E}$) was applied along the z-direction. From classical theory, a dipole placed in an electric field experiences a torque $\vec{\tau}$=$\vec{p}$ x $\vec{E}$ with potential energy as U= -$\vec{p}$.$\vec{E}$, where $\vec{p}$ is the dipole moment vector. In the presence of the field, the dipole direction of either one or two helices is opposite to that of $\vec{E}$. The hydrogen bonds constituting the helix which are anti-aligned with the field become unstable (*vide infra*) and the individual H-bond dipoles flip so as to align with the field. The sequence of events is: hydrogen bond breakage, bond rotation, followed by the formation of a new hydrogen bond. This process, in effect, transforms the 2:1 type oligomer into a 0:3 one wherein all the helix dipole vectors are oriented parallel to the field. Snapshots of one of the stacks from the MD simulation of the LC phase, before and after the application of the external field are shown in Figure 4.4. Since a 2:1 stack transforms to a 0:3 one due to the external electric field, we shall consider the effect of E-field on 3:0 stacks themselves in the rest of the discussion.

4.3.3 Symmetric LC phase

With the same protocols as before, we proceed to examine the effect of electric field on the LC phase constituted by stacks of 3:0 type. The field was applied in directions either parallel or antiparallel to the macrodipole vector. Expectedly, the former does

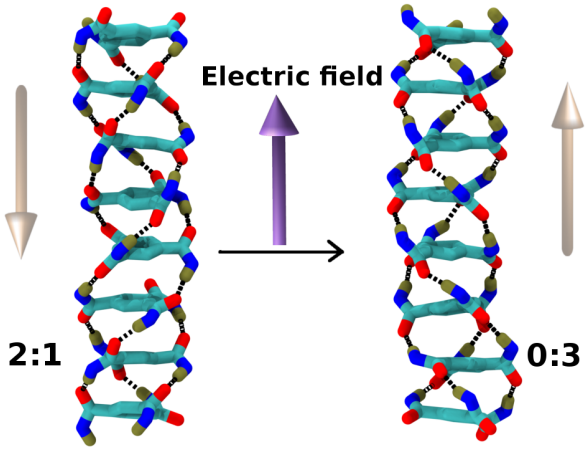

Figure 4.4: Snapshot of one stack from MD simulations of the LC phase at 400 K. The change from an asymmetric (2:1) dipole configuration to a symmetric (0:3) one, upon application of the electric field ($\vec{E}$=0.2 V/Å) is seen. The macrodipole moment is indicated by the brown arrow.

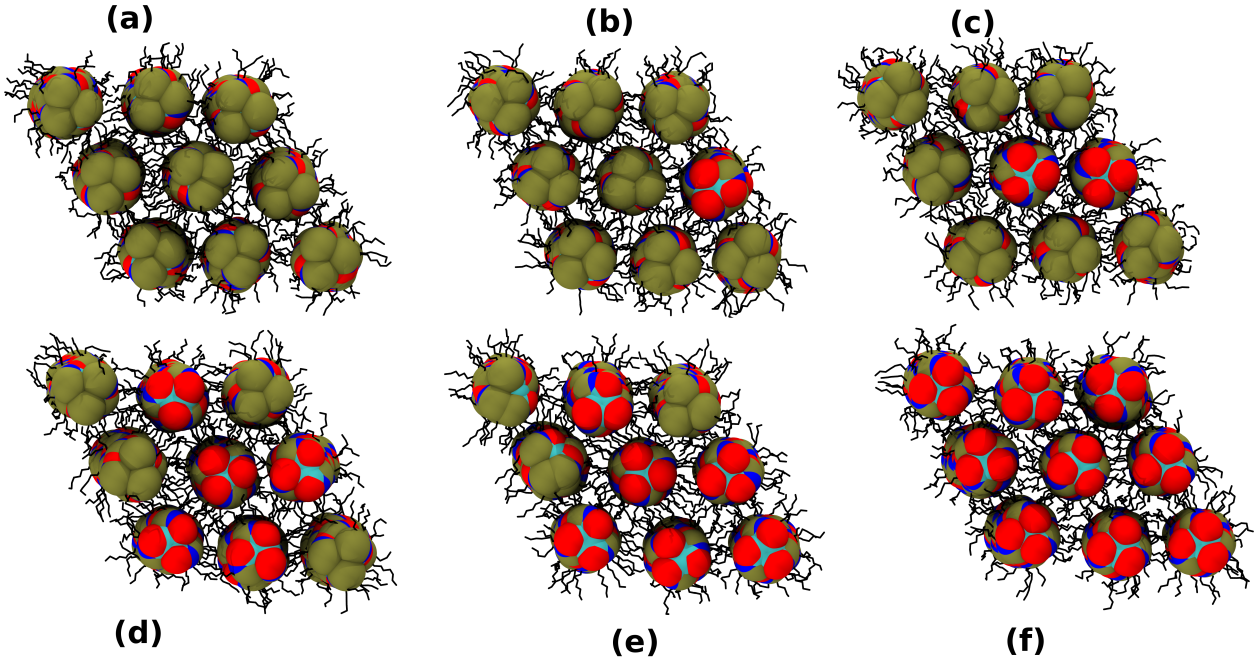

Figure 4.5: Representative snapshots at various times demonstrating the reversal of polarization upon the application of electric field. (a) 0 ns (b) 0.1 ns (c) 0.2 ns (d) 0.5 ns (e) 1.2 ns (f) 2 ns. Oxygens are in red and hydrogens are in tan color. The field is applied at t=0 and is directed into the plane of the paper.

not disturb the structure. In contrast, when the field is applied in a direction opposite to the macrodipole, the stack relaxes by aligning its macrodipole with the field and

the same is observed as a ferroelectric hysteresis loop (P-E loop) [13, 14]. In order to unravel the mechanism of polarization switching, MD simulation of the LC phase (wherein the macrodipoles of all the stacks were parallel to each other) was carried out at 400 K in the NPT ensemble by applying a field of 0.2 V/Å [21] antiparallel to the direction of the macrodipoles. Figure 4.5 illustrates switching of polarization upon application of an external electric field. Initially, the macroscopic polarization points out of the plane, so does the macrodipole moment (hydrogens are shown in tan color). Upon applying an electric field in the direction opposite to that of polarization, each columnar stack reorients its macrodipole to align with field. Thus the direction of macroscopic polarization is reversed (oxygens are shown in red color). Although the torque ($\vec{\tau}$) on the H-bond dipoles is zero, the potential energy (U) of the system is highly positive which destablizes the dipole forcing the macrodipole to align with $\vec{E}$. As the overall rotation of the stacks is infeasible, intermolecular hydrogen bonds within a stack break, so that the amide groups become free to rotate. Since the barrier for the bond rotation is around 1.5 kcal/mol (see Chapter 2), the amide group of each molecule can flip about the benzene plane such that H-bond dipole moment vector ($\vec{p}$) of amide is inverted. Post rotation, they reform the hydrogen bond with a neighboring molecule (different from the one it was initially hydrogen bonded to). In this manner, the triply hydrogen bonded network is regained. However, in this process, the handedness of each hydrogen bonded helix is reversed. A snapshot of an arbitrarily chosen octamer (part of the LC phase) from the MD trajectory demonstrates the switching mechanism (Figure 4.6).

In Figure 4.6, each H-bonded helical network is colored differently so as to clearly distinguish left- and right-handed systems. In the initial geometry, the helices are twisted in clockwise (left-handed) direction, and the electric field makes the helices turn counter-clockwise (right-handed). The dihedral angle between the amide group and benzene plane was used as a parameter to identify the type of handedness.

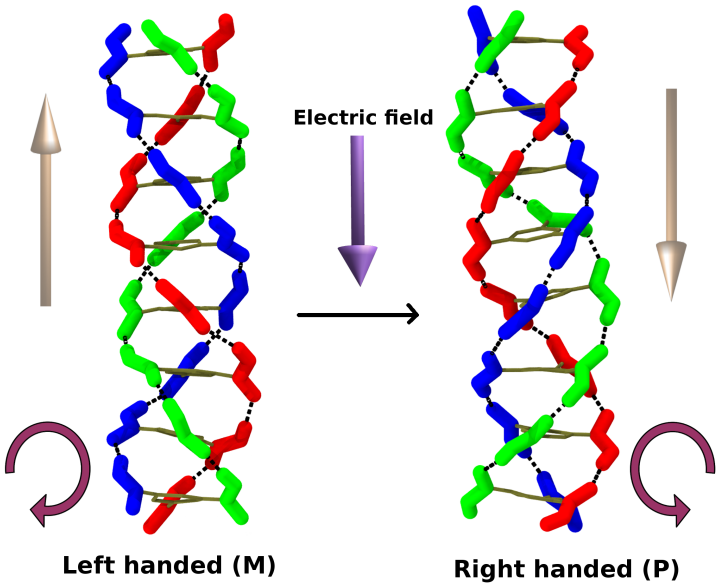

Figure 4.6: Snapshot of a stack from MD simulations of the LC phase illustrates the reversal of chirality on application of electric field. In the initial geometry (left), H-bonded helices are twisted in clockwise direction and the macrodipole points up. Amides present in each H-bonded helix are colored differently. Application of an electric field in the direction opposite to that of the macrodipole reverses the handedness i.e., the helical twist turns counter-clockwise.

Determination of handedness of stack

The dihedral angle ($C_{Ar} - C_{Ar} - C - O$, see Figure 4.7) between the amide group and benzene plane determines the type of handedness taken by the hydrogen bonded helical network in an oligomer. The conditions on this angle can be described as follows:

$$Dihedral\ angle(\theta) = \begin{cases} -90^\circ < \theta < 0^\circ \\ 90^\circ < \theta < 180^\circ \end{cases} Left - handed \quad \begin{cases} -180^\circ < \theta < -90^\circ \\ 0^\circ < \theta < 90^\circ \end{cases} Right - handed \tag{4.1}$$

The progress of the change in handedness over time is shown in Figure 4.8. The fraction of dihedrals which are left-handed exhibits step-wise changes. The same quantity for individual stacks is shown in Figure 4.9a. The time taken for

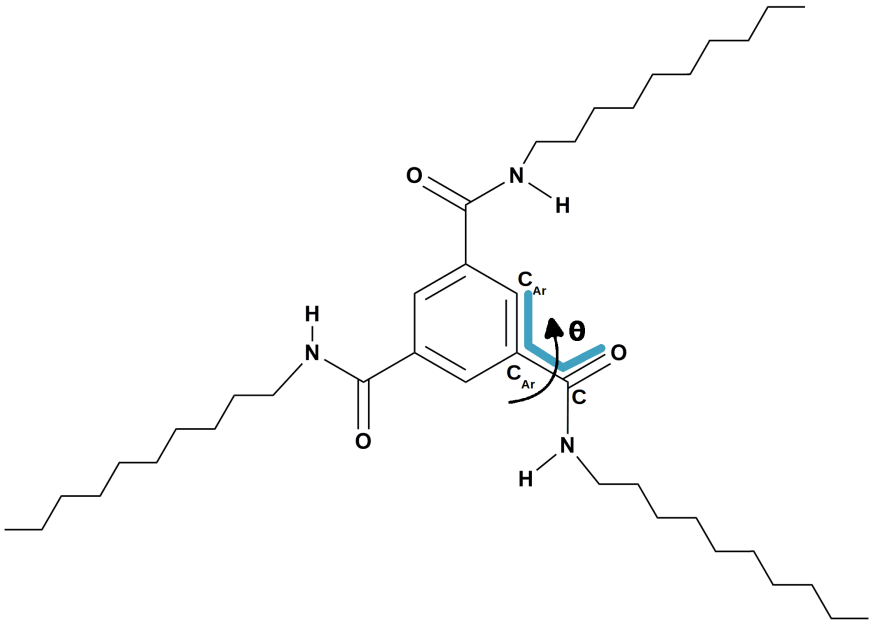

Figure 4.7: *N,N',N''*-tris(decyl)benzene-1,3,5-tricarboxamide. Value of the dihedral angle ($C_{Ar} - C_{Ar} - C - O$) determines the type of handedness of the hydrogen bonded helical network in an oligomer. One such dihedral is marked.

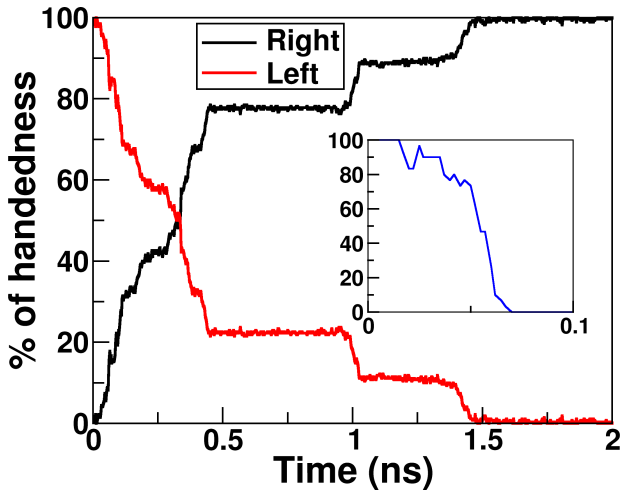

Figure 4.8: Change of handedness of BTA stacks in the LC phase with time. The ordinate is the fraction of dihedrals ($C_{Ar} - C_{Ar} - C - O$) that are left-handed. An electric field of magnitude 0.2 V/Å was applied at a temperature of 400 K at t=0. Inset shows the same for an arbitrarily chosen stack.

any stack to reverse its macrodipole is rather short (Inset to Figure 4.8). Thus, the reversal of handedness proceeds in a sequential manner – one stack completely switches its direction, followed by the next and so on, i.e., *each oligomer switches its*

handedness independent of the others. The effect of temperature and field strength on the switching mechanism was examined by carrying out additional simulations at different conditions: (i) 370 K & 0.2 V/Å (Figure 4.9b) and (ii) 400 K & 0.1 V/Å (Figure 4.10). Reversal of handedness was observed in these two simulations as well but the rate of switching was considerably slower than at 400 K & 0.2 V/Å [22]. Our simulations thus strongly suggest that a handedness reversal should have been concomitant with ferroelectric switching in the experiments of Sijbesma and co-workers [13, 14].

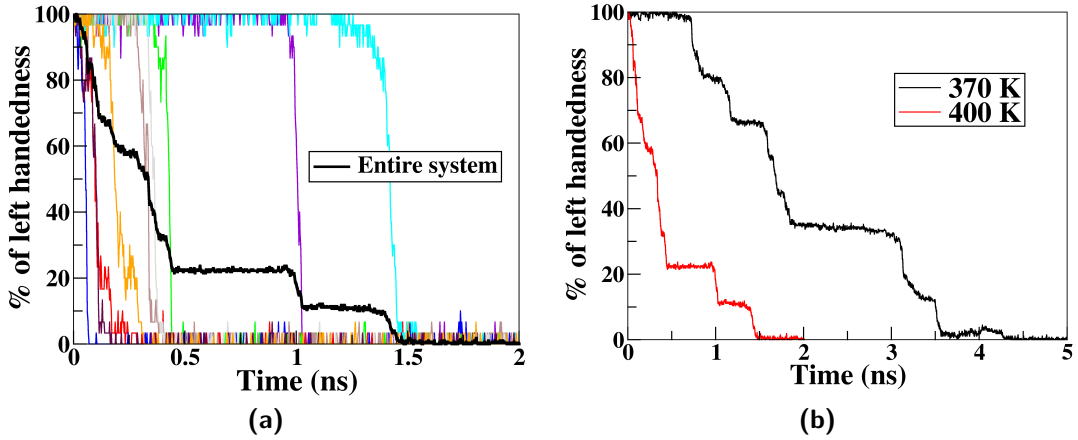

Figure 4.9: (a) Switching of handedness of each oligomer in the LC phase, upon application of an external electric field of magnitude 0.2 V/Å as a function of time. Each color indicates a different oligomer. Black is the average and is the same as the one shown in Figure 4.8. (b) Comparison of the reversal of handedness at two different temperatures. Upon cooling the system, handedness reversal is slowed down.

The identification of handedness in a MD simulation is rather straightforward. Yet, in order to substantiate our conclusions, we calculated the circular dichroism (CD) spectrum using the semi-empirical ZINDO/s method within Gaussian09 [23]. The initial and final coordinates of eight molecules (the core region of an arbitrarily chosen stack) obtained from the MD simulations were used as input for the ZINDO/s calculations. The CD spectra too reveal the reversal of handedness as can be seen from Figure 4.11.

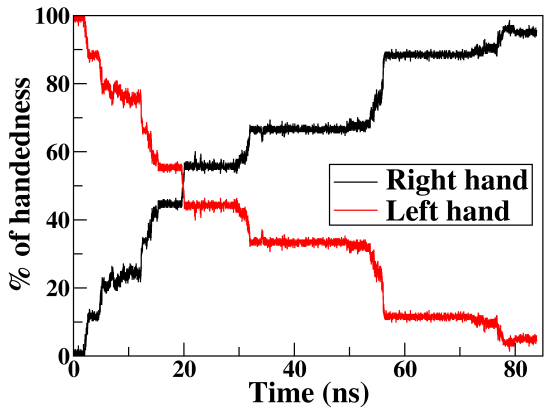

Figure 4.10: Progress of the transformation from left-handed to right-handed enantiomers by applying a small field of magnitude 0.1 V/Å (which is twenty five times that applied typically in experiments [14]). The MD simulations were carried out at 400 K. Reversal of handedness is seen to be accompanied with defects ($\approx 5\%$). Herein, the defect refers to a dihedral whose handedness does not change while the macrodipole aligns with the field. Experiments to observe handedness reversal may be performed at low temperatures so as to decrease the concentration of such defects.

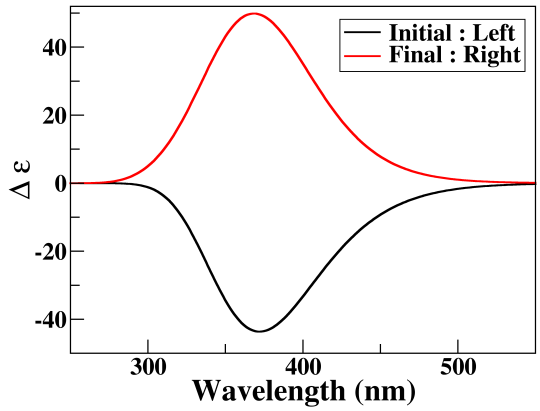

Figure 4.11: Initial and final (upon application of E-field) geometries of an oligomer in the LC phase as described in Figure 4.8 were used as inputs to calculate the CD spectra using the semi-empirical ZINDO/s method.

4.3.4 Proposals for experiments: achiral molecules

We now examine the prospects of investigating the reversal of handedness experimentally. The LC phase of achiral molecules is racemic, whose nature remains unchanged in the presence of an electric field. An achiral supramolecular system will consist of an equal proportion of stacks which are left- or right-handed. Furthermore,

equal fraction of stacks can have their macrodipole moments either aligned or anti-aligned with the electric-field. Accordingly, a LC phase of achiral molecules, with equal number of right- and left-handed stacks was constructed as a model for the racemic mixture. The stacks can be of four types: PU, PD, MU and MD, where 'P' and 'M' stand for right- and left-handed stacks respectively, while 'U' and 'D' denote the direction of the macrodipole moment. The racemic mixture consisted of four stacks of each kind. All the 16 stacks were arranged in a hexagonal packing. MD simulation was carried out in the constant temperature-constant stress ensemble (fully flexible simulation cell) at a temperature of 400 K and the final snapshot is shown in Figure 4.12. After equilibration (over a duration of 2 ns), an external electric field $\vec{E}$ of 0.2 V/Å was applied in the positive z-direction (upwards) on the racemic mixture. Stacks whose macrodipole were aligned with the field remained unaltered. However, intermolecular hydrogen bonds in stacks whose macrodipoles were anti-parallel to the field reoriented so that the resultant macrodipole vector was aligned with the field. As a result, PD stacks converted to MU and MD ones converted to PU. Thus, the mixture remained racemic even after the application of electric field. This process is schematically shown in Figure 4.13a and demonstrated in Figure 4.13. Even after the application of electric field, an equal number of right- and left-handed stacks prevail, keeping the mixture chiro-optically inactive.

4.3.5 Handedness switching of a chiral system aligned with the field

The LC phase of *N-((*S*)*-3,7-dimethyloctyl)-*N',N"*-di(7-methyloctyl)benzene-1,3,5-tricarboxamide was prepared in a fashion similar to that described for the LC phase of the achiral system. We considered that the macrodipole vectors of all the stacks are pointing along the same direction. We have examined the case of a chiral system where the macrodipoles of stacks can be pointing either parallel or anti-parallel to the field (*vide infra*). In the present instant, the chiral (S)-center was present on one of the

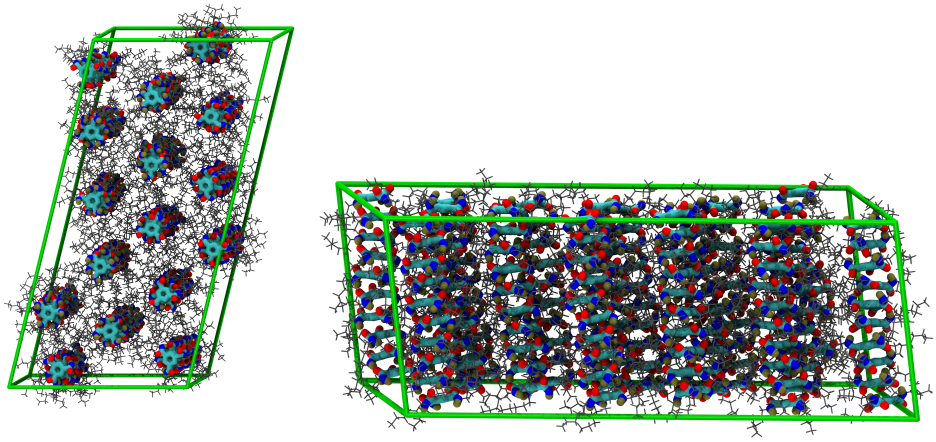

(a) (b)

Figure 4.12: Top and side views of the final configuration in the simulation of the LC phase of a racemic mixture. MD simulation was carried out in fully flexible simulation cell at 400 K.

octyl tails (Figure 4.14). Post equilibration (duration of 2 ns), MD simulation with an electric field of 0.2 V/Å in a direction opposite to the direction of the macrodipole was applied. Within 8 ns, right-handed stacks switch their handedness so as to align with the field, similar to the phenomenon observed for achiral molecules. The same mechanism was found to hold good for these chiral molecules as well (Figure 4.15).

4.3.6 Proposals for experiments: chiral molecules

The macrodipole vectors of a given stack has equal probability to be pointing either up or down. As the chiral center is of 'S' type, the assembly prefers left-handedness [24]. Thus, we constructed a LC phase of the chiral compound out of 8 MU and 8 MD stacks. MD simulation of a LC system consisting of only one enantiomer was carried out with protocols same as those described earlier. This mixture is chiro-optically active. On the application of an electric field in the positive 'Z' direction, a MU stack remains aligned with $\vec{E}$ while MD transforms into PU. Thus, while the original system was optically active (all left handed stacks), application of the electric field nullifies optical activity by changing the handedness of one set of stacks. A schematic representation of this process is depicted in Figure 4.16 and

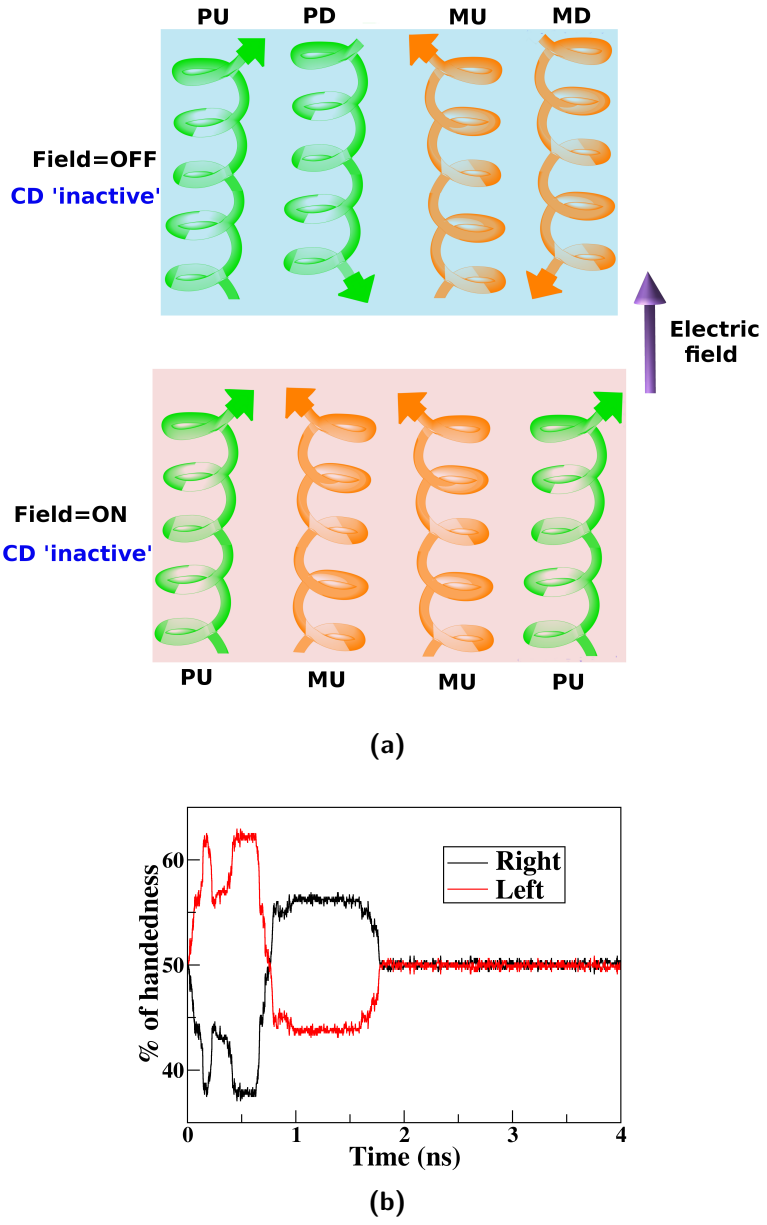

Figure 4.13: (a) Schematic representation of the effect of an external electric field applied on a racemic mixture of stacks. Arrows refer to the direction of the macrodipole vector. Although the electric field transforms the handedness of the stacks which are anti-aligned with it, the resultant configuration continues to be racemic and chiro-optically inactive. (b) Fraction of left or right handedness in hydrogen bonded helices as probed through the dihedral ($C_{Ar} - C_{Ar} - C - O$)) as defined in Equation 4.1. As the initial configuration is a racemic mixture, 50% of each kind is seen. The external electric field converts anti-aligned, right-handed helices to aligned, left-handed helices. It also converts anti-aligned left-handed helices to aligned right-handed ones. Thus, the phase is chiro-optically inactive both in the presence (and absence) of the electric field.

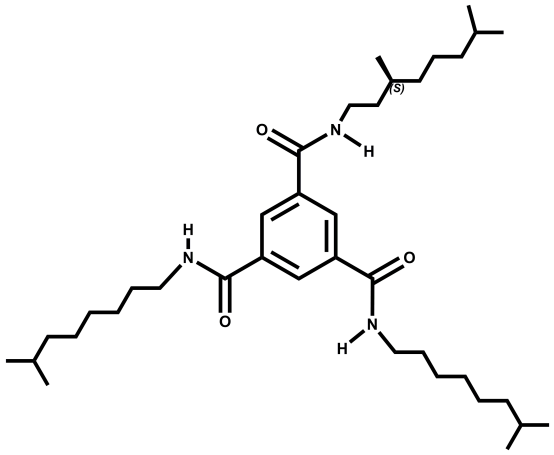

Figure 4.14: *N*-(*(*S*)*-3,7-dimethyloctyl)-*N'*,*N''*-di(7-methyloctyl) benzene-1,3,5-tricarboxamide

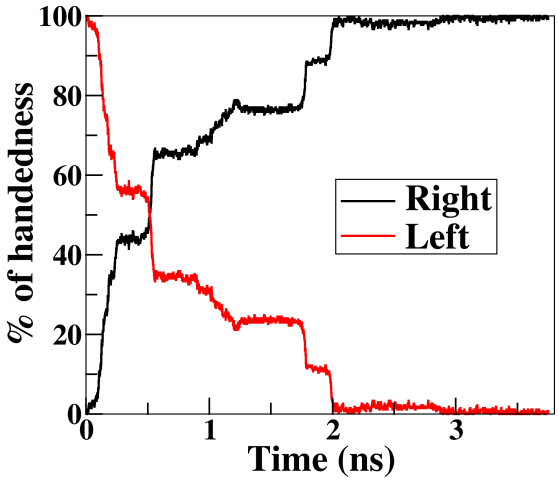

Figure 4.15: Progress in the reversal of handedness of a LC phase formed by chiral molecules. The molecule employed in the simulation is shown in Figure 4.14. Magnitude of the field is 0.2 V/Å and temperature is 400 K.

the conversion of a chiro-optically active mixture into a chiro-optically inactive one is displayed in Figure 4.17. Since stacks can neither exhibit overall rotation nor can disaggregate in the LC phase, the quenching of optical activity upon application of the field will be permanent. The system will be optically inactive even after the removal of the E-field.

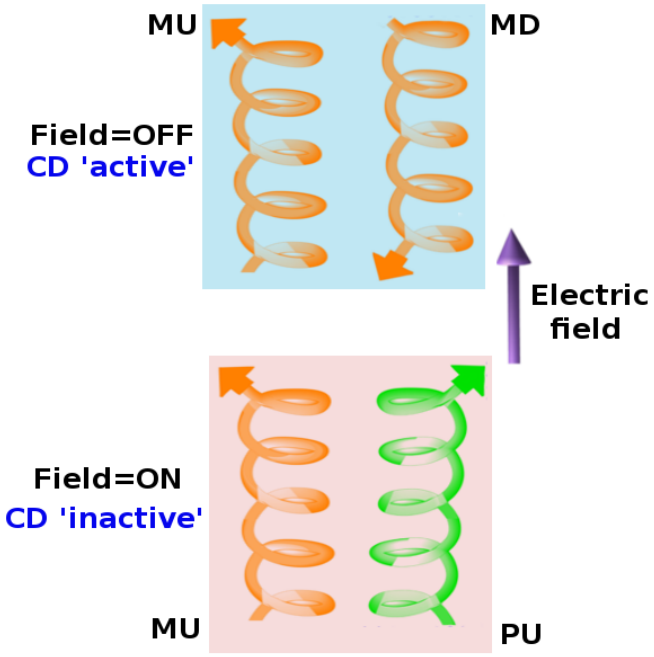

Figure 4.16: Schematic representation of the effect of electric field on a left-handed chiral system. At equilibrium, an equal proportion of stacks with macrodipoles pointing either up or down can exist. Upon application of an external electric field, a stack whose macrodipole is opposite to the field relaxes by changing its handedness. Thus, the chiro-optical activity of the compound is quenched.

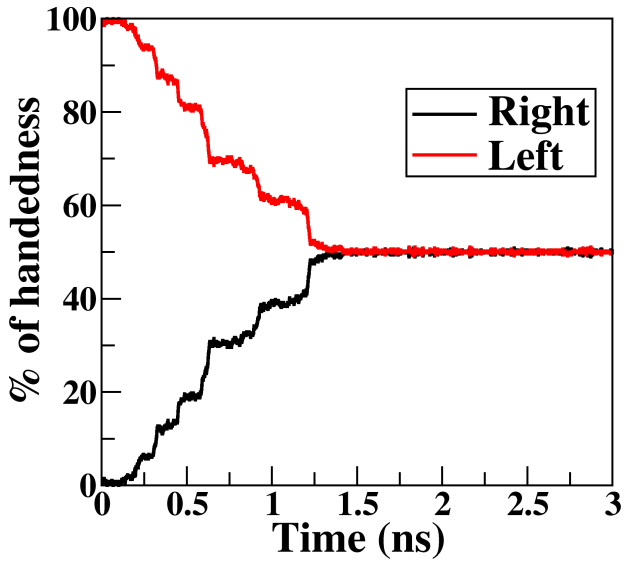

Figure 4.17: Transformation of a enantiomerically pure (left-handed) system into a racemic mixture upon the application of electric field. At t=0, all the stacks are left-handed (100%) which yield equal amounts of left- (50%) and right- (50%) handed stacks on the application of electric field.

4.4 Conclusions

Ferroelectric switching mechanism [13, 14] has been elucidated for columnar stacks of BTA in its liquid crystalline phase using MD simulations. When an external field is applied in a direction opposite to that of the macrodipole, intermolecular hydrogen bonds break, and are re-formed in the opposite direction by virtue of amide bond rotation. This process leads to a reversal of handedness of the stack. *Experimental measurements of the P-E hysteresis loop in hydrogen bonded supramolecular polymers must be associated with such a handedness switch as well, which to our knowledge, has not been recognized yet.* Although the fields employed in the current work are 25 to 50 times larger than experimental values, the mechanism is independent of the field magnitude, and thus should be observable under experimental conditions. It is hoped that the current work will spur experimental efforts in this direction.

Bibliography

[1] Viedma, C.; Ortiz, J. E.; Torres, T. d.; Izumi, T.; Blackmond, D. G. *J. Am. Chem. Soc.* **2008**, *130*, 15274–15275.

[2] Green, M. M.; Park, J.-W.; Sato, T.; Teramoto, A.; Lifson, S.; Selinger, R. L. B.; Selinger, J. V. *Angew. Chem. Int. Ed.* **1999**, *38*, 3138–3154.

[3] Green, M. M.; Cheon, K.-S.; Yang, S.-Y.; Park, J.-W.; Swansburg, S.; Liu, W. *Acc. Chem. Res.* **2001**, *34*, 672–680.

[4] Palmans, A. R. A.; Meijer, E. W. *Angew. Chem. Int. Ed.* **2007**, *46*, 8948–8968.

[5] Bailey, J.; Chrysostomou, A.; Hough, J. H.; Gledhill, T. M.; McCall, A.; Clark, S.; Ménard, F.; Tamura, M. *Science* **1998**, *281*, 672–674.

[6] Edwards, D.; Cooper, K.; Dougherty, R. C. *J. Am. Chem. Soc.* **1980**, *102*, 381–382.

[7] Micali, N.; Engelkamp, H.; van Rhee, P. G.; Christianen, P. C. M.; Scolaro, L. M.; Maan, J. C. *Nat. Chem.* **2012**, *4*, 201–207.

[8] Ribó, J. M.; Crusats, J.; Sagués, F.; Claret, J.; Rubires, R. *Science* **2001**, *292*, 2063–2066.

[9] Yamaguchi, T.; Kimura, T.; Matsuda, H.; Aida, T. *Angew. Chem. Int. Ed.* **2004**, *43*, 6350–6355.

[10] Wolffs, M.; George, S. J.; Tomović Ž.; Meskers, S. C. J.; Schenning, A. P. H. J.; Meijer, E. W. *Angew. Chem. Int. Ed.* **2007**, *46*, 8203–8205.

[11] Yang, X.; Seo, S.; Park, C.; Kim, E. *Macromolecules* **2014**, *47*, 7043–7051.

[12] Cantekin, S.; de Greef, T. F. A.; Palmans, A. R. A. *Chem. Soc. Rev.* **2012**, *41*, 6125–6137.

[13] Fitié, C. F. C.; Roelofs, W. S. C.; Kemerink, M.; Sijbesma, R. P. *J. Am. Chem. Soc.* **2010**, *132*, 6892–6893.

[14] Fitié, C. F. C.; Roelofs, W. S. C.; Magusin, P. C. M. M.; Wübbenhorst, M.; Kemerink, M.; Sijbesma, R. P. *J. Phys. Chem. B* **2012**, *116*, 3928–3937.

[15] Plimpton, S. *J. Comput. Phys.* **1995**, *117*, 1 – 19.

[16] Mayo, S. L.; Olafson, B. D.; Goddard, W. A. *J. Phys. Chem.* **1990**, *94*, 8897–8909.

[17] Gasteiger, J.; Marsili, M. *Tetrahedron* **1980**, *36*, 3219 – 3228.

[18] Parrinello, M.; Rahman, A. *J. Appl. Phys.* **1981**, *52*, 7182–7190.

[19] Humphrey, W.; Dalke, A.; Schulten, K. *J. Molec. Graphics* **1996**, *14*, 33–38.

[20] Timme, A.; Kress, R.; Albuquerque, R. Q.; Schmidt, H.-W. *Chem. Eur. J.* **2012**, *18*, 8329–8339.

[21] The magnitude of the field in simulations is around fifty times larger than that in experiments.

[22] Switching of the handedness of the LC phase by applying an electric field of 0.1 V/Å (twenty five times that of experimental value) takes around 100 ns (Figure 4.9).

[23] Frisch, M. J. et al. Gaussian 09 Revision D.01. Gaussian Inc. Wallingford CT **2009**.

[24] Brunsveld, L.; Schenning, A. P. H. J.; Broeren, M. A. C.; Janssen, H. M.; Vekemans, J. A. J. M.; Meijer, E. W. *Chem. Lett.* **2000**, *29*, 292–293.

Chapter 5

Self-assembly of amino ester-based benzene-1,3,5-tricarboxamides: A molecular dynamics study

5.1 Introduction

In the present chapter, the self-assembly of benzene-1,3,5-tricarboxamide (BTA) molecules appended with amino ester-based moieties have been investigated. BTA with carboxymethyl peripheral groups crystallizes in a face-to-face dimer fashion with six hydrogen bonds [1]. In a recent work, Desmarchelier *et al.* reported the synthesis of three amino ester-based BTAs and the exploration of the effect of three substituents (Met, Nle, and Phe, see Figure 5.1) on the self-assembled structures, as a function of both concentration and temperature [2]. Formation of either one-dimensional long aggregates or of dimers was seen to be dependent on the substituent. At ambient conditions, BTA-Met and BTA-Phe self-assemble into long one-dimensional stacks, while the self-assembly of BTA-Nle does not proceed beyond a dimer. "Sergeants-and-Soldiers" experiments were performed by mixing amino ester-BTAs (sergeants) with alkyl BTAs (soldiers). Chiral amplification for alkyl BTAs (R=octyl, see Figure

5.1) was achieved.

The present study aims at obtaining a microscopic understanding of the role of substituents in stabilizing either the long assemblies or dimers; the structure of the dimeric species in solution is also proposed. We also elucidate the free energy difference between the two variants of dimers as a function of temperature, and address the favourable interactions responsible for the stability of long assemblies. Umbrella sampling simulations to determine the relative FE differences between oligomers and dimers are also presented.

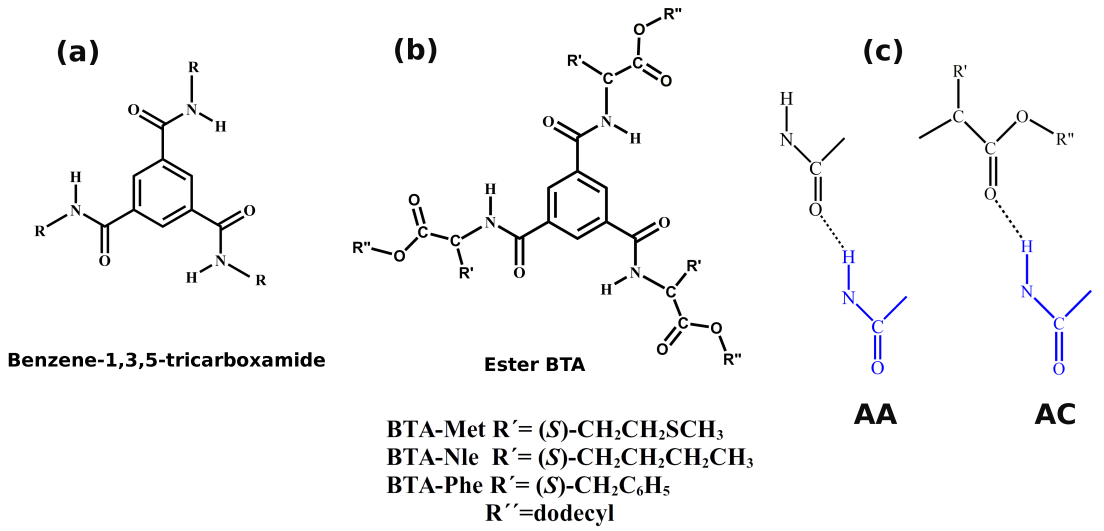

Figure 5.1: (a) Common core for all BTA based compounds (b) Amino ester BTAs studied here (c) Two hydrogen bond types among amino ester BTAs: amide-amide (AA) and amide-carboxylate (AC). Blue and black color indicate different molecules.

5.2 Computational Details

Classical Molecular Dynamics (MD) simulations were performed using LAMMPS [3] package. All-atom DREIDING [4] parameters combined with Gasteiger partial charges [5] on the atomic sites were employed to model the supramolecules . Solvent molecules were modelled through an united atom approach using a TraPPE force field [6]. Cross interactions between the solute and solvent molecules were handled by DREIDING's mixing rules. Real space interactions were truncated at 12 Å and

Table 5.1: Details of the simulated systems. [a] Temperature is 350 K. All other simulations are at 298.15 K. [b] Free energy simulations performed at 298.15 K and length of the trajectory corresponds to the duration in each window.

System	Total No. of atoms	No. of cyclohexane molecules	Mean box length (in Å)	Trajectory length (in ns)
Hexamer (BTA-Met)	16080	2500	76.9	40
Hexamer (BTA-Phe)	16134	2500	76.9	40
AC dimer (BTA-Met)	11724	1894	69.8	25
AA dimer (BTA-Met)	11700	1890	69.7	25
AC dimer (BTA-Nle)	11670	1883	69.7	25
AA dimer (BTA-Nle)	11514	1857	69.4	25
AC dimer (BTA-Phe)	11586	1868	69.5	25
AA dimer (BTA-Phe)	11616	1873	69.6	25
AC dimer (BTA-Met)[a]	11724	1894	71.3	25
AA dimer (BTA-Met)[a]	11700	1890	71.3	25
AC dimer (BTA-Nle)[a]	11670	1883	71.2	25
AA dimer (BTA-Nle)[a]	11514	1857	70.9	25
AC dimer (BTA-Phe)[a]	11586	1868	71.0	25
AA dimer (BTA-Phe)[a]	11616	1873	71.1	25
Dimer (BTA-Met)[b]	11724	1894	69.8	20
Dimer (BTA-Nle)[b]	11670	1883	71.2	20
Dimer (BTA-Phe)[a]	11586	1868	71.0	20
Tetramer (BTA-Met)[b]	23370	3775	87.9	10
Tetramer (BTA-Nle)[b]	23544	3800	88.1	10
Tetramer (BTA-Phe)[b]	23610	3809	88.2	10
Hexamer (BTA-Phe)[b]	17430	2716	79.0	10

long range corrections to energy and pressure were included. Long range Coulombic interactions were handled using particle-particle particle-mesh (PPPM) method. Three-dimensional periodic boundary conditions were applied. Equations of motions were integrated using velocity-Verlet algorithm with a time-step of 0.5 fs. Simulations were carried out in isothermal-isobaric (NPT) ensemble. Temperature and pressure control were achieved by a Nosé-Hoover thermostat [7, 8] and barostat with a coupling constant of 1 ps. 1-4 interactions were treated with full-scaling. Snapshots were

visualized and rendered using VMD [9]. Details of the simulated systems are given in Table 5.1. Criteria adopted to determine AA and AA hydrogen bonds [10], and CH$\cdots$S and CH$\cdots\pi$ weak hydrogen bonds [11, 12] are listed in Table 5.2.

Table 5.2: Various hydrogen bond types and criteria adopted to determine their existence. D: Donor; A: Acceptor

Hydrogen bond type	D-A distance (in Å)	Minimum D-H-A angle (°)
AA	3.3	140
AC	3.3	140
CH$\cdots$S	3.6	110
CH$\cdots\pi$	3.9	110

Quantum chemical calculations were performed using both Gaussian09 [13] and CP2K [14] softwares. In Gaussian09, optimizations of two dimer variants have been carried out at B3LYP/6-31g(d,p) level of theory. In CP2K calculations, all valence electrons were treated in a mixed basis with an energy cutoff of 280 Ry. The short range basis of triple-ζ single polarization (TZVP) was used. Effect of core electrons and nuclei were handled by Goedecker-Teter-Hutter (GTH) [15] pseudo-potentials. The exchange and correlation interactions between the electrons were treated within Perdew-Burke-Ernzerhof (PBE) [16] functional. Empirical van der Waals terms were accounted using DFT-D3 [17] approach developed by Grimme.

Free energy calculations have been performed using the colvars module [18] implemented in LAMMPS [3] package. Umbrella Sampling (US) [19] technique has been employed to estimate the relative free energies between two states. UWHAM [20, 21] was used to obtain the free energies along the reaction coordinate (RC).

5.3 Results and Discussion

5.3.1 Energy differences between the two dimers

Amino ester-based BTAs considered here can dimerize into two different forms with differing hydrogen bonding patterns; the NH of amide group can hydrogen bond with the oxygen of either the amide (AA) or the carboxylate (AC) group of another

molecule. In an AA dimer, three hydrogen bonds (H-bonds) are formed between the amide 'NH' of one molecule and amide 'O' of another molecule, shown in Figure 5.2a. This dimer possesses free hydrogen bonding sites which can be exploited to extend it further to larger oligomers. The hydrogen bonding network in an AA dimer is similar to that in traditional alkyl BTAs (see Chapter 2); thus, an AA dimer acts as a basic building block for an assembly. On the other hand, in an AC dimer, hydrogen bonds are formed between the amide 'NH' of one molecule and the carboxylate 'O' of another molecule, and *vice versa*, shown in Figure 5.2b. Face-to-face dimerization of two molecules in such an AC dimer leads to the formation of six hydrogen bonds, leaving no free hydrogen bonding sites. Such a dimer cannot be further extended to an oligomer.

Energy differences between the two variants of dimers for R'=CH_2CH_3 and R"=CH_3 have been determined using both quantum chemical calculations and empirical force field at zero Kelvin and they are provided in Table 5.3. Clearly, the AC dimer is more stable than the corresponding AA dimer, independent of the level of theory. The energy difference between the two dimer types arise due to: (i) Differing number of hydrogen bonds and (ii) Dihedral Penalty: in an AC dimer, the 'NH' group hydrogen bonds with the carboxylate oxygen of another molecule within the plane of the former's benzene ring; thus, the amide group has no need to rotate about the benzene plane (see Figure 5.2). On the other hand, in an AA dimer, the amide group rotates about the benzene plane so as to form hydrogen bonds. As a result, a dihedral penalty of 0.25 kcal/mol (see Chapter 2) is associated for each such dihedral in the AA configuration.

In summary, the AC dimer is more stable than the AA dimer both by way of having more hydrogen bonds and also by not incurring dihedral penalty.

Table 5.3: Energy difference ($E_{AA}-E_{AC}$) (in kcal/mol) between the two optimized dimers of amino ester-based BTA for R'=CH_2CH_3 and R"=CH_3 at zero Kelvin. Zero point energy corrections (ΔE_{ZPE}=-2.4 kcal/mol) are included in the B3LYP data.

Method	$\Delta E=E_{AA}-E_{AC}$
DREIDING	20.7
B3LYP/6-31g(d,p)	12.5
PBE-D3	27.9

5.3.2 Favourable interactions in an assembly

Desmarchelier *et al.* observed the formation of long assemblies for BTA-Met and BTA-Phe in cyclohexane solvent at ambient conditions, but not so for the case of BTA-Nle [2]. The discussion above showed that BTA molecules can aggregate into long stacks only *via* AA hydrogen bonding pattern. Thus, although an AC dimer is favoured over the corresponding AA dimer by a large extent, albeit in gas phase, there must be some additional stability accruing in an oligomer, which overcomes the energy difference between the two dimer types. To understand the stability of an oligomer, a hexamer of BTA-Met and BTA-Phe each were geometry optimized at PBE-D3 level of theory using CP2K [14] and at HF/STO-3G level of theory with Gaussian09 [13]. In these calculations, R" was truncated to hexyl instead of the dodecyl used in experiments [2], to decrease the computational cost. In the case of BTA-Met, sulfur forms weak hydrogen bonds with the CH of alkyl tails (see Figure 5.3). A total of ten CH$\cdots$S hydrogen bonds were observed in a hexamer of BTA-Met. Similarly, in a hexamer of BTA-Phe, the phenyl rings were observed to participate in weak CH$\cdots\pi$ hydrogen bonds (see Figure 5.3). Thus, CH$\cdots$S [11, 22, 23] and CH$\cdots\pi$ [11, 24–26] hydrogen bonds likely stabilize the longer assemblies of BTA-Met and BTA-Phe, respectively. However, such specific interactions are not available in BTA-Nle molecules, and thus their self-assembly is just limited to dimers. Additionally, oligomers of BTA-Met and BTA-Phe are stabilized *via* 1-3 interactions. The aggregate strength of 1-3 interactions in a hexamer of BTA-Met and BTA-Phe

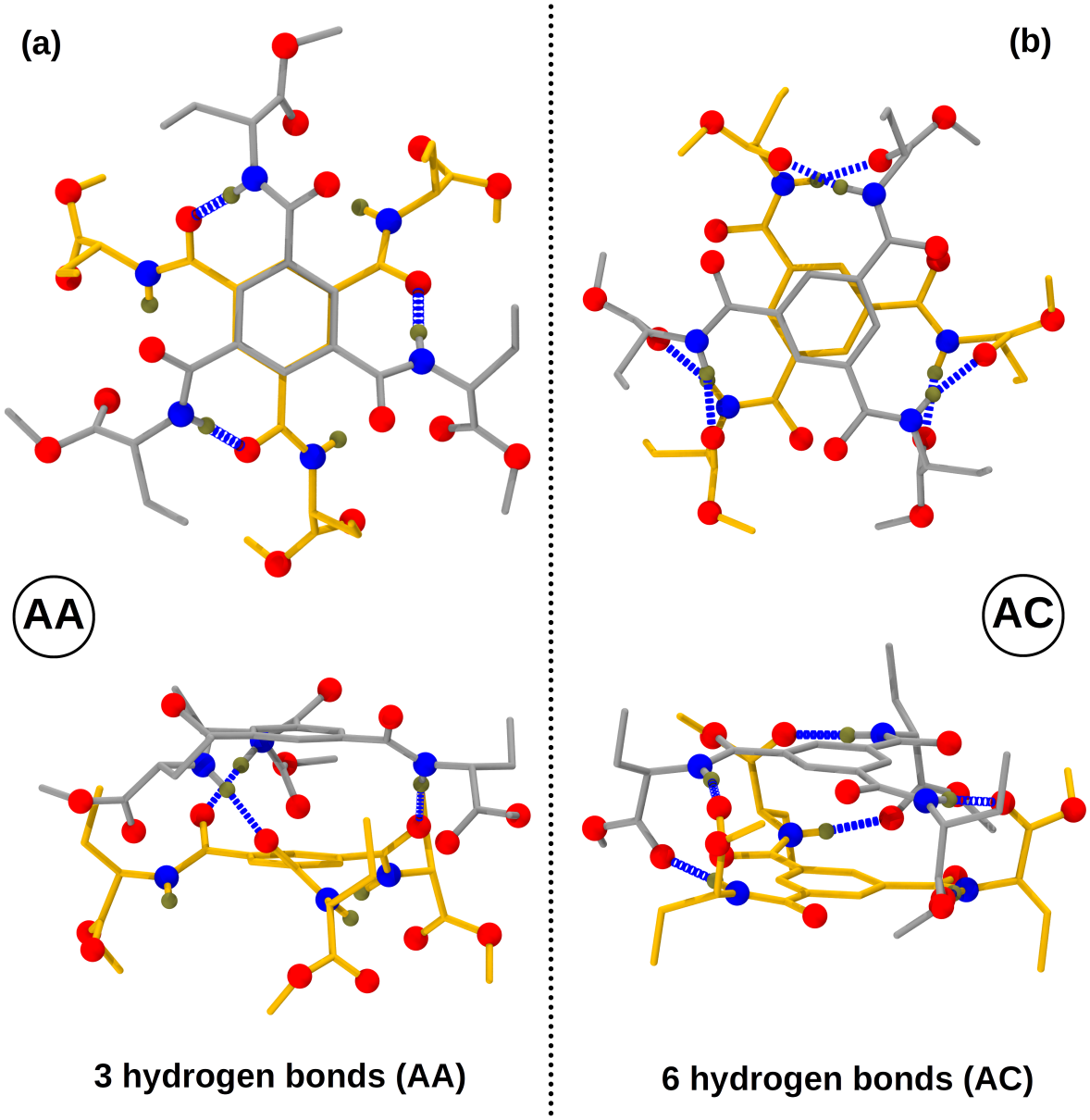

Figure 5.2: Top and side views of both types of dimers with R'=CH_2CH_3 and R"=CH_3. (a) Amide-amide (AA) dimer (b) Amide-carboxylate (AC) dimer. Color scheme: carbon (molecule 1)-gray; carbon (molecule 2)-yellow; oxygen-red; nitrogen-blue; hydrogen-tan; non-polar hydrogens are not shown for clarity.

in solution were -52 kcal/mol and -58 kcal/mol respectively.

An oligomer of size n contains 3(n-1) AA hydrogen bonds, while equivalently, n such molecules can form n/2 AC dimers, each possessing 6 AC hydrogen bonds. Therefore, an oligomer possesses 3(n-1) AA H-bonds while the corresponding AC

dimers can have 3n AC H-bonds. Although the former contains three fewer hydrogen bonds, 1-3 interactions can contribute significantly towards its stabilization. As mentioned earlier, the oligomers of BTA-Met and BTA-Phe are further stabilized by CH$\cdots$S and CH$\cdots\pi$ interactions respectively.

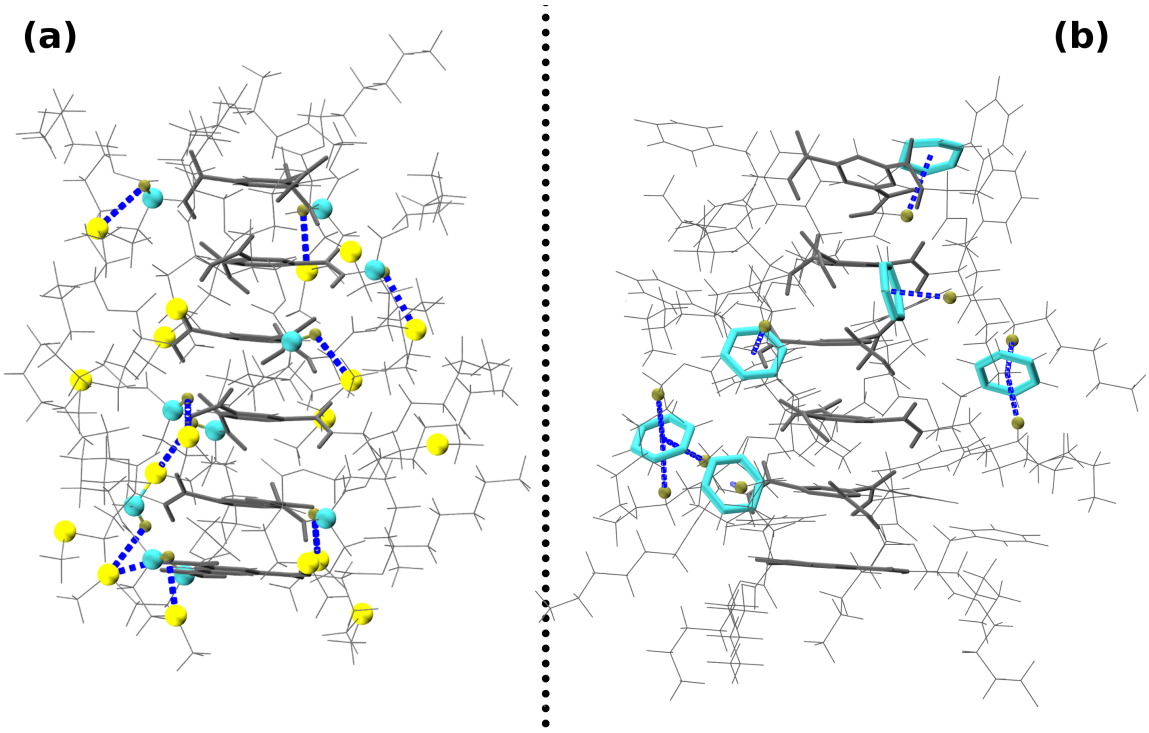

Figure 5.3: Optimized hexamer geometries (with R"=C_6H_{13}) of BTA-Met and BTA-Phe obtained at PBE-D3 level of theory. (a) CH$\cdots$S hydrogen bonds are highlighted in an assembly of BTA-Met. (b) CH$\cdots\pi$ hydrogen bonds are highlighted in the BTA-Phe hexamer. Color scheme: sulfur-yellow; carbon-cyan; hydrogen-tan.

Zero Kelvin, gas-phase, optimized structures of BTA-Met and BTA-Phe demonstrate the existence of weak CH$\cdots$S and CH$\cdots\pi$ hydrogen bonds, respectively. However, it remains to be seen if these interactions hold good in the solution phase at finite temperature, the solvent being cyclohexane. Pre-formed hexamers of BTA-Met and BTA-Phe with R"=dodecyl were soaked in explicit cyclohexane solvent and MD simulations were carried out at 298.15 K. Configurations were saved every 2.5 ps for post-processing and visualization. The distance between the core benzene ring and the last carbon of all the three dodecyl tails of the central two molecules of the hexamer

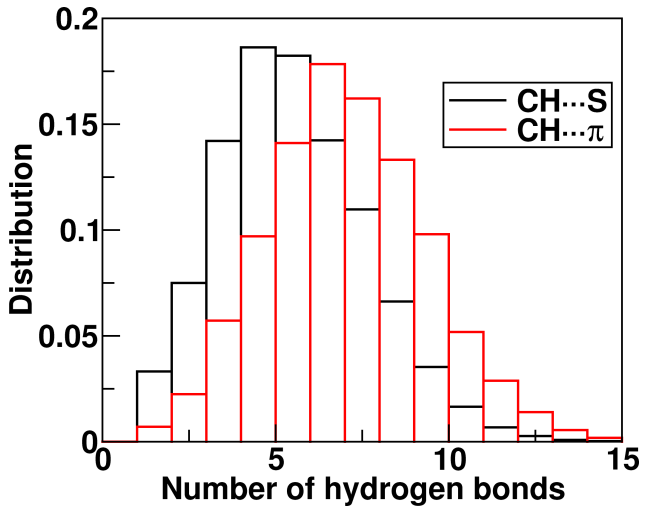

Figure 5.4: Distribution of the number of CH$\cdots$S and CH$\cdots\pi$ weak hydrogen bonds in a hexamer of BTA-Met and BTA-Phe, respectively. Simulations have been performed in cyclohexane solvent at 298.15 K.

was determined. The distribution of the distances for BTA-Met and BTA-Phe are shown in Figure 5.5 from which we obtain the cross-sectional radii of BTA-Met and BTA-Phe to be 17.8 Å and 18.0 Å respectively which are quite comparable to the experimental values of 16.0 Å and 16.5 Å respectively [2]. All the amide-amide (AA) hydrogen bonds were found to be intact throughout the simulations which implies that the force field parameters adopted here represent the system reasonably well. The distribution of the number of CH$\cdots$S and CH$\cdots\pi$ hydrogen bonds in the BTA-Met and BTA-Phe systems respectively are shown in Figure 5.4. The persistence of such interactions at ambient conditions strongly suggests the stabilization of oligomeric structures over their dimeric species.

5.3.3 Stability of dimers at finite temperature

Having understood the stability of long oligomers of BTA-Met and BTA-Phe, we revert our attention back to the two types of dimers: AA and AC. We would like to elucidate the stability of the two variants of dimers for all the three substituents (Met, Nle, Phe) at finite temperature in explicit cyclohexane solvent. For each derivative, simulations were performed starting with either the AC or AA dimer soaked in a

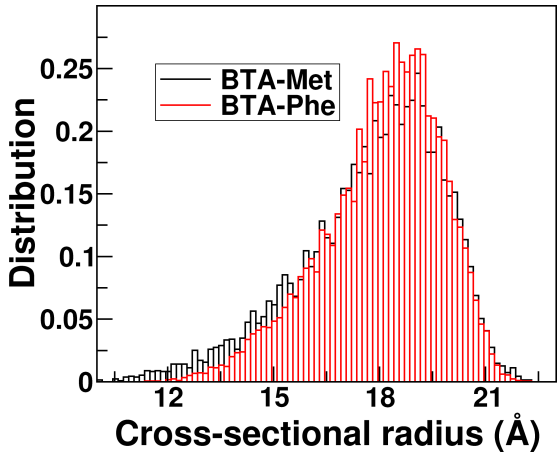

Figure 5.5: Distribution of the distance between the benzene ring and the last carbon of dedecyl chain, averaged over the two molecules in the core of a hexamer in solution.

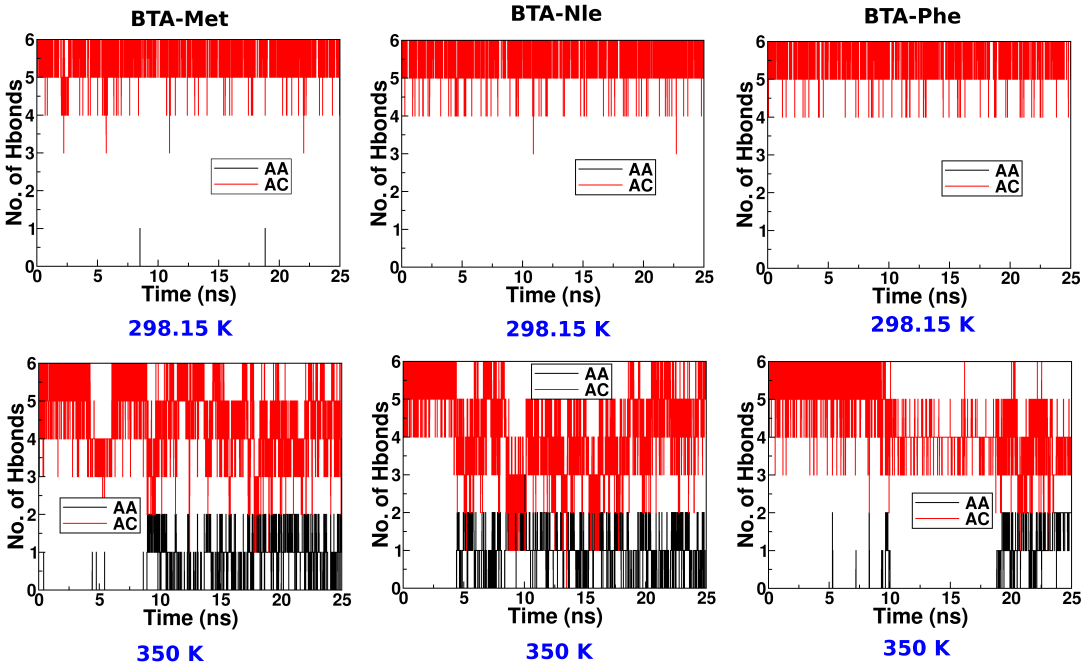

Figure 5.6: MD simulations started from an AC dimer (6 AC hydrogen bonds) configuration soaked in explicit cyclohexane solution were performed in the NPT ensemble. The number of AA and AC hydrogen bonds as a function of time for the three derivatives at 298.15 K (top panel) and 350 K (bottom panel) are shown. For BTA-Met: R'=$CH_2CH_2SCH_3$, BTA-Nle: R'=$CH_2CH_2CH_2CH_3$, BTA-Phe:R'=$CH_2C_6H_5$ and R"=dodecyl.

well-equilibrated cyclohexane solvent for 5 ns. These simulations were carried out at two temperatures 298.15 K and 350 K in the isothermal-isobaric (NPT) ensemble.

Table 5.4: Mean value of the number of hydrogen bonds for simulations started with either the AC dimer (6 AC hydrogen bonds) or the AA dimer (3 AA hydrogen bonds) at 298.15 K and 350 K. Entries with asterisk represent configurations from a trajectory at 298.15 K which was initiated by cooling the 350 K configuration over 2.5 ns. For BTA-Met: R'=$CH_2CH_2SCH_3$, BTA-Nle: R'=$CH_2CH_2CH_2CH_3$, BTA-Phe:R'=$CH_2C_6H_5$ and R"=dodecyl.

System	Dimer type	Temperature			
		298.15 K		350 K	
		AA HBs	AC HBs	AA HBs	AC HBs
BTA-Met	AC	0	5.8	0.5	4.8
BTA-Nle	AC	0	5.8	0.8	4.3
BTA-Phe	AC	0	5.9	0.3	4.6
BTA-Met	AA	2.9	1.3	1.7	3.0
BTA-Nle	AA	2.8	1.3	1.9	2.3
BTA-Phe	AA	2.8	1.2	2.3	1.8
BTA-Met	AC*	0.5	5.2	-	-
BTA-Nle	AC*	0.4	4.5	-	-
BTA-Phe	AC*	1.9	3.7	-	-

The number of AA and AC hydrogen bonds as a function of time in these simulations are plotted in Figures 5.6 and 5.7. The mean values of the number of hydrogen bonds are provided in Table 5.4.

298.15 K: Simulations started with an AC dimer reveal that the six AC H-bonds are quite stable for all the three derivatives. Figure 5.6 shows the total number of AC and AA H-bond types as a function of time. Simulations starting from an AA dimer (i.e. with three H-bonds of AA type) were also performed and the number of H-bonds (both AA and AC type) as a function of time are shown in Figure 5.7. At t=0, such a dimer possesses 3 AA and 0 AC H-bonds, but with time, it gains AC H-bonds and attempts to transform into an AC dimer. Within the time-scales accessed here, the AA dimer may not completely transform itself to an AC dimer, and 'equilibrium' configuration consists of hydrogen bonds of both AA and AC types.

350 K: Interestingly, at 350 K, a few AC H-bonds are broken to result in the formation of AA H-bonds. Although such events are not seen at 298.15 K within the timescales studied here, one cannot rule them out as the ambient temperature

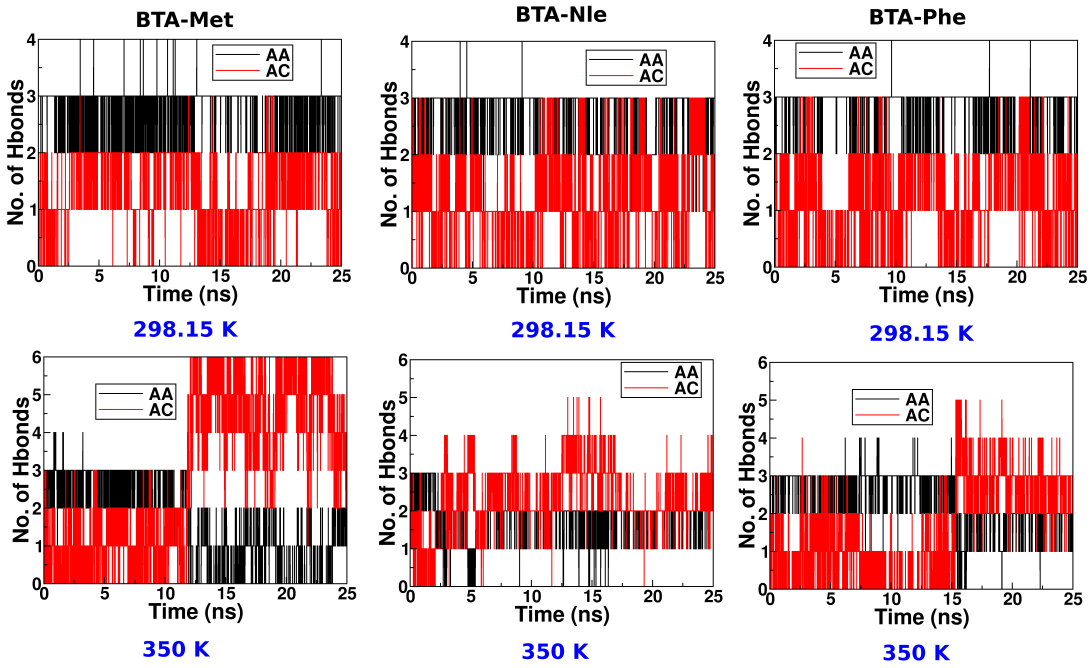

Figure 5.7: MD simulations started from an AA dimer (3 AA hydrogen bonds) configuration soaked in explicit cyclohexane solution were performed in the NPT ensemble. The number of AA and AC hydrogen bonds as a function of time for the three derivatives at 298.15 K (top panel) and 350 K (bottom panel) are shown. For BTA-Met: R'=$CH_2CH_2SCH_3$, BTA-Nle: R'=$CH_2CH_2CH_2CH_3$, BTA-Phe:R'=$CH_2C_6H_5$ and R"=dodecyl.

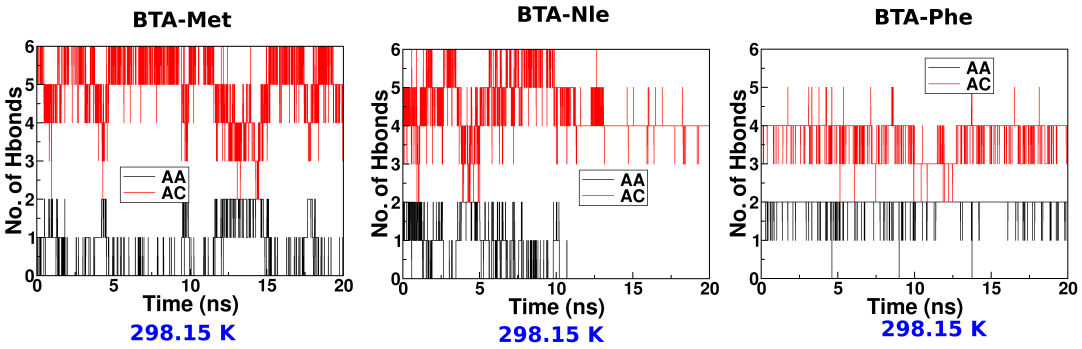

Figure 5.8: Configurations obtained from the simulations at 350 K for a AC dimer, have been cooled to 298.15 K in 2.5 ns. Further, MD simulations were extended for 20 ns at 298.15 K. For BTA-Met: R'=$CH_2CH_2SCH_3$, BTA-Nle: R'=$CH_2CH_2CH_2CH_3$, BTA-Phe:R'=$CH_2C_6H_5$ and R"=dodecyl.

simulations could be beset by sampling issues.

At 298.15 K, the AC dimer is the stable configuration for all the three derivatives with six AC H-bonds, while at 350 K, the dimer possesses a mixture of AA and AC H-bonds (total number H-bonds being six or more). Configurations obtained from the simulations of AC dimer at 350 K (possessing a mixture of AA and AC H-bonds) have been cooled to 298.15 K over 2.5 ns. MD simulations initiated from such configurations, have been run for 20 ns at 298.15 K (see Figure 5.8). The number of AC H-bonds are seen to increase, however the dimer does not completely convert to an AC type and the mean values of the number of hydrogen bonds are provided in Table 5.4.

5.3.4 Free energy simulations

Configurational free energy (ΔG_{AC}^{AA})

The stability of a AC dimer with respect to AA dimer for all the three derivatives was discussed in the previous section. Herein, we quantify the free energy difference between both the entities. Umbrella sampling technique [19] was employed to determine the relative free energies. UWHAM [20, 21] was used for post-processing to obtain free energy profiles along the reaction coordinate. Root-mean-square deviations (RMSDs) of instantaneous configurations with respect to AC dimer and AA dimer (excluding alkyl tails, see Figure 5.9) were employed as reaction coordinates (RCs) to determine the two-dimensional free energy surface. Based on unbiased MD simulations of both dimer types, we know that the RMSD of an AC dimer with respect to a AA dimer is 5.2 Å a value which is non-negligible (see Figure 5.10). Therefore, RMSD serves as a smart approach to distinguish both types of dimers. The free energy surface in the plane formed by $\mathrm{RMSD_{AC}}$ and $\mathrm{RMDS_{AA}}$ was explored. With $\mathrm{RMSD_{AC}}$ on x-axis and $\mathrm{RMSD_{AA}}$ on y-axis, the two coordinates A(0.8,5.2) and B(5.2,0.8) would correspond to AC dimer and AA dimer configurations, respectively. US simulations were carried out in 14 windows centered at different points spanning from A to B,

so as to have an optimum overlap of probability distributions (see Figure 5.11). Windows were selected along a curved path and not along the diagonal to avoid a high free energy path [27]. In any case, we were interested in only determining the free energy difference between the two dimer configurations and thus the exact path connecting the two did not matter. Simulations in each window were carried out for at least 20 ns at 298.15 K. Free energy profiles obtained using UWHAM are shown in Figure 5.12. For all the three substituents, the AC dimer is favoured over the AA dimer at 298.15 K, evidenced by the configurational free energy differences (ΔG_{AC}^{AA}) in Table 5.5.

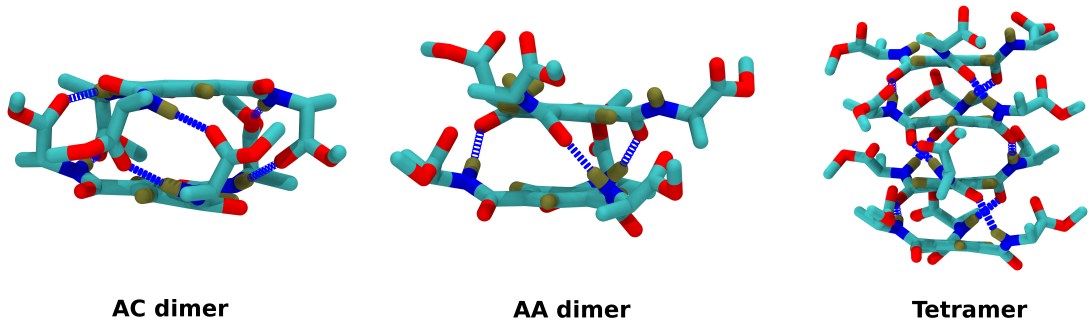

Figure 5.9: Snapshots of an AC dimer, an AA dimer and a tetramer that were considered as reference structures to determine RMSD. These structures have been chosen from the unbiased simulations carried out in explicit solution at 298.15 K.

Stability of an oligomer

As mentioned before, at ambient conditions, BTA-Met and BTA-Phe are reported in experiments [2] to self-assemble into long stacks, while BTA-Nle forms just dimers [2]. The relative free energy difference between the two dimer types-AA and AC alone cannot explain the stabilization of either long assemblies or of short dimers in the three systems studied. Thus, we have performed umbrella sampling simulations to estimate the FE difference between a tetramer and its two stable dimers. All the hydrogen bonds in a tetramer are necessarily of AA type and a pair of neighbouring molecules within it possesses hydrogen bonds of AA type. However, isolated dimers in

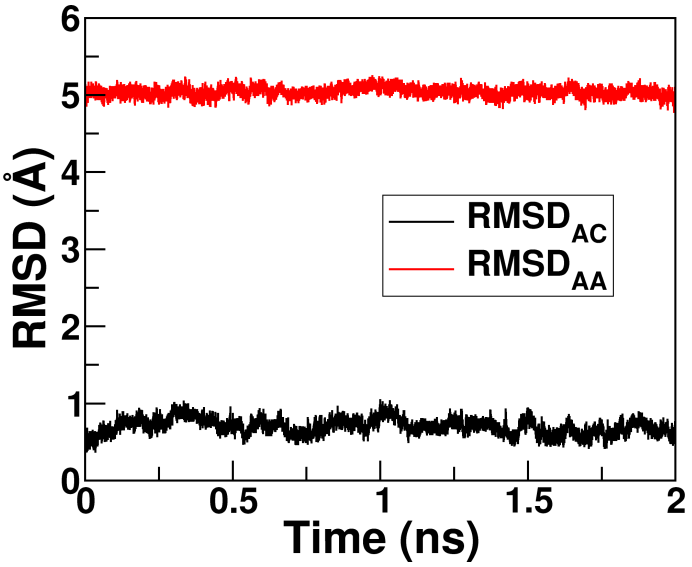

Figure 5.10: RMSD of an AC dimer with respect to an AC dimer and an AA dimer. Figure 5.9 displays the reference AC and AA dimers.

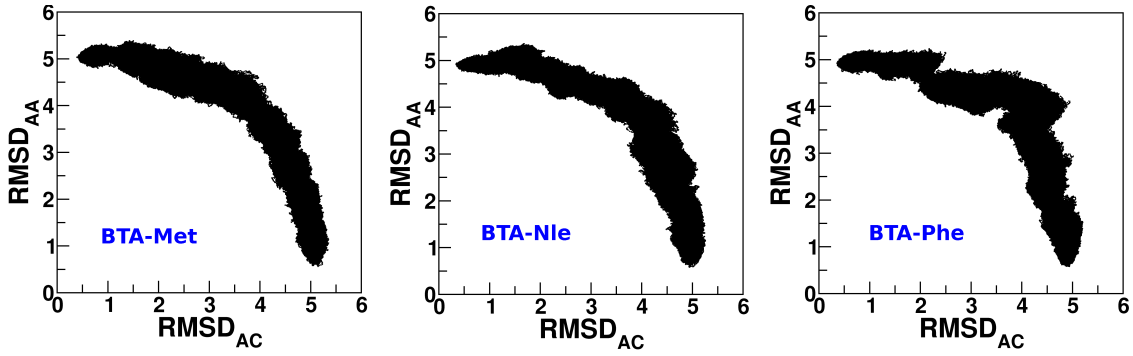

Figure 5.11: Overlap of the probability distributions along the two-dimensional reaction coordinate (Ref. Figure 5.12).

solution favour the AC configuration, as discussed earlier. Therefore, simply pulling two dimers apart from a tetramer (in which the two pairs are of AA type) does not provide us the free energy difference between a AA tetramer and two AC dimers. What we seek is the free energy difference for:

$$\underset{\text{(AA type)}}{\text{Tetramer}} \rightleftharpoons \underset{\text{(each of AC type)}}{\text{Two separated Dimers}} \tag{5.1}$$

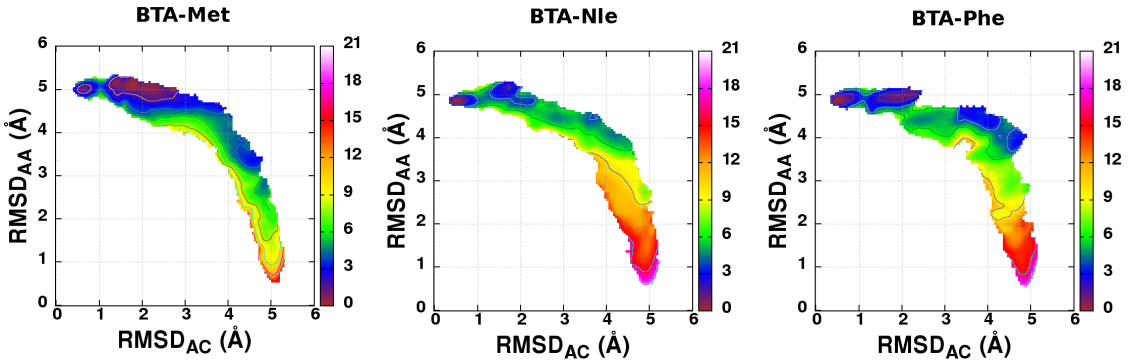

Figure 5.12: Two-dimensional free energy profiles (in kcal/mol) to estimate the free energy difference between AC and AA dimers of BTA-Met, BTA-Nle, and BTA-Phe. RMSD with respect to AC (RMSD$_{AC}$) and AA (RMSD$_{AA}$) dimer types were chosen as the two reaction coordinates. Profiles are obtained *via* umbrella sampling simulations performed in explicit cyclohexane solvent at 298.15 K.

This FE difference (ΔG^{2AC}_{4AA}) between a tetramer and its two AC dimers can be calculated in two steps, as follows:

(i) Two dimers that belong to a tetramer are pulled apart in such a way that the configurations of the resulting dimers are unaltered i.e. each dimer resembles an AA dimer throughout the pulling process. Let us call the free energy associated with this step as ΔG^{2AA}_{4AA}.

(ii) Each AA dimer is subsequently converted into AC dimer, and the free energy change (ΔG^{AC}_{AA}) associated with this step is the negative of ΔG^{AA}_{AC} which has already been determined (see Figure 5.12).

Using the above two steps, the free energy difference between a AA tetramer and two AC dimers (ΔG^{2AC}_{4AA}) can be easily determined as ΔG^{2AA}_{4AA} - 2 $\times$ ΔG^{AC}_{AA}. A scheme of this procedure is shown in Figure 5.13.

US simulations have been performed to determine the FE change between a system consisting of two independent dimers (in AA fashion) and a tetramer in cyclohexane solvent at 298.15 K. The distance between the center of mass of the two dimers was employed as a reaction coordinate. US simulations have been carried out in 30

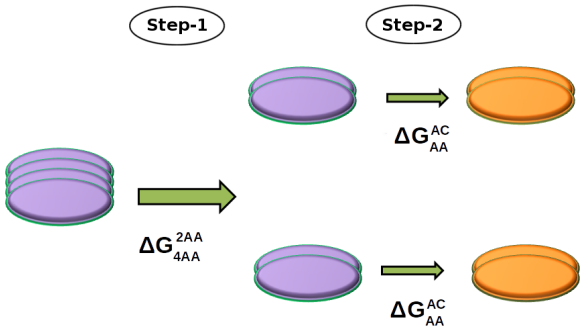

Figure 5.13: Scheme to determine the free energy difference ΔG^{2AC}_{4AA}, between a tetramer with AA hydrogen bonding and two AC dimers *via* two steps. Discs colored in violet and orange represent molecules whose hydrogen bonding pattern are in AA and AC configurations respectively. In the first step, two dimers are pulled apart from a tetramer constraining the individual dimer geometries to be of AA type. In the second step, each AA dimer is transformed to an AC dimer.

Table 5.5: Free energy changes obtained from umbrella sampling simulations are provided in the first two columns. These values are subsequently used to determine the free energy difference between a tetramer and two AC dimers (column 3). All values are in kcal/mol.

System	ΔG^{AC}_{AA}	ΔG^{2AA}_{4AA}	ΔG^{2AC}_{4AA}
BTA-Met	8.4	17.8	1.0
BTA-Nle	15.4	10.7	-20.1
BTA-Phe	15.1	14.0	-16.2

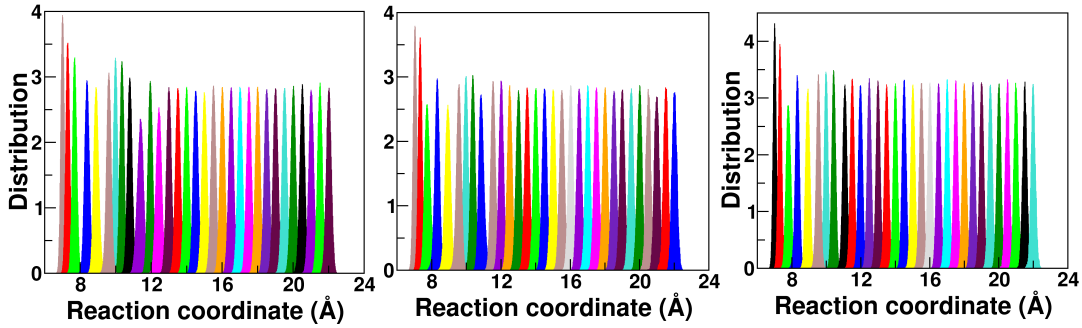

Figure 5.14: Overlap of probability distributions along the reaction coordinate (Ref. Figure 5.16).

windows for optimum overlap of probability distributions, spanning the RC value from 7.0 Å to 21.5 Å (see Figure 5.14). The geometry of the two pairs of molecules

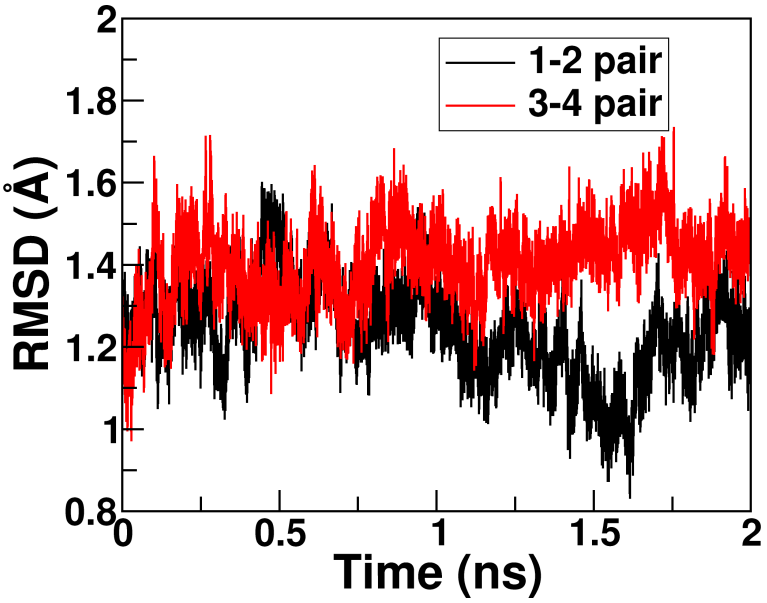

Figure 5.15: MD simulations of a tetramer in cyclohexane solution at 298.15 K. A pair of neighbouring molecules in a tetramer resembles an AA dimer. RMSD of two pair of dimers with respect to an AA dimer (see Figure 5.9).

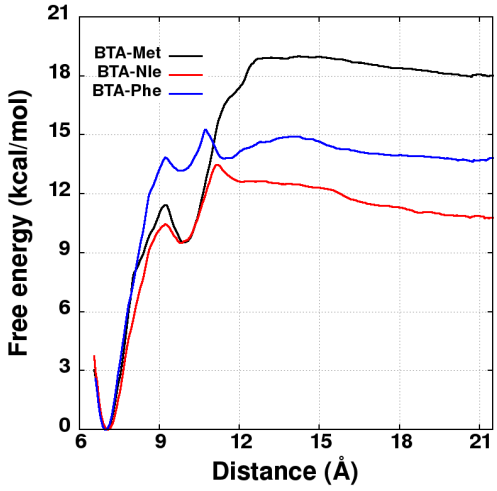

Figure 5.16: Free energy profiles associated with pulling the two dimers apart from a tetramer. Geometry of each dimer is constrained with a RMSD variable. Simulations are carried out at 298.15 K in explicit cyclohexane solvent. The oscillations in the free energy profiles are due to the reorientation of dimers during their separation (see Figure 5.17).

constituting the tetramer was restrained to a RMSD (with respect to AA dimer) value of 1.3 Å; This value was chosen based on fluctuations in the configurations exhibited by the pairs in the unbiased tetramer simulations (see Figure 5.15). Free

energy profiles were obtained using UWHAM [20, 21]. The profiles are displayed in Figure 5.16 and ΔG values determined as the difference between the free energy at the minimum and at 21.5 Å are provided in Table 5.5. The free energy profiles shown in Figure 5.16 exhibit oscillations at a reaction coordinate value of 10 Å. The dip in free energy at that distance is due to more negative potential energy, caused by a reorientation of the separating dimers (see Figure 5.17). The dimers were nearly parallel to each other until 7-8 Å, but become nearly perpendicular at around 10 Å leading to increased interaction between them which causes the dip in the free energy profile. Simulations were also performed with a restraint value of 1.5 Å. There is not much change in the free energy difference for a dimer restrained with either 1.3 Å or 1.5 Å (see Figure 5.18).

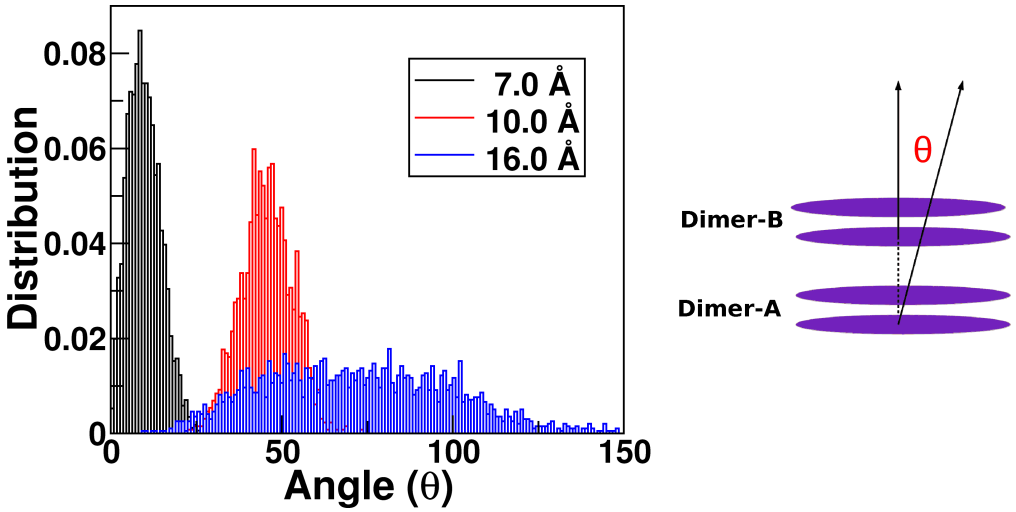

Figure 5.17: Distributions of the angle between two dimers which were pulled apart from a tetramer. Vector 1 is the vector joining the centers of mass of molecules in Dimer-A. Vector 2 is the vector joining the centers of mass of molecules in Dimer-B. θ is the angle between these two vectors.

The free energy difference between a tetramer and two AC dimers (ΔG_{4AA}^{2AC}) was determined for all the three derivatives at 298.15 K, as described in Figure 5.13. For BTA-Met, the tetramer is more stable than the two AC dimers by 1.0 kcal/mol. In contrast, the two AC dimers of BTA-Nle are stabler than a tetramer by 20.1

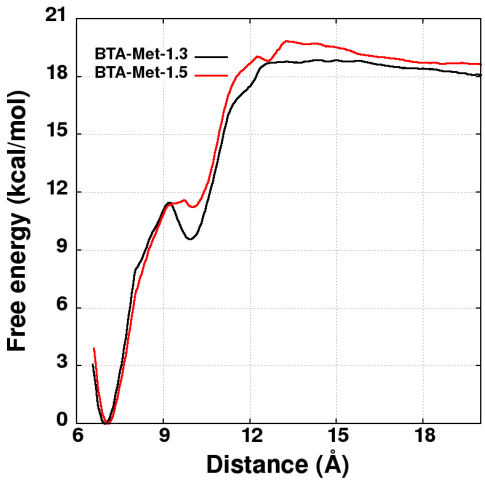

Figure 5.18: Free energy profiles associated with pulling two AA dimers apart from a AA tetramer. The geometry of each dimer is restrained with a RMSD variable.

kcal/mol. The stabilities of either an oligomer (for BTA-Met) or of a dimer (for BTA-Nle) is consistent with experimental observations [2]. However, in the case of BTA-Phe, the configuration of two independent AC dimers was found to be more stable than a tetramer (difference being -16.2 kcal/mol), while the opposite is found in experiments [2]. This can be understood as follows: there exists an additional stability imparted to the oligomers of BTA-Met and BTA-Phe due to CH$\cdots$S and CH$\cdots\pi$ hydrogen bonds, respectively as well as 1-3 interactions. Therefore, the free energy balance between the oligomer and the corresponding AC dimers shifts towards the formation of an oligomer with increase in oligomer size. Hence the free energy difference of 1.0 kcal/mol and -16.2 kcal/mol for BTA-Met and BTA-Phe, respectively increases (i.e., becomes more positive) with increasing oligomer size–favouring the oligomer formation. In the case of BTA-Phe, the AA tetramer is less stable than the configuration of two independent dimers by 16.2 kcal/mol. Thus, we explored the free energy of its hexamer to try and understand if the balance tilts towards oligomerization.

Free energy difference between a hexamer and three AC dimers

Umbrella sampling simulations have been performed to estimate the free energy difference between a hexamer with AA hydrogen bonding and three AC dimers (ΔG_{6AA}^{3AC}), for BTA-Phe.

$$\underset{\text{(AA type)}}{\text{Hexamer}} \rightleftharpoons \underset{\text{(each of AC type)}}{\text{Three separated Dimers}} \tag{5.2}$$

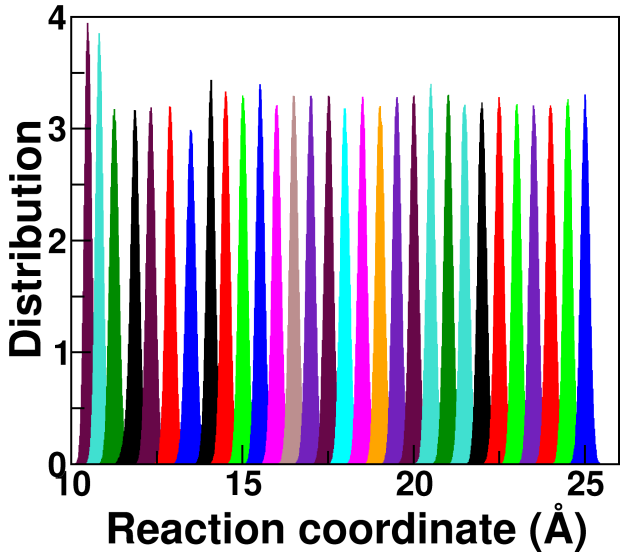

Figure 5.19: Overlap of probability distributions along the reaction coordinate (Ref. Figure 5.20).

Similar to the preceding approach, a tetramer and a AA dimer were separated from a hexamer to quantify the free energy difference (ΔG_{6AA}^{4AA+AA}) in the first step. The geometry of a tetramer and of a dimer constituting the hexamer were restrained to a RMSD value of 1.3 Å. The distance between the center of mass of the tetramer and center of mass of the dimer was chosen to be the reaction coordinate. Two styles 'distanceZ' and 'distanceXY' of colvars module were used to determine the free profiles. 'DistanceZ' style was employed to determine the free energy profile along the reaction coordinate. 'DistanceXY' was used to restrain the dimer coaxially

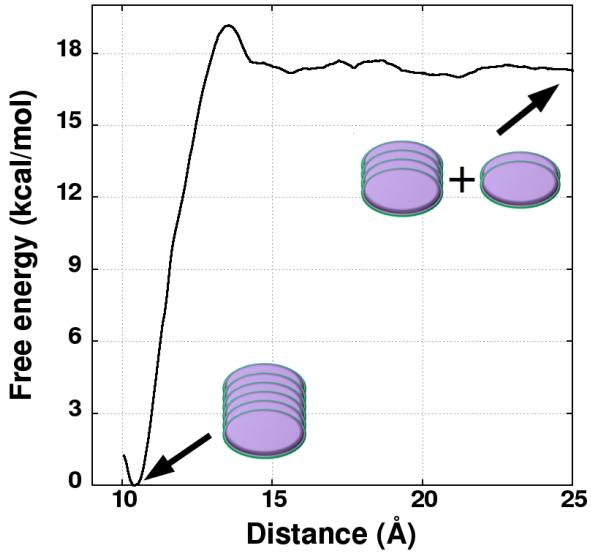

Figure 5.20: Free energy profile associated with pulling a AA tetramer and a AA dimer apart from the AA hexamer. Geometry of tetramer and dimer is constrained with a RMSD variable. Simulations are carried out at 298.15 K in explicit cyclohexane solvent.

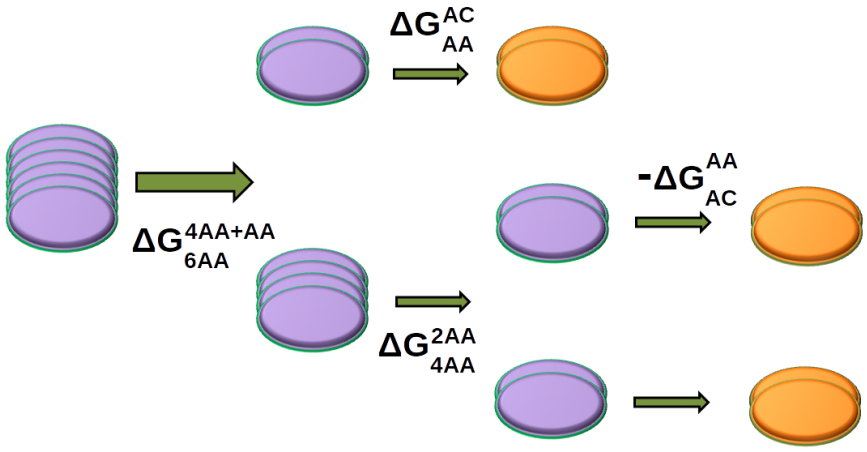

Figure 5.21: Scheme to determine the free energy difference ΔG_{6AA}^{3AC}, between a hexamer with AA hydrogen bonding and three AC dimers.

along the tetramer. Umbrella sampling simulations were performed in 30 windows spanning from 10.5 Å to 25.0 Å. Overlap of probability distributions along the RC is displayed in Figure 5.19. The profile is shown in Figure 5.20 with ΔG_{6AA}^{4AA+AC}

being 17.3 kcal/mol. Using a Born-Haber cycle approach, the free energy difference between a hexamer and its three AC dimers can be estimated as shown in Figure 5.21 and evaluated as

$$\Delta G_{6AA}^{3AC} = \Delta G_{6AA}^{4AA+AC} + \Delta G_{4AA}^{2AA} - 3 \times \Delta G_{AA}^{AC}$$

Substituting the values in the above expression, we obtain ΔG_{6AA}^{3AC} to be -14 kcal/mol. Although the value favours the formation of three AC dimers over a hexamer, the difference in free energy of the oligomer and its AC dimers decreased by 2 kcal/mol (from tetramer to hexamer). This clearly demonstrates that the formation of an oligomer can become more facile for longer oligomers of BTA-Phe.

5.4 Conclusions

In amino ester-based benzene-1,3,5-tricarboxamide, two variants of dimer configurations are possible which are differentiated based on their hydrogen bonding patterns. An AA dimer is one in which hydrogen bonds are formed between amide groups, similar to typical alkyl derivatized BTA stacks [28]. In contrast, an AC dimer is formed *via* hydrogen bonds between amide and carboxylate groups. The latter is more stable than the AA dimer by $\approx$ 20 kcal/mol at zero Kelvin, for molecules in gas phase, with short tails. The face-to-face dimerization of two molecules leads to the formation of an AC dimer, which precludes further elongation to form oligomers. The AC dimer configuration is a capsule. Thus, pairs of molecules with only amide-amide hydrogen bonding can lead to the formation of an oligomer.

Following recent experiments [2], the self-assembly of three derivatives of amino ester-based BTA (Met, Nle, Phe) have been studied at finite temperature in explicit cyclohexane solvent. BTA-Met and BTA-Phe were reported to exist as long assemblies, while BTA-Nle forms dimers at ambient conditions. Assemblies of BTA-Met and BTA-Phe are stabilized by weak CH$\cdots$S and CH$\cdots\pi$ hydrogen bonds, respectively. Also, the structure of a dimer at 298.15 K is different from the structure at 350 K. At higher temperatures, the dimers possess a mixture of AA and AC hyrdogen bonding

types, whereas at ambient conditions, they consist of only AC H-bonds.

Umbrella sampling simulations have been performed to quantify the free energy difference between the two variants of dimer species. Additionally, such simulations have also been carried out to estimate the free energy difference between an oligomer and its corresponding stable dimers (AC ones). The results convincingly shown for BTA-Met, and evidence is provided for BTA-Phe having stable oligomers. The present study uncovers the structural aspects of amino ester-based BTAs for three substituents. The approach presented here can guide experimentalists in the choice of substituents to control self-assembled structures.

Bibliography

[1] Gong, B.; Zheng, C.; Yan, Y. *J. Chem. Crystallogr. 29*, 649–652.

[2] Desmarchelier, A.; Raynal, M.; Brocorens, P.; Vanthuyne, N.; Bouteiller, L. *Chem. Commun.* **2015**, *51*, 7397–7400.

[3] Plimpton, S. *J. Comput. Phys.* **1995**, *117*, 1–19.

[4] Mayo, S. L.; Olafson, B. D.; Goddard, W. A. *J. Phys. Chem.* **1990**, *94*, 8897–8909.

[5] Gasteiger, J.; Marsili, M. *Tetrahedron* **1980**, *36*, 3219–3228.

[6] Keasler, S. J.; Charan, S. M.; Wick, C. D.; Economou, I. G.; Siepmann, J. I. *J. Phys. Chem. B* **2012**, *116*, 11234–11246.

[7] Nosé, S. *J. Chem. Phys.* **1984**, *81*, 511–519.

[8] Hoover, W. G. *Phys. Rev. A* **1985**, *31*, 1695–1697.

[9] Humphrey, W.; Dalke, A.; Schulten, K. *J. Molec. Graphics* **1996**, *14*, 33–38.

[10] Kulkarni, C.; Reddy, S. K.; George, S. J.; Balasubramanian, S. *Chem. Phys. Lett.* **2011**, *515*, 226–230.

[11] Panigrahi, S. K.; Desiraju, G. R. *Proteins: Structure, Function, and Bioinformatics* **2007**, *67*, 128–141.

[12] Zhou, P.; Tian, F.; Lv, F.; Shang, Z. *Proteins: Structure, Function, and Bioinformatics* **2009**, *76*, 151–163.

[13] Frisch, M. J.; *et al.*, Gaussian 09 Revision D.01. Gaussian Inc. Wallingford CT 2009.

[14] Hutter, J.; Iannuzzi, M.; Schiffmann, F.; VandeVondele, J. *Wiley Interdiscip. Rev.: Comput. Mol. Sci.* **2014**, *4*, 15–25.

[15] Elstner, M.; Porezag, D.; Jungnickel, G.; Elsner, J.; Haugk, M.; Frauenheim, T.; Suhai, S.; Seifert, G. *Phys. Rev. B* **1998**, *58*, 7260–7268.

[16] Perdew, J. P.; Burke, K.; Ernzerhof, M. *Phys. Rev. Lett.* **1996**, *77*, 3865–3868.

[17] Grimme, S.; Antony, J.; Ehrlich, S.; Krieg, H. *J. Chem. Phys.* **2010**, *132*.

[18] Fiorin, G.; Klein, M.; Hénin, J. *Mol. Phys.* **2013**, *111*, 3345–3362.

[19] Torrie, G.; Valleau, J. *J. Comput. Phys.* **1977**, *23*, 187–199.

[20] Tan, Z.; Gallicchio, E.; Lapelosa, M.; Levy, R. M. *J. Chem. Phys.* **2012**, *136*.

[21] Tan, Z.; Gallicchio, E. UWHAM: Unbinned weighted histogram analysis method. 2012; R package version 1.0.

[22] Krepps, M. K.; Parkin, S.; ; Atwood, D. A. *Crystal Growth & Design* **2001**, *1*, 291–297.

[23] Gregoret, L. M.; Rader, S. D.; Fletterick, R. J.; Cohen, F. E. *Proteins: Structure, Function, and Bioinformatics* **1991**, *9*, 99–107.

[24] Brandl, M.; Weiss, M. S.; Jabs, A.; Sühnel, J.; Hilgenfeld, R. *J. Mol. Biol.* **2001**, *307*, 357–377.

[25] Harigai, M.; Kataoka, M.; Imamoto, Y. *J. Am. Chem. Soc.* **2006**, *128*, 10646–10647.

[26] Nishio, M. *Phys. Chem. Chem. Phys.* **2011**, *13*, 13873–13900.

[27] To restrain along the diagonal, high force constant was needed especially at (2.5,2.5).

[28] Bejagam, K. K.; Fiorin, G.; Klein, M. L.; Balasubramanian, S. *J. Phys. Chem. B* **2014**, *118*, 5218–5228.

Chapter 6

Dipole-Moment Driven Cooperative Supramolecular Polymerization

6.1 Introduction

The mechanism of one-dimensional self-assembly of molecules into supramolecular polymers can be broadly classified into two types: isodesmic and cooperative (Chapter 1). In the former, the association constant is the same during all the steps of polymerization, while in the latter, it shows a dependence on the oligomer size. The investigation into the mechanism of supramolecular polymerization has gained importance in the past decade to allow for a better control over its structure and functions [1–3]. Electronic, structural, and hydrophobic interactions have been suggested as the cause of cooperativity in supramolecular polymers [4]. Yet, a comprehensive rationale for the observed mechanisms of polymerization based on

Reprinted with permission from "Dipole Moment Driven Cooperative Supramolecular Polymerization," *J. Am. Chem. Soc.* **2015**, 137, 3924-3932. Copyright 2015, American Chemical Society. http://pubs.acs.org/doi/abs/10.1021/jacs.5b00504. All experiments were carried out by Dr. Chidambar Kulkarni.

structural motifs in the monomer is lacking. It has earlier been conjectured that the presence of molecular motifs that give rise to long-range interactions along the stacking direction leads to cooperative growth and lack of such interactions results in isodesmicity [5]. Towards this, we have studied three perylene based derivatives bearing various combinations of linkers and self-assembling moieties.

Perylene-3,4,9,10-tetracarboxylic acid bisimides (PBIs) are well-known electron-deficient organic semiconductors and have been widely employed as active materials in organic electronics [6]. PBI derivatives are known to follow an isodesmic mechanism of self-assembly [7, 8]. However, there are only a few reports on the cooperative self-assembly of PBIs; these are mainly driven by either intermolecular hydrogen bonding or intramolecular hydrogen bonding together with π-stacking [9, 10].

In the present chapter, we investigate the effect of various linker groups and self-assembling moieties attached to the PBI chromophore on the mechanism of self-assembly. These PBI derivatives have been synthesized in the research group of Prof. Subi George at JNCASR. Structures of these molecules are shown in Figure 6.1. Molecule **1** consists of a carbonate dipolar linker and rigid cholesterol as self-assembling moiety. Molecule **2** is same as molecule **1** with ether replacing the ester linker. Molecule **3** possesses carbonate linker along with chiral swallowtail as the self-assembling moiety. Experimental studies reveal that molecule **1** grows in a cooperative pathway, whereas, molecules **2** & **3** follow an isodesmic mechanism (see Figure 6.2). The shape of the cooling curves indicate the self-assembling mechanism (see Chapter 1). Substitution of a cholesterol with chiral swallowtail transforms the self-assembly mechanism from cooperative to isodesmic growth. Also, replacing the dipolar carbonate group with ether too causes a similar change in mechanism.

Molecular Dynamics (MD) simulations have been performed to gain insights into the assembled structures and explain the collective role played by the linker and self-assembling moieties in imparting cooperativity in the self-assembly. Herein, we show that dipole-dipole interaction between molecules along the stacking direction is

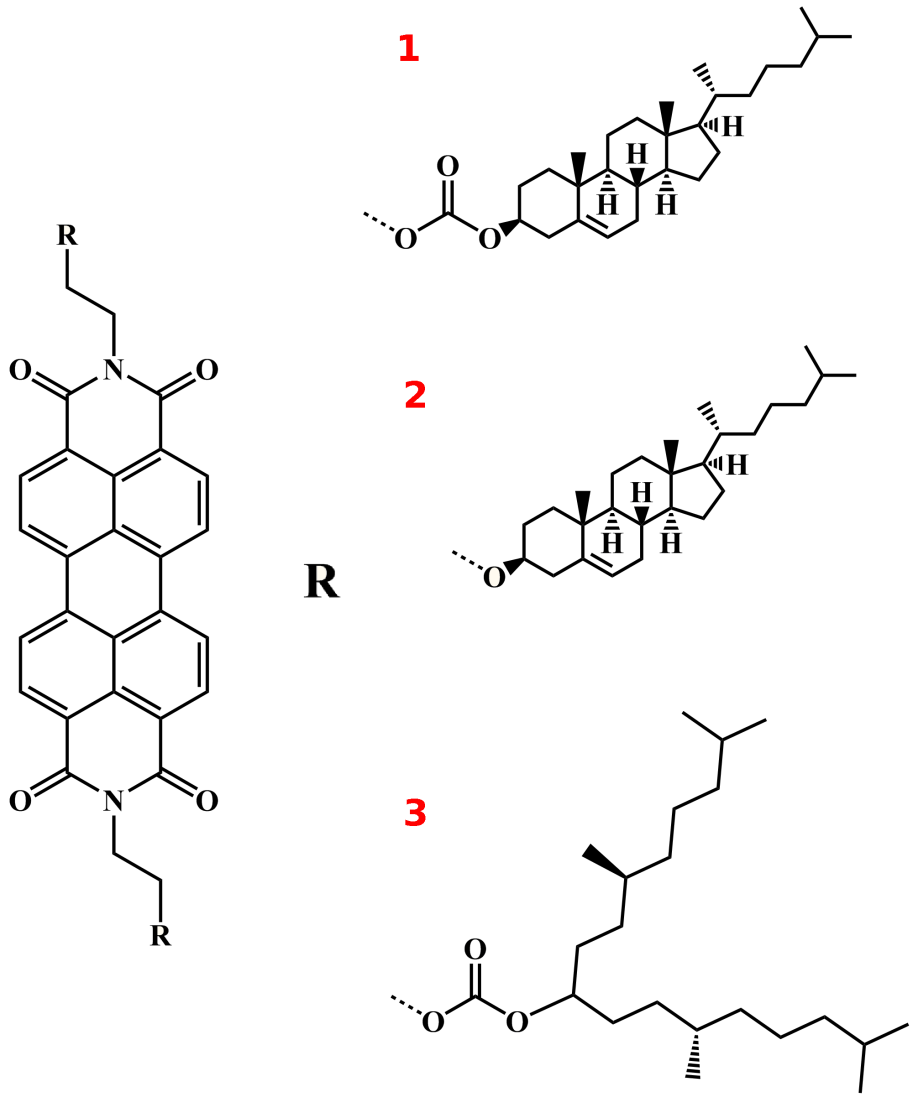

Figure 6.1: PBI is functionalized on both imide nitrogens with either carbonate (**1** and **3**) or ether linker (**2**). Cholesterol (**1** and **2**) or chiral swallowtail (**3**) are used as self-assembling motifs.

the primary cause of cooperativity. The interaction is shown to arise from the dipolar nature of carbonate linkers and the rigidity of cholesterol self-assembling moieties. Thus, we present a unique example of non-hydrogen-bonded and dipole-moment-driven cooperativity in a supramolecular system.

6.2 Computational studies

Similar to BTA molecules in the previous chapters, PBI molecules also were modelled using DREIDING [12] force field with gasteiger [13] charges on atomic sites.

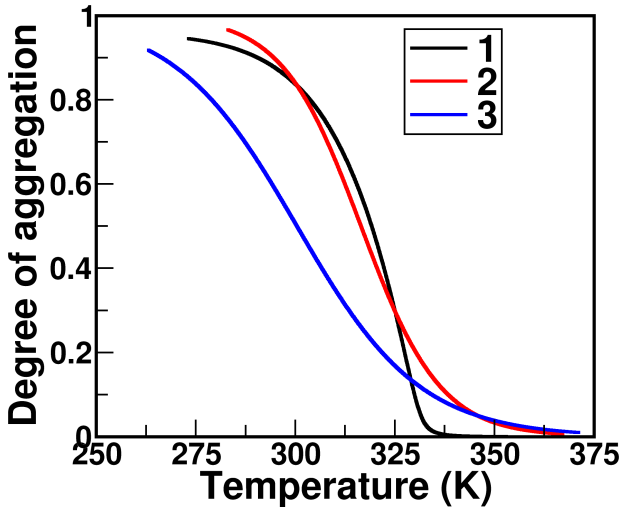

Figure 6.2: Degree of aggregation as a function of temperature for all three derivatives obtained experimentally from spectroscopic studies. System **1** shows a cooperative growth, while systems **2** & **3** exhibit an isodesmic mechanism of self-assembly. Details of experiment are provided in Ref. [11].

Cyclohexane (solvent) molecules were represented within a united atom approach using TraPPE [14] parameters. Cross interactions between PBI and solvent molecules were handled using DREIDING's mixing rules. MD simulations were carried out using LAMMPS [15] package in the canonical (NVT) ensemble. Temperature of the system was maintained at 298.15 K using Nosé-Hoover thermostat [16, 17] with a coupling constant of 1 ps. Time step of 0.5 fs and periodic boundary conditions were employed for all simulations. Real space interactions were truncated at 12 Å and long-range Coulombic interactions were evaluated using particle-particle particle-mesh (PPPM) solver.

Table 6.1: Details of the system sizes that are considered for the pre-formed bulk simulations at 298.15 K.

System	**1**	**2**	**3**
No. of PBI molecules	40	40	40
No. of cyclohexane molecules	45521	45674	45631
Total no. of atoms	281206	281884	281226

6.3 Results and Discussion

6.3.1 Conformers of PBI

PBI has a planar core with its two arms being out of plane. (i) Boat, in which the two arms project out in the same direction with respect to the core, and (ii) chair, with the arms oriented in opposite directions with respect to the core are the two conformers of PBI as shown in Figure 6.3. To predict their relative stability, we have geometry optimized oligomers constructed using both units within the force field approach. Energies of the dimer and trimer in gas-phase are comparable but a drastic difference in energy is seen for the tetramer (Table 6.2). Clearly, the chair conformer is preferred over the boat during oligomerization.

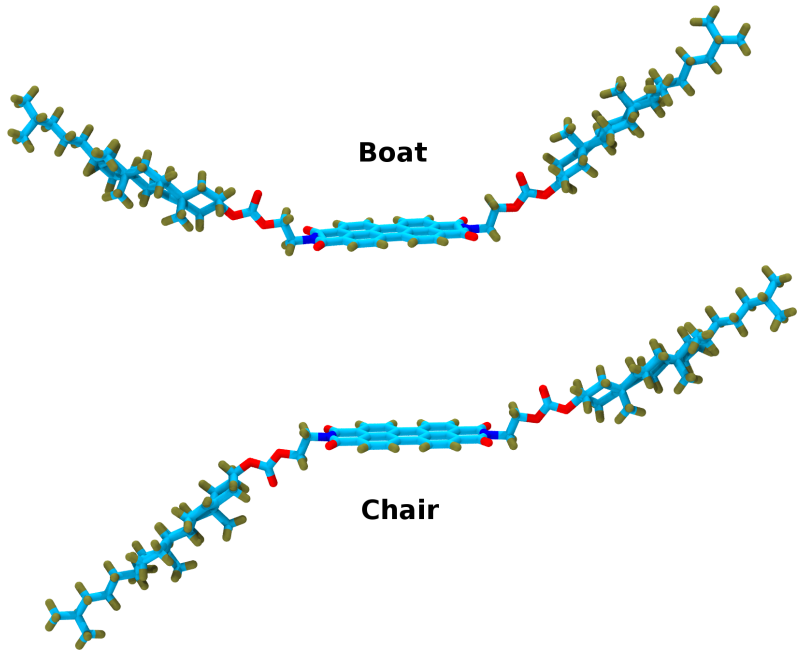

Figure 6.3: Snapshot showing two conformers of **1**. Both the substituents on the imide nitrogen are on the same (Top) or on either side (Bottom) side of the PBI core.

6.3.2 Construction of an oligomer

In an oligomer, PBI molecules are π-stacked and rotated with respect to each other along the molecular axis. Molecular axis is the line joining the two nitrogens of the PBI core (see Figure 6.1). The angle between the molecular axis of two neighboring

Table 6.2: Difference in energies between two conformers of PBI (E_{boat}- E_{chair}) in kcal/mol attached with different self-assembling moieties, calculated using force field.

Oligomer	**1**	**2**	**3**
Monomer	0.04	0.80	-1.07
Dimer	4.90	-1.48	-0.28
Trimer	4.61	-1.53	4.14
Tetramer	14.77	15.49	22.61

PBI molecules in the stack is denoted by β. Minimization of the dimer with different starting values of β may end up in different local minima. MD simulations of a dimer initiated with β value of either 30° or 60° converge to the same value around 28° (see Figure 6.4). This is in agreement with β values reported in literature obtained *via* gas-phase quantum chemical calculations [18–20]. Figure 6.5 shows the dimer started with a β value of 60° which converge around 28°. We have constructed the oligomers of three compounds, each with an initial $\pi - \pi$ distance of 3.7 Å and β of 26° (26° was chosen over 28° to avoid hard contact of tails). Gas-phase MD simulations of oligomers of **1**, **2**, and **3** were performed to know the stability of such an oligomers at low temperature. All the π contacts are intact throughout the simulations which implies that the initial structures are reasonable.

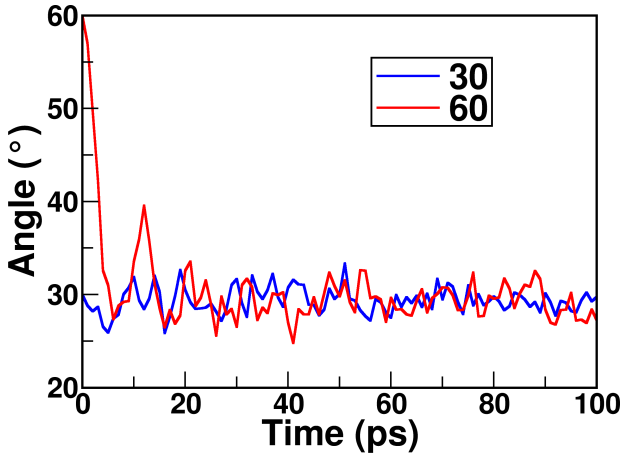

Figure 6.4: Evolution of β, from MD simulations of a dimer of **1** initiated from two different values, as a function of time.

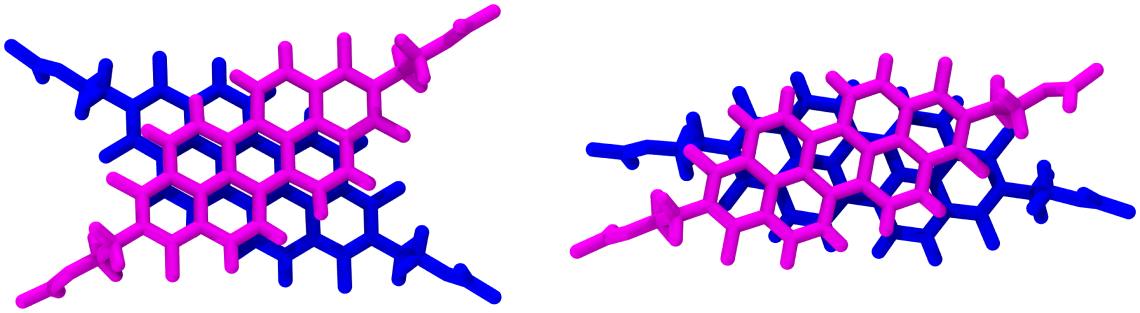

Figure 6.5: Molecular axis for each PBI molecule is defined as the vector joining the nitrogen atoms in the core. Two molecules are represented in two different colors (a) Initial configuration of PBI molecules starting with an angle (β) of 60° between the molecular axis. (b) Snapshot of the dimer, post MD simulation, when the angle converges to around 28°.

6.3.3 Gas-phase MD simulation and macrodipole

Before starting realistic simulations in solvent phase at ambient conditions, we carried out MD simulations at 5 K to check the stability of the oligomers constructed. Simulations of pre-formed hexamer were carried out to evaluate the dipole moment along the stacking direction for oligomers of **1**, **2** and **3**. The macrodipole moment along the stacking direction for each of these systems over the last 1 ns of trajectory is shown in Figure 6.6. Noticeably, the hexamer formed with **1** possesses a larger dipole moment compared to other hexamer units. The final structure obtained from MD was used as input to calculate semiempirical PM6 charges using Gaussian 09 [21]. The macrodipole moment of a hexamer of **1** is 9.46 D while that of **3** is merely 1.5 D. Using charges of the force field, the macrodipole moment of various optimized oligomers was determined and the same are provided in Table 6.3. With increase in oligomer size, the macrodipole moment of **1** increases more compared to those of either **2** or **3**.

6.3.4 Finite temperature MD simulations in solution

Simulations of pre-formed oligomeric stacks, each containing 40 molecules of **1**, **2**, and **3** were performed in explicit cyclohexane at 298.15 K for 20 ns. All the analysis were performed on the last 12 ns of the MD trajectory. Snapshots at the end of the

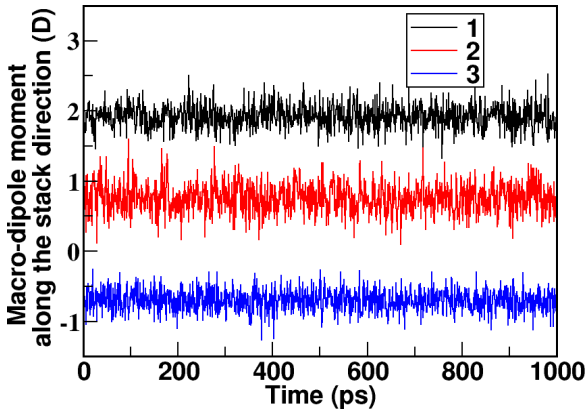

Figure 6.6: Macrodipole moment along the stacking direction for hexamers of the three molecules obtained using gas phase MD simulations carried out at 5 K.

Table 6.3: Macrodipole moment (in Debye) determined using Gasteiger charges for various optimized oligomers of **1, 2** and **3** in gas phase.

Oligomer	**1**	**2**	**3**
Monomer	0.3	0.48	0.02
Dimer	0.6	0.38	0.00
Trimer	1.52	0.34	0.02
Tetramer	1.81	0.52	0.54
hexamer	1.97	0.93	0.73

MD simulations for cholesterol appended molecules **1** and **2** exhibit helical packing of linker groups (carbonate or ether) around the PBI core (Figure 6.7). This, in turn, is reflected in the ordered helical organization of the peripheral cholesterol groups and PBI core, in agreement with the experimental observation of bisignated CD signal. On the other hand, the organization of linker groups (carbonate) in the assembly of **3** is ill-defined (Figure 6.7) which can be attributed to the flexibility of the chiral swallowtail. Coincidentally, chiral organization in **3** is experimentally determined to be absent as well. The arrangement of linkers in the assembly can be further quantified by the distance between them across neighboring molecules in an assembly (Figure 6.8). Assemblies of **1** and **3** exhibit a bimodal distribution of interlinker (carbonate) distances, centered at 5.5 Å and 9 Å. For **1**, the intensity at 5.5 Å is larger than at 8.9 Å suggesting that the majority of carbonate groups

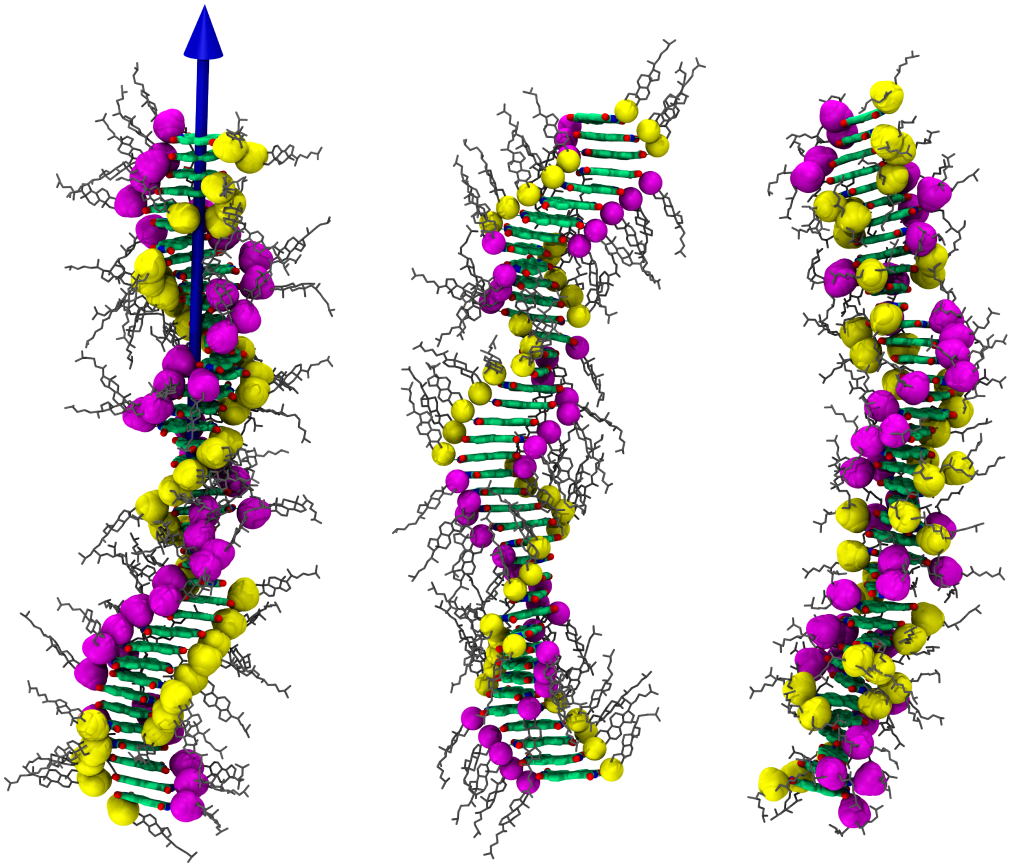

Figure 6.7: Snapshot illustrating the arrangement of molecules in the assembled state. Linkers are highlighted in yellow and magenta to aid in the visualization of the helical packing. Self-assembling groups are represented with thin sticks, and hydrogens are omitted for clarity.

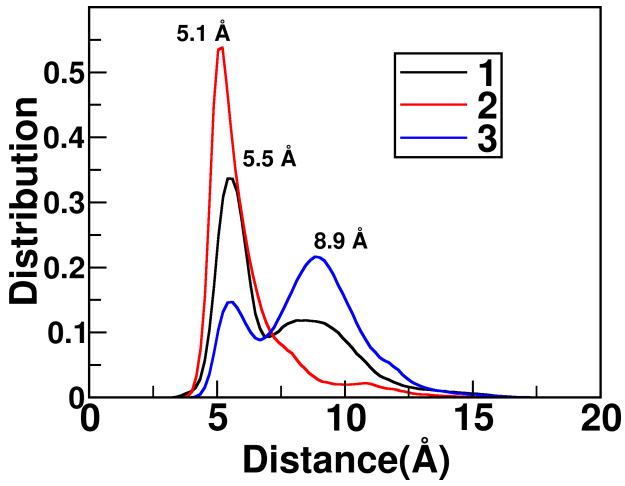

Figure 6.8: Distance distribution between the linkers of neighboring molecules.

are more closely arranged in an assembly of **1** compared to that of **3**. A unimodal probability distribution centered at 5.1 Å is observed for the assembly of **2** (ether linker), suggesting close and uniform packing of linkers.

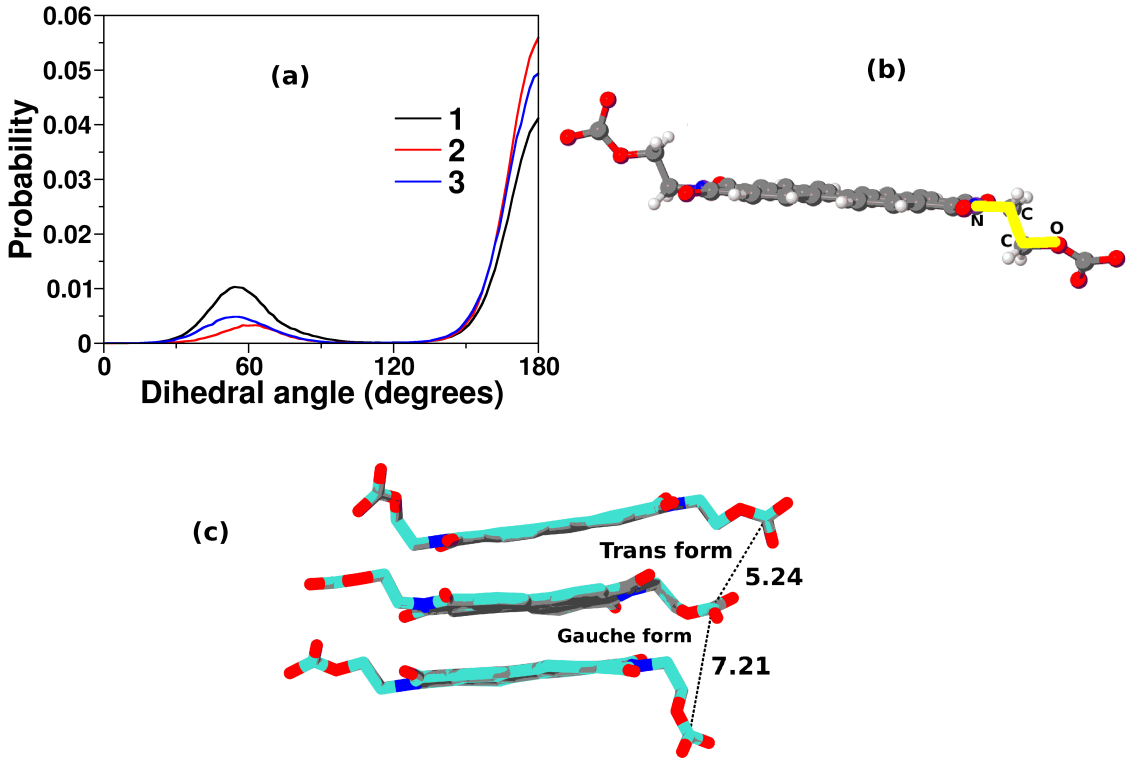

Figure 6.9: (a) Distribution of the dihedral angle, averaged over all molecules in the core of the assembly at 298.15 K for **1**, **2** and **3**. (b) Dihedral angle (N-C-C-O) under consideration. (c) Snapshot from an assembly of **1**, illustrating the gauche and trans forms and corresponding linker distances (in Å) (lower panel) . The bimodal distribution of the torisonal angle contributed to the observed distribution of linker distances presented in Figure 6.8.

Origin of the bimodal distribution of linker distances

Torsional distributions about the N-C-C-O middle bond (see Figure 6.9b) for the three oligomers in solution under ambient conditions are shown in Figure 6.9a. The taller peak arises from trans conformation while the shorter one is from gauche defects. The percentage of gauche defects is more in the oligomer of **1** (52%) compared to that in 2 (12%) and 3 (20%). Gauche and trans conformations of this bond are the leading contributors to the bimodal nature of the distribution of linker distances in **1** and **3**

(Figure 6.9c). Absence of the bimodal distribution in an assembly of **2** is clearly due to the lesser amount of gauche defects. Additionally, the angle between the molecular axis in an assembly (β), also shows a bimodal distribution (Figure 6.10). This too could likely contribute to the bimodal distribution of linker distances (Figure 6.8).

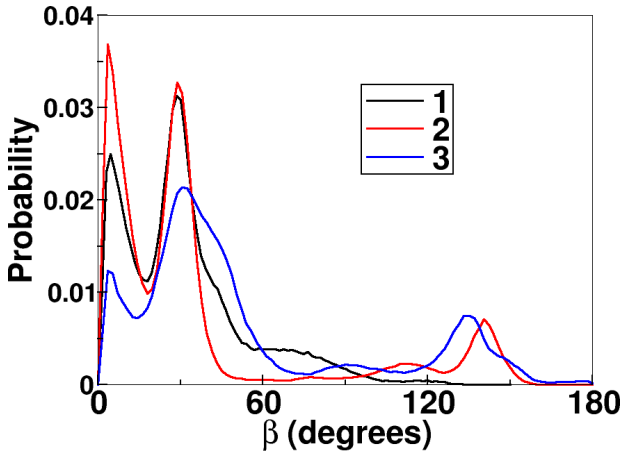

Figure 6.10: β angle distribution for the inner 30 molecules of the oligomer at 298.15 K analysed over the last 20 ns. The bimodal distribution of β contributes to the observed distribution of linker distances presented in Figure 6.8.

Macrodipole moment

The consequence of structural organization of linkers on the macrodipole moment (along the stacking direction) is studied during the MD trajectory (Figure 6.11). Macrodipole is calculated as $\Sigma q_i \times \vec{r}_i$, where q_i is the charge on the atoms and $\vec{r}_i$ the displacement vector from negative to positive charge, respectively, and the sum extends over all atoms. The mean macrodipole moment for **1** (14.7 D) is an order of magnitude higher than that for **3** (1.43 D), although in both molecules (**1** and **3**), the carbonate linker is the dipolar entity.

Orientation of dipole moment vector of individual molecules

We now study the orientation of the dipole moment of a molecule. In order to eliminate edge effects, we discard contributions from five molecules present at either end of the stack in further analysis. Macrodipole moment of the entire system was obtained as the sum of dipole moment of each molecule in a given oligomeric structure.

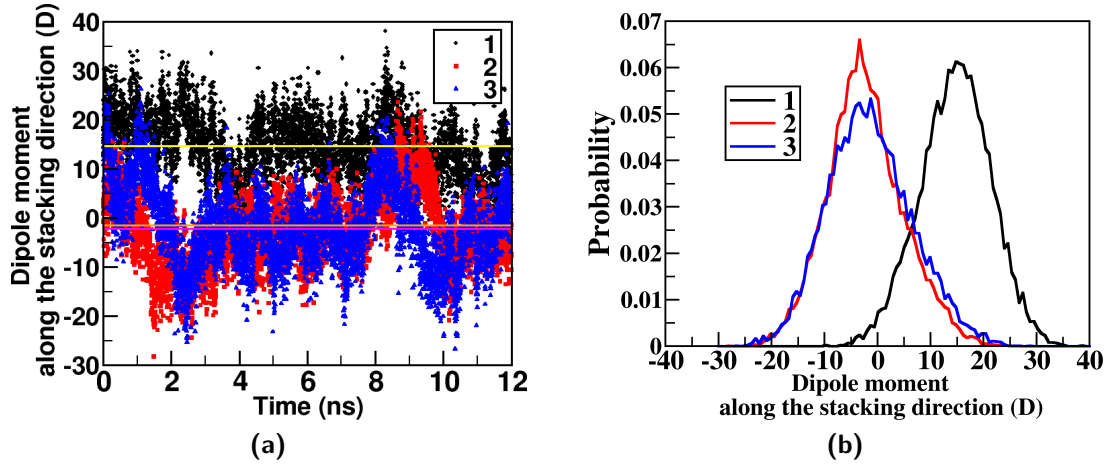

Figure 6.11: (a) Macrodipole moment along the stacking direction as a function of time. Solid horizontal lines (yellow for **1**, magenta for **2**, and orange for **3**) are drawn to represent the mean dipole moment value for each system. (b) Normalized histogram of macrodipole moment obtained from (a).

Distribution of these individual dipole moment vectors (μ) of each molecule with respect to the normal to the PBI plane is shown in Figure 6.12 and the actual dipole vectors are displayed in Figure 6.13. For **2** and **3**, the distribution is nearly symmetric about zero (Figure 6.12), implying that parallel and antiparallel orientations of molecular dipoles are equally likely which does not lead to any significant macrodipole for the stack. In contrast, in the assembly of **1**, the carbonate linkers on each branch of the molecules are better aligned with each other; however, the net dipole from each of these branches, although in opposite directions, do not cancel fully. This results in a net macrodipole moment for a stack of **1** (Figure 6.11a). Thus, the difference in the macrodipole moment between **1** and **3** can be mainly attributed to the organization of the linkers.

Inclination of the carbonate group

As the carbonate linker is dominant in imparting a dipole moment for the molecule, it is important to examine the carbonate orientations along the stack. Herein, we defined a vector along the C=O axis and determined the angle it made with the normal of the PBI plane. In an oligomer, all the carbonate linkers along one arm are

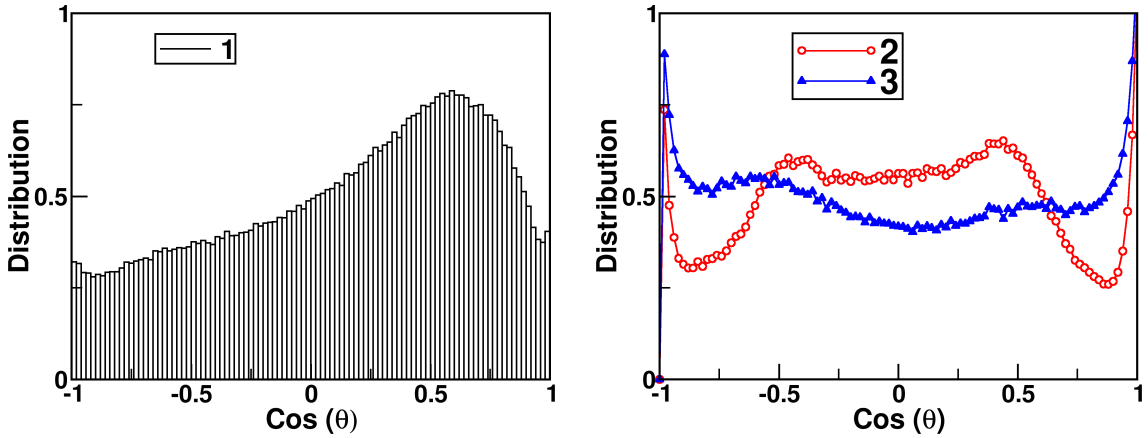

Figure 6.12: Distribution of the cosine of the angle between the dipole moment of each molecule (μ) with the normal to the PBI plane (n).

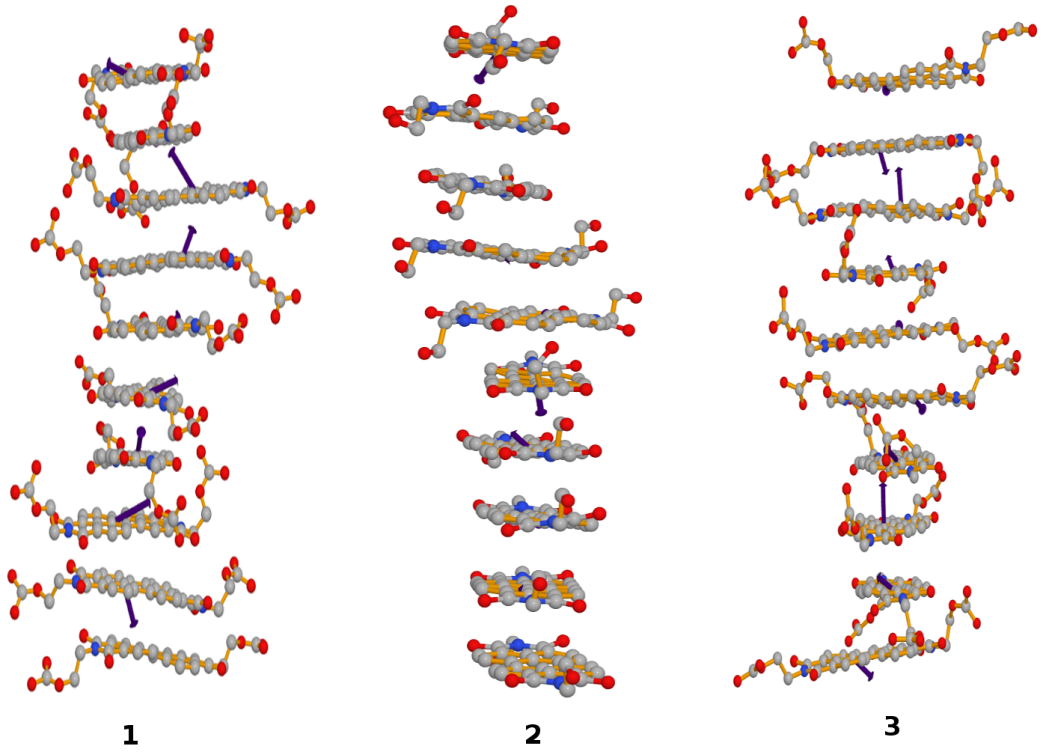

Figure 6.13: Snapshot showing dipole moment vectors of each molecule in stacks of **1**, **2** and **3**. Only ten molecules present in the core of each stack is shown for clarity. Periphery groups are not shown for clarity. Dipole vectors are denoted with thick violet arrows.

referred as helix A and on the other as helix B. Figure 6.14 and Figure 6.15 show the distributions of angle between C=O vector and the normal of PBI plane for each

helix in the stack and for entire oligomer respectively. The average of the inclination angle of carbonate vector can be taken as an order parameter for structural ordering. This quantity averaged over the core 30 molecules for **1** and **3** is 0.149 and 0.005, respectively, clearly suggesting the ordered arrangement of molecules in the former over the latter. Thus, the differences in the structural organization can be attributed to the rigidity or flexibility of the self-assembling moiety. For **1**, the probability of finding the C=O vectors making an angle close to 0° is more compared to that for an angle of 180°. As a result, a net dipole moment ensues along the stack direction for **1**. On the other hand, the distribution of C=O vector orientation with respect to PBI core normal in a stack of **3** is symmetric, enabling only a weak macrodipole moment for **3**.

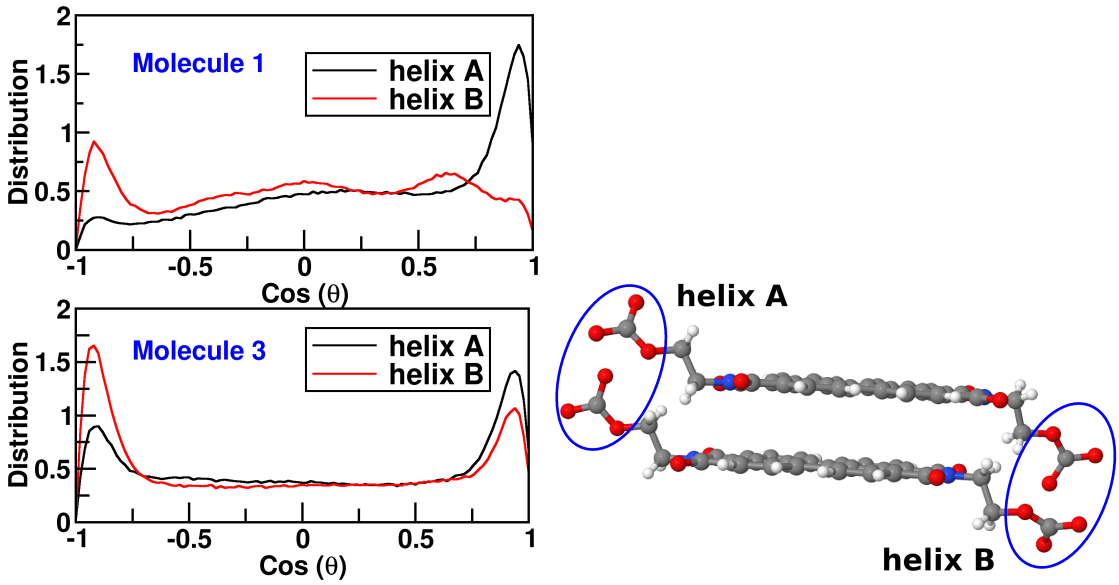

Figure 6.14: Distribution of the angle between the C=O vectors of an arm of a molecule which is part of either of the two helices, with the normal of PBI plane in **1** and **3**. The right panel shows the definition of helix A and helix B.

In an oligomer of **1**, the distribution of carbonate orientations are different in the two helices which contributes to the net macrodipole in stack of **1**. From a molecular point of view, both the helices are identical; what makes the macrodipole to prefer one helix over the other? In order to figure out the cause, we examined configurations

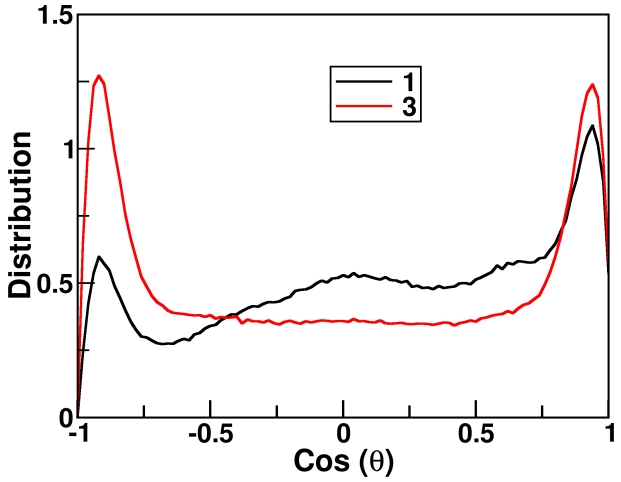

Figure 6.15: Total number of C=O vectors, in two helices, as a function of inclination angle to the normal of PBI plane for oligomers of **1** and **3**.

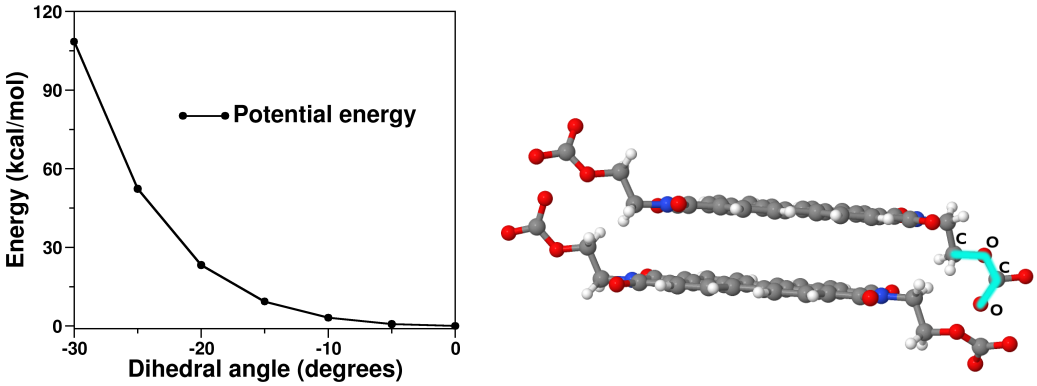

Figure 6.16: Potential energy scan of C-O-C=O dihedral angle of a dimer of **1** at B3LYP/6-31g level of theory. Dihedral angle of zero corresponds to the configuration when the carbonate dipoles are not aligned. Right panel depicts the dihedral angle scanned.

of a hexamer simulated in gas phase at 5 K. Astonishingly, the self-assembling moieties and carbonate linkers in each helix are packed in different manners. In helix B, cholesterols are closely packed, accompanied with random orientations of C=O dipoles in it; however, in helix A, the C=O dipoles are aligned parallel to each other and cholesterols spaced at optimal distance. There is a competition between van der Waals interaction between cholesterols and dipole-dipole interaction between carbonate linkers of adjacent molecules. For a given $\pi - \pi$ distance between the two

PBI planes, only one type of interaction can dominate on one arm of a molecule. In helix B, van der Waals interactions dominate over the dipole, whereas in helix A, dipole-dipole interactions are more effective than van der Waals interactions.

Can dipolar interactions be dominant (aligned) in both the helices? Consider a dimer with a $\pi - \pi$ distance of 3.8 Å shown in Figure 6.16. In helix A, carbonate linkers are aligned with each other. Rotating the carbonate on a neighboring molecule, one can obtain the energy cost associated with rotation of carbonate linker so as to align it with the carbonate of the neigbouring molecule. With a slight rotation of about 5°-10°, the energy becomes repulsive due to hard contacts between the cholesterol moieties. Thus, the differential behaviour of dipole alignment in the two helices in a stack of **1** can be rationalized.

6.4 Conclusions

Molecular dynamics simulations elucidate the molecular features governing the mechanism of supramolecular polymerization. PBI appended with dipolar carbonate linkers and rigid cholesterol self-assembling moieties (molecule **1**) exhibit a cooperative growth. However, an absence of either dipolar carbonate linkers (molecule **2**) or a rigid self-assembling moieties (molecule **3**) lead to isodesmic self-assembly. Thus, the present work justifies the conjecture proposed earlier which states that long-range interactions along the stacking direction are essential for a cooperative growth [5]. MD studies demonstrate a dipole-driven cooperativity for **1**, while **2** and **3** self-assemble in isodesmic pathway due to lack of such interactions.

Bibliography

[1] Ogi, S.; Sugiyasu, K.; Manna, S.; Samitsu, S.; Takeuchi, M. *Nat. Chem.* **2014**, *6*, 188–195.

[2] Kang, J.; Miyajima, D.; Mori, T.; Inoue, Y.; Itoh, Y.; Aida, T. *Science* **2015**, *347*, 646–651.

[3] Ogi, S.; Fukui, T.; Jue, M. L.; Takeuchi, M.; Sugiyasu, K. *Angew. Chem. Int. Ed.* **2014**, *53*, 14363–14367.

[4] De Greef, T. F. A.; Smulders, M. M. J.; Wolffs, M.; Schenning, A. P. H. J.; Sijbesma, R. P.; Meijer, E. W. *Chem. Rev.* **2009**, *109*, 5687–5754.

[5] Kulkarni, C.; Balasubramanian, S.; George, S. J. *ChemPhysChem* **2013**, *14*, 661–673.

[6] Würthner, F. *Chem. Commun.* **2004**, 1564–1579.

[7] Chen, Z.; Stepanenko, V.; Dehm, V.; Prins, P.; Siebbeles, L.; Seibt, J.; Marquetand, P.; Engel, V.; Würthner, F. *Chem. Eur. J.* **2007**, *13*, 436–449.

[8] Würthner, F.; Thalacker, C.; Diele, S.; Tschierske, C. *Chem. Eur. J.* **2001**, *7*, 2245–2253.

[9] van der Weegen, R.; Korevaar, P. A.; Voudouris, P.; Voets, I. K.; de Greef, T. F. A.; Vekemans, J. A. J. M.; Meijer, E. W. *Chem. Commun.* **2013**, *49*, 5532–5534.

[10] Yagai, S.; Usui, M.; Seki, T.; Murayama, H.; Kikkawa, Y.; Uemura, S.; Karatsu, T.; Kitamura, A.; Asano, A.; Seki, S. *J. Am. Chem. Soc.* **2012**, *134*, 7983–7994.

[11] Kulkarni, C.; Bejagam, K. K.; Senanayak, S. P.; Narayan, K. S.; Balasubramanian, S.; George, S. J. *J. Am. Chem. Soc.* **2015**, *137*, 3924–3932.

[12] Mayo, S. L.; Olafson, B. D.; Goddard, W. A. *J. Phys. Chem.* **1990**, *94*, 8897–8909.

[13] Gasteiger, J.; Marsili, M. *Tetrahedron* **1980**, *36*, 3219 – 3228.

[14] Keasler, S. J.; Charan, S. M.; Wick, C. D.; Economou, I. G.; Siepmann, J. I. *J. Phys. Chem. B* **2012**, *116*, 11234–11246.

[15] Plimpton, S. *J. Comput. Phys.* **1995**, *117*, 1 – 19.

[16] Nosé, S. *J. Chem. Phys.* **1984**, *81*, 511–519.

[17] Hoover, W. G. *Phys. Rev. A* **1985**, *31*, 1695–1697.

[18] Fink, R. F.; Seibt, J.; Engel, V.; Renz, M.; Kaupp, M.; Lochbrunner, S.; Zhao, H.-M.; Pfister, J.; Würthner, F.; Engels, B. *J. Am. Chem. Soc.* **2008**, *130*, 12858–12859.

[19] Zhao, H.-M.; Pfister, J.; Settels, V.; Renz, M.; Kaupp, M.; Dehm, V. C.; Würthner, F.; Fink, R. F.; Engels, B. *J. Am. Chem. Soc.* **2009**, *131*, 15660–15668.

[20] Clark, A. E.; Qin, C.; Li, A. D. Q. *J. Am. Chem. Soc.* **2007**, *129*, 7586–7595.

[21] Frisch, M. J. et al. Gaussian 09 Revision D.01. Gaussian Inc. Wallingford CT **2009**.

Chapter 7

Future Outlook

The present thesis sheds light on the structural aspects, mechanism and thermodynamics of the self-assembly of organic molecules which polymerize supramolecularly along one-dimension. In chapters 2 and 3, supramolecular aggregation has been demonstrated via atomistic and coarse-grain modelling. Although coarse-grain models possess fewer degrees of freedom compared to atomistic ones, solvent degrees of freedom constitute a major part of the system and continue to be a bottleneck to access even larger length and time scales. As a result, simulations at low concentrations (μM) are prohibitively expensive. This can be circumvented by developing implicit solvent models. Dissipative particle dynamics (DPD) is an alternative approach through which study of supramolecular self-assembly can be greatly enriched.

Chapter 4 demonstrates the handedness reversal of a supramolecular columnar stack upon the application of an external electric field. Supramolecular chemistry offers ways to synthesize lead-free, all-organic ferroelectric materials. The mechanism of polar switching in other supramolecular compounds upon the application of external electric field and consequent handedness changes (if any) should be explored. Modification of molecular functional groups and supramolecular architecture to achieve enhanced polarizability at low fields should also be studied.

Self-assembled structures of BTA are sensitive to the attached peripheral substituents. In chapter 5, aggregate structures of amino ester-BTAs have been discussed. The effect of other kinds of substituents on the self-assembled structures can be investigated.

The mechanism of self-assembly of supramolecules can be identified based on the presence of long-range interactions along the growth direction. The same was demonstrated for perylene bisimide (PBI) derivatives here. Further, the proposed conjecture can be varied across various supramolecular compounds.

The cooperative nature of self-assembly of N,N',N"-trialkylbenzene-1,3,5-tricarboxamide derivative was demonstrated herein via free energy calculations using both atomistic and coarse-grain models.

Free energy to remove a molecule increases with oligomer size until the formation of nucleus and further remains constant. It will be interesting to explore the free energy changes for an isodesmic system to remove a molecule from various oligomer sizes. It is anticipated that the free energy change for the removal of a molecule from a stack remains constant with oligomer size.

Molecular dynamics simulations help in understanding aggregate structures and predict the size of nucleus (as described in chapter 3). Can new supramolecular systems whose nucleus is dormant and grows upon the addition of fresh feed of molecules be identified? One can thus obtain a living supramolecular polymer in which the polydispersity index is low.

To summarize, molecular dynamics simulations illustrate the microscopic understanding and unravel the interactions guiding the mechanism of self-assembly. The present thesis focussed on many such aspects which can be continued further.

List of publications

- Supramolecular Polymerization of Benzene 1,3,5 tricarboxamide: A Molecular Dynamics Simulation Study

  Bejagam, K. K.; Fiorin, G.; Klein, M. L.; Balasubramanian, S. *J. Phys. Chem. B* **2014**, 118, 5218-5228.

- Dissolution of Cellulose in Room Temperature Ionic Liquids: Anion Dependence

  Payal, R. S.†; **Bejagam, K. K.**†; Mondal, A; Balasubramanian, S. *J. Phys. Chem. B*, **2015** 119, 1654-1659. († Equal contribution)

- Dipole-Moment Driven Cooperative Supramolecular Polymerization

  Kulkarni, C; **Bejagam, K. K.;** Senanayak, S. P.; Narayan, K. S.; Balasubramanian, S; George, S. J. *J. Am. Chem. Soc.* **2015**, 137, 3924-3932.

- Supramolecular Polymerization: A Coarse Grained Molecular Dynamics Study

  Bejagam K. K.; Balasubramanian, S., *J. Phys. Chem. B* **2015** , 119, 5738-5746.

- External Electric Field Reverses Helical Handedness of a Supramolecular Columnar Stack

  Bejagam, K. K.; Kulkarni, C; George, S. J.; Balasubramanian, S., *Chem. Commun.* **2015**, 51, 16049-16052. (Highlighted in Chemistry World)

- Autoresolution of Segregated and Mixed p-n Stacks via Stereoselective Supramolecular Polymerization in Solution

  Narayan, B; **Bejagam, K. K.;** Balasubramanian, S.; George, S. J. , *Angew. Chem. Int. Ed.* **2015**, 54, 13053-13057.

- Host-Guest [2+2] Cycloaddition Reaction: Postsynthetic Modulation of CO_2 Selectivity and Magnetic Properties in a Bimodal Metal-Organic Framework

  Hazra, A; Bonakala, S.; **Bejagam, K. K.;**, Balasubramanian S.; Maji T. K. *Chem. Eur. J.* **2016**, 22, 7792-7799.

- Self-assembly of amino ester-based benzene-1,3,5-tricarboxamides: A molecular dynamics study

  Bejagam, K. K.;, Remsing R. C.; Klein, M. L.; Balasubramanian, S. (To be submitted).

Erratum

1. Chapter 2: It should be noted that DREIDING-C is more appropriate than DREIDING-N for modelling BTA molecules, as the former is able to capture the cooperative mechanism of oligomerization better.

2. Table 3.2 caption: 12 Å has to be seen as 15 Å.

3. In Chapter 5, it should be noted that the total simulation trajectory of about 300 ns (14 windows , each of 20 ns) was generated.

4. In Chapter 5, a figure has been added (see below) to illustrate the convergence in free energy. As surfaces obtained from trajectories of durations 15 ns and 20 ns do not vary much, the free energy can be seen to have converged, within an error bar of 1 kcal/mol.

5. The values in Table 5.5 should be rounded off to the nearest integer.

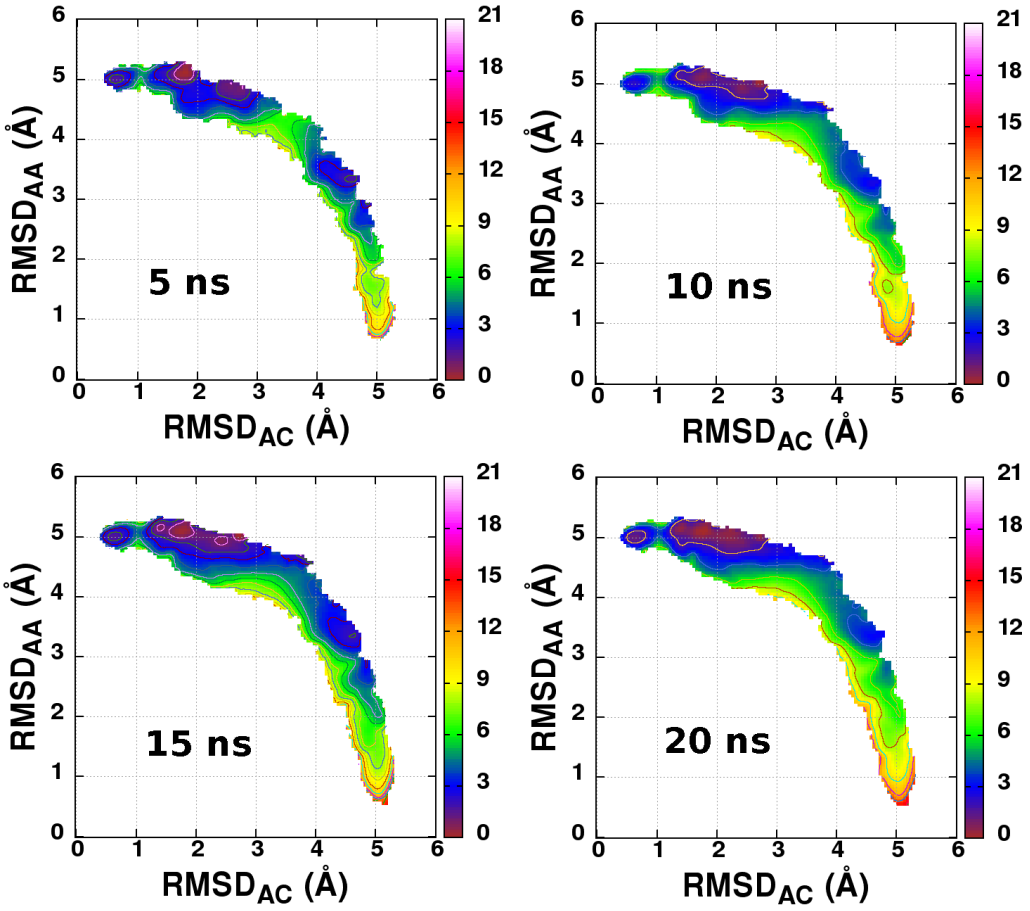

Figure 7.1: Evolution of free energy surface as a function of time for BTA-Met derivative.